VILNIUS UNIVERSITY
Centre of physical sciences and technology

Vilma
JONAUSKĖ

# Synthesis of calcium hydroxyapatite coatings on the stainless steel substrates and investigation of influence of substrates surface modification on the quality of coatings

**DOCTORAL DISSERTATION**

Natural sciences,
Chemistry N 003

VILNIUS 2019

The dissertation was carried out from 2013 to 2019 at Vilnius University.

**Scientific supervisors:**

**Prof. Habil. Dr. Aivaras Kareiva** (Vilnius University, Natural Sciences, Chemistry – N 003) (From 2013-10-01 to 2015-06-14).

**Prof. Dr. Jurgis Barkauskas** (Vilnius University, Natural Sciences, Chemistry – N 003) (From 2015-06-15 to 2019-12-01).

VILNIAUS UNIVERSITETAS
Fizinių ir technologijos mokslų centras

Vilma
JONAUSKĖ

# Kalcio hidroksiapatito dangų ant nerūdijančio plieno padėklų sintezė ir padėklų paviršiaus modifikavimo įtakos dangų kokybei tyrimas

**DAKTARO DISERTACIJA**

Gamtos mokslai,
Chemija N 003

VILNIUS 2019

Disertacija rengta 2013–2019 metais Vilniaus universitete.

**Moksliniai vadovai:**

**Prof. habil. dr. Aivaras Kareiva** (Vilniaus universitetas, gamtos mokslai, chemija – N 003) (nuo 2013-10-01 iki 2015-06-14).

**Prof. dr. Jurgis Barkauskas** (Vilniaus universitetas, gamtos mokslai, chemija – N 003) (nuo 2015-06-15 iki 2019-12-01).

TABLE OF CONTENTS

LIST OF ABBREVIATIONS

ACP – amorphous calcium phosphate
AFM – atomic force microscopy
ALD – atomic layer deposition
AISI – American iron and steel institute
APCVD – atmospheric pressure chemical vapor deposition
APS – atmospheric plasma spraying
CAM – contact angle measurements
CHAp – calcium hydroxyapatite
ClAp – chlorapatite
COF – coefficient of friction
CDHA – calcium-deficient hydroxyapatite
CVD – chemical vapor deposition
DCPA – dicalcium phosphate anhydrous
DCPD – dicalcium phosphate dihydrate
DNA – deoxyribonucleic acid
DRIFTS – diffuse reflectance infrared Fourier transform spectroscopy
EDTA – ethylenediaminetetraacetic acid
FAp – fluorapatite
FDA – food and drug administration
FTIR – Fourier transform infrared spectroscopy
GDP – gross domestic product
HDPE – high-density polyethylene
ICSD – inorganic crystal structure database
LPCVD – low pressure chemical vapor deposition
MCPA – monocalcium phosphate anhydrous
MCPM – monocalcium phosphate monohydrate
OCP – octacalcium phosphate
OXA – oxyapatite
PA – polyamide
PCL – poly(caprolactone)
PECVD – plasma-enhanced chemical vapor deposition
PEG – poly(ethylene glycol)
PGA – poly(glycolic acid)
PLA – poly(lactic acid)
PVA – poly(vinyl alcohol)
PVD – physical vapor deposition
RMS, Rq – root mean squared value of roughness

RPM – rate per minute
SBF – simulated body fluid
SEM – scanning electron microscopy
TCP – tricalcium phosphate
TTCP – tetracalcium phosphate
TEA – triethanolamine
VLPCVD – very low pressure chemical vapor deposition
XPS – X-ray photoelectron spectroscopy
XRD – X-Ray diffraction

# INTRODUCTION

Human lifespan is constantly increasing thanks to improvement of living conditions and health care [1]. However ageing population requires more medical services, procedures and medical devices. Since good health is top priority for most governments, the share of gross domestic product (GDP) for health care is constantly growing [2-4]. This leads to a search for new technologies which would be good value for money. Ageing of population is responsible for the incidence of osteoarthritis and osteoporosis thus bones replacement with implants is very common surgery [5]. Most of the implants (approximately 80%) are made of metals due to their perfect mechanical properties, resistance to corrosion and acceptable biocompatibility [6, 7]. Most popular metals and alloys for implants are cobalt-chromium alloys, titanium, titanium alloys and zirconium (for dental implants) [8, 9]. However titanium and titanium alloys are very expensive in comparison to medical grade stainless steel. Good mechanical properties, corrosion resistance, biocompatibility and low price make 316L stainless steel preferred material for medical and dental applications [10-12].

Implant is an exotic material for the body therefore its surface morphological and other properties have a huge impact on the behaviour of bone cells that come into contact with implants [13, 14]. Of course, the immune system of individual patient is very important and sometimes crucial for the response to implant biomaterials [15]. It was shown that the use of calcium hydroxyapatite ($Ca_{10}(PO_4)_6(OH)_2$; CHAp) on metallic implant can reduce patient recovery time from 100 days with non-coated implant to only 20 days with CHAp coated implant after implantation [11]. Calcium hydroxyapatite is widely used for bone grafting. CHAp is suitable for bone substitution due to a similar chemical composition and the crystal structure as natural hard tissue [16, 17]. However, the brittleness and poor mechanical properties of CHAp ceramics limit their application to replacement of small, non-load-bearing bone parts [18]. In order to overcome this disadvantage CHAp is usually used as a thin coating on metallic implants. Additionally, CHAp acts as a protective barrier from ion release of metals [19]. The mechanical performance of metals and their alloys in combination with the biocompatibility of CHAp coating gave promising results [20].

There are number of methods for the fabrication of CHAp coatings on various substrates such as sol-gel, plasma spraying, ion-beam sputtering, electrophoretic deposition and others. Processes requiring high temperatures can lead to the formation of alternative phosphate phases which influence the

dissolution rates of coating and affect mechanical properties of implants [21]. Plasma spraying is the most popular technique used commercially and the only clinically accepted method to deposit CHAp on various substrates [22, 23]. However, it has significant disadvantages such as poor control over coating phase composition, crystallinity, thickness, morphology, and resistance to delamination [17, 21]. The sol-gel processing route for thin films have some benefits over other methods such as simplicity, synthesis at low temperatures, effectiveness, suitability for complex-shaped implants, chemical homogenity, fine grain structure of the end product and cost efficiency [11, 24-26].

The main aim of this doctoral thesis was to develop an effective synthetic procedure for CHAp on variously modified 316L stainless steel substrates and investigate different properties of obtained coatings in order to use the CHAp coated stainless steel for manufacture of permanent implants. Regardless the fact that medical grade stainless steel is widely used in medicine and dentistry it still has potential to replace expensive prosthetics from titanium or cobalt-chromium alloys [27]. From this point of view our research is quite novel and in case of success can significantly reduce implantation cost. Moreover, the specific modifications of stainless steel surface to obtain CHAp coatings of better quality also shows novelty and originality of the results presented in this PhD thesis. For this reason, the tasks to achieve the main goal were formulated as follows:

1. To synthesize and characterize CHAp thin films on 316L stainless steel with low number of layers using spin-coating and dip-coating techniques.

2. To synthesize and characterize CHAp thin films on 316L stainless steel with large number of layers at lower temperature and compare spin-coating and dip-coating techniques.

3. To synthesize and characterize CHAp thin films deposited on specifically roughened stainless steel surface.

4. To investigate impact of simulated body fluid (SBF) on the surface properties of CHAp coated 316L stainless steel samples.

5. To synthesize and characterize CHAp thin films on stainless steel substrate modified with TiN sublayer.

# 1. LITERATURE OVERVIEW

## 1.1. OVERVIEW OF CALCIUM PHOSPHATES

Calcium phosphates are found in nature in several forms and are widely used in biology, geology, dentistry and medicine and different fields of industry. The properties of phosphates and, concequently, their applications depend on their structure, composition, solubility, and stability [28]. The Ca/P molar ratio in calcium phosphates can vary from 0.5 to 2.2. Generally, the higher Ca/P ratio gives the lower solubility of a compound [29]. Hydroxide ions can be replaced with halide and this way fluorapatite or chlorapatite obtained. Whitlockite which is unusual form of calcium phosphate will form in the presence of magnesium ions. The presence of carbonate will result in the formation of carbonated apatite. The origin of calcium phosphates can be natural or synthetic [30]. The most used calcium phosphates with their chemical formulas, abbreviations, Ca/P ratios and space groups are listed in Table 1 [31, 32].

**Table 1.** Calcium phosphates chemical formulas, abbreviations, Ca/P molar ratio and space groups.

| **Name, formula** | **Abbreviation** | **Ca/P** | **Space group** |
|---|---|---|---|
| Monocalcium phosphate monohydrate, $Ca(H_2PO_4)_2 \cdot H_2O$ | MCPM | 0.50 | Triclinic |
| Monocalcium phosphate anhydrous, $Ca(H_2PO_4)_2$ | MCPA | 0.50 | Triclinic |
| Dicalcium phosphate dihydrate, $CaHPO_4 \cdot 2H_2O$ | DCPD | 1.00 | Monoclinic |
| Dicalcium phosphate anhydrous, $CaHPO_4$ | DCPA | 1.00 | Triclinic |
| Amorphous calcium phosphate, $Ca_xH_y(PO_4)_z \cdot nH_2O$, n=3-4,5; 15-20% $H_2O$ | ACP | 1.2-2.2 | Not applicable |
| | OCP | 1.33 | Triclinic |

| | | | |
|---|---|---|---|
| Octacalcium phosphate, $Ca_8(HPO_4)_2(PO_4)_4{\cdot}5H_2O$ | | | |
| Whitlockite (mineral), $Ca_{18}Mg_2(HPO_4)_2(PO_4)_{12}$ | | 1.43 | Rhombohedral |
| α-tricalcium phosphate, α-$Ca_3(PO_4)_2$ | α-TCP | 1.50 | Monoclinic |
| β-tricalcium phosphate, β-$Ca_3(PO_4)_2$ | β-TCP | 1.50 | Rhombohedral |
| Calcium-deficient hydroxyapatite, Ca10-x(HPO4)x(PO4)6-x(OH)2-x, 0<x<1 | CDHA | 1.5-1.67 | Hexagonal |
| Hydroxyapatite, $Ca_{10}(PO_4)_6(OH)_2$ | CHAp | 1.67 | Hexagonal |
| Fluorapatite, $Ca_{10}(PO_4)_6F_2$ | FAp | 1.67 | Hexagonal |
| Chlorapatite, $Ca_{10}(PO_4)_6Cl_2$ | ClAp | 1.67 | Monoclinic |
| Oxyapatite, $Ca_{10}(PO_4)_6O$ | OXA | 1.67 | Trigonal |
| Carbonated apatite, A-$Ca_{10}(PO_4)_6CO_3$ B-$Ca_{10}(PO_4)_{6-x}(CO_3)_{3x/2}(OH)_2$ | A-$CO_3$Ap B- $CO_3$Ap | 1.67 for A Varies for B | Monoclinic (for A-$CO_3$Ap) |
| Tetracalcium phosphate, $Ca_4(PO_4)_2O$ | TTCP | 2.00 | Monoclinic |

Calcium phosphates are of a very special interest since they are the most important inorganic component in human and other vertebrate bones and teeth. Due to biocompatibility to living tissues calcium phosphates along with other materials such as various bioglasses, zirconia, carbon nanostructures, etc. are known as bioceramics. In addition, these bioceramics are also resistant to microbial attack, pH changes and solvent conditions [33].

Properties required from calcium phosphates bioceramics for medical applications are presented in Figure 1 [34].

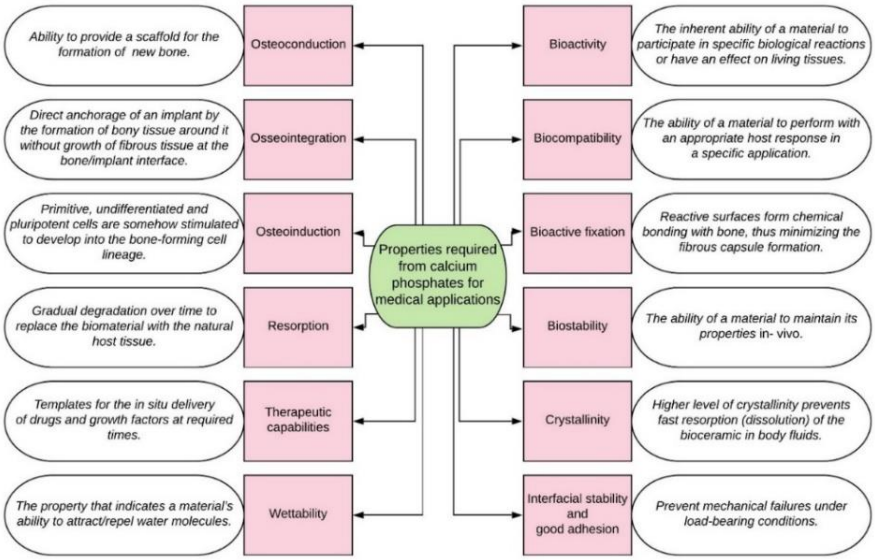


**Figure 1.** Properties required from calcium phosphates bioceramics for medical applications.

According to bioceramics performance after implantation they are divided into following groups [32, 35]:

1. Bioinert – do not interact with bone tissue and do not promote important changes. These materials are mainly used as supporting media;

2. Biotoxic – stimulate immune response by releasing substances in toxic concentrations this way triggering antigens formation;

3. Biocompatible – do not provoke adverse reactions and neither release any toxic constituents;

4. Bioactive – promote formation of biological apatite responsible for bone healing. Due to structural similarities with bone tissue they are used as bone parts replacement;

5. Bioresorbable – degrade over time in physiological fluids. Only used for temporary support while tissues regenerate themselves.

In medicine and dentistry for bone replacement, restoration and implantation calcium phosphates can be used in different forms such as scaffolds, powders, granules, nanoparticles, injectable cements, porous ceramics, blocks and coatings [36, 37]. Most recent studies showed, that calcium phosphates can be used as matrices for drug release control and even substrates for DNA delivery in gene therapies [38-40].

Since calcium phosphates are mostly used to replace damaged bones they must resist mechanical loads and be able to form active apatite layer for bone bonding. General schematic illustration of bone defect regeneration with short-term support from calcium phosphate cement is presented in Figure 2 [41].

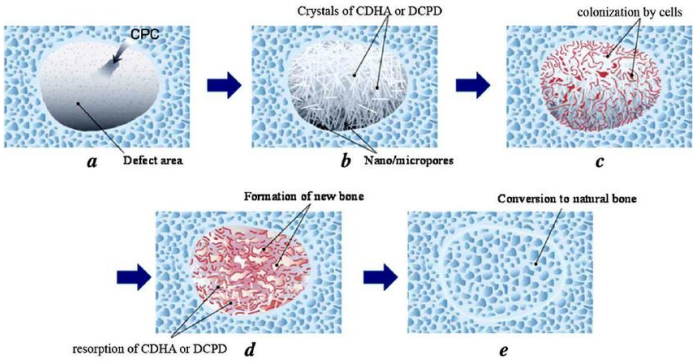


**Figure 2**. Schematic illustration of bone defect regeneration: (a) filling of a cavity with a thick calcium phosphate cement (CPC), (b) cement setting with formation of the end product (CDHA or DCPD), (c) colonization by cells, (d) resorption of CDHA or DCPD and formation of new bone, (e) bone regeneration.

After filling bone defect with calcium phosphate cement paste, cement starts to set following by formation of calcium-deficient hydroxyapatite (CDHA) or dicalcium phosphate dehydrate (DCPD). Phosphate crystals are then colonized by bone cells and new bone begins to form. By the time bone is fully regenerated, CDHA or DCPD fully resorbs.

Examples of ceramic coated metal as permanent implant and bioresorbable ceramic scaffold for hard tissue restoration are presented in Figure 3 [42, 43].

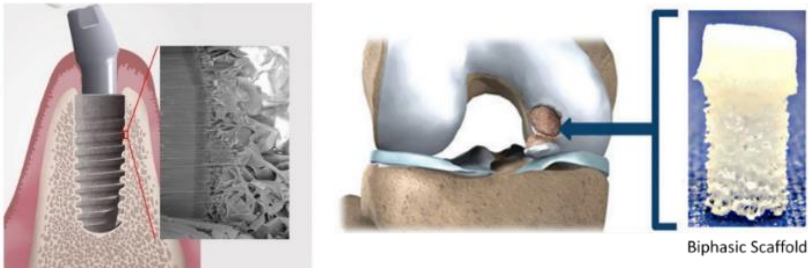


**Figure 3**. Dental implant coated with bioceramics (left) and bioceramic scaffold for bone restoration (right).

One of the most important characteristics which has huge impact for calcium phosphates bioactivity is porosity. Porosity of artificial material should mimic that one of natural material in order to perform the same physiological role. Pores in natural bone tissue are hierarchical and interconnected with a size within micron range [44]. The presence of pores stimulates protein interaction with the surface. Protein adsorption is enhanced when the pore size of calcium phosphate is 20–500 μm [45, 46]. Pore size affects bone incorporation as well. Bone ingrowth is possible at a pore size of about ≥50 μm. On the other hand, pore sizes larger than 100 μm affect the mechanical strength of calcium phosphate [47-49]. Pores larger than 1000 μm determines functionality and shape of the implant [44]. Poor mechanical properties of calcium phosphates such as brittleness, low impact resistance and low tensile stress are results of high porosity [50].

Even more, surface of implanted materials must be hydrophilic. Hydrophilicity affects cellular reactions and has huge possitive effect on adhesion, proliferation and maturation of bone cells [51, 52].

### 1.1.1. Calcium hydroxyapatite

Calcium hydroxyapatite ($Ca_{10}(PO_4)_6(OH)_2$; CHAp) is naturally occurring mineral and is most abundant compound in bones and teeth [53]. Apatite was discovered in 1786 by the famous German geologist Abraham Gottlob Werner (1750–1817). The origin of the name „apatite“ is from ancient Greek απατάω (apatao) meaning “to mislead” because apatite had been mistaken for other minerals, such as beryl, tourmaline, chrysolite, amethyst, fluorite, etc. [54].

Crystal structure of CHAp is presented in Figure 4 [55].

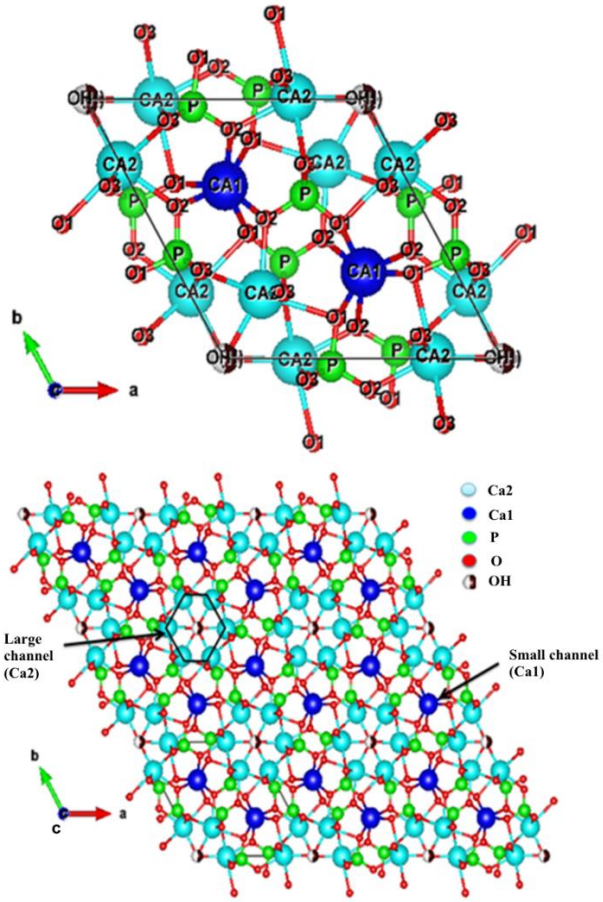


**Figure 4**. Detailed crystallographic structure of calcium hydroxyapatite, representing two different positions for $Ca^{2+}$ ions along with large and small channels within the crystal.

CHAp crystallizes in the hexagonal system (space group P63/m) with the crystallographic parameters: $a = b = 9.418$ Å, $c = 6.881$ Å, $\beta = 120°$C. CHAp structure is composed of tetrahedral $PO_4$ groups, where $P^{5+}$ ions are in the center of the tetrahedrons and whose tops are occupied by 4 oxygen atoms. Each $PO_4$ tetrahedron is shared by a column and delimits two types of unconnected channels. The first small channel has a diameter of 2.5 Å and is surrounded by $Ca^{2+}$ ions (Ca1 in Figure 4). They are coordinated with 9 oxygen atoms of the $PO_4$ tetrahedrons. The second type of channel determines unique properties of apatites. It has a diameter larger than the previous one (3–4.5 Å), and contains six other $Ca^{2+}$ ions (Ca2 in Figure 4). They are located

at the periphery of the channel and coordinated with 7 oxygen atoms belonging to $PO_4$ tetrahedron and one $OH^-$ anion. Due to existence of two different calcium sites, the properties of CHAp can be tuned by specific modification of the site. These channels host $OH^-$ groups along the *c* direction to balance the positive charge of the matrix. The $OH^-$ ions are present in columns perpendicular to the unit cell face, at the center of the large channels. The dimension of the channel enables certain mobility to these ions and consequently allows their circulation along the channels in the direction of z axis. A key element of the apatite structure is that it allows a great number of substitutions that leave the crystallographic structure unchanged [56].

Recent studies discovered that CHAp can also exist in a monoclinic form. The monoclinic form is the most thermodynamically stable form, even at room temperature. The main difference between the monoclinic form and the hexagonal form is the orientations of the $OH^-$ groups (Figure 5). In the hexagonal CHAp, two adjacent hydroxyl groups point at the reverse direction, while in the monoclinic form—hydroxyl groups have the same direction in the same column, and an opposite direction among columns [34, 57].

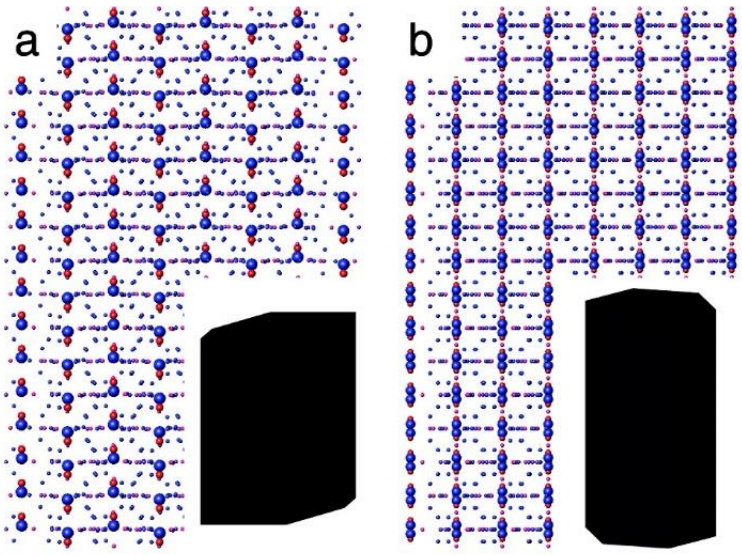


**Figure 5**. Schematic drawings of the atomic structures of monoclinic CHAp (a) and hexagonal CHAp (b). The hydroxyl ions are emphasized in the drawings to illustrate the primary difference of the two structures, and the symmetry-determined morphologies of the crystals are inserted at the lower right corners [57].

Degradation of CHAp strongly depends on its crystallinity and stoichiometry. Amorphous CHAp has a faster degradation rate than crystallized, therefore well-crystallized stoichiometric CHAp is considered to be the most stable Ca-P compound at the pH, temperature and composition of the physiological fluid, thus ideal material for the application inside human body [58].

Dissolution of calcium phosphate compounds is a complex process as it is accompanied by other chemical reactions such as precipitation of Ca and P and hydrolysis of TCP [33, 59]. The physicochemical dissolution process depends on the surface area to volume ratio, fluid convection, acidity and temperature. Bioresorption is usually mediated by osteoclast cells and sometimes by macrophages [58]. Generally, CHAp is inert material which doesn‘t resorb over time [60].

Mechanical properties of CHAp depends on density, sinterability, crystal size, phase composition and others. Dense structure with fine grains are way more resistant and tougher than porous ones with larger grains [58].

Regardless structural and chemical similarity to natural apatite, synthetic apatites differ chemically from biological CHAp, because natural bone-like apatites often include cations such as $Mg^{2+}$, $Na^{+}$, and $K^{+}$ and anions such as $Cl^{-}$ and $F^{-}$. However, the main substituent is carbonate at levels of 5–8 wt % of bone minerals [61]. Carbonated hydroxyapatite has increased bioactivity and biocompatibility [30]. Interesting fact, that bones contain almost 80% of the total body carbon dioxide [62].

Biomedical applications of calcium hydroxyapatite are presented in Figure 6 [63].

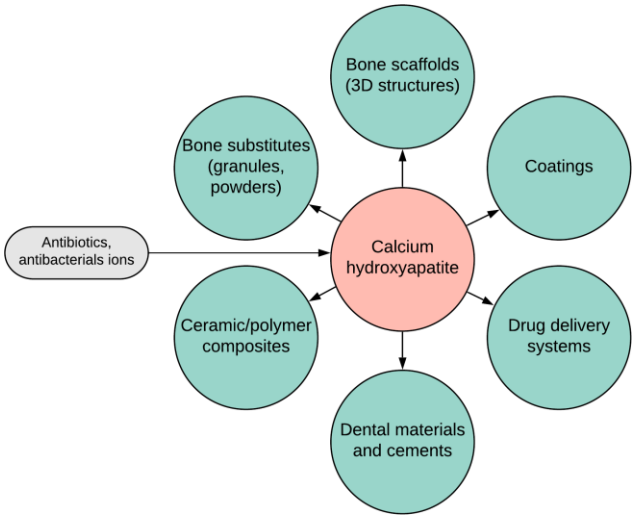


**Figure 6.** Biomedical applications of calcium hydroxyapatite.

Antimicrobial properties of CHAp can be achieved in two ways. First method is to load the pores of CHAp with therapeutic molecules as drug delivery systems. This way ensures precise drug delivery to the damaged area. The local and sustained release of drugs allows shortening of the prolonged therapies and can accelerate the bone healing process, as well minimize the extent of surgical removal of the affected bone [64]. Other method to achieve desired antimicrobial properties is the doping of CHAp with functional ions such as $Ag^{+}$, $Zn^{2+}$, $Cu^{2+}$, $SeO_3^{2-}$ or other. Silver is known as antimicrobial agent for many centuries. It exhibits actions against bacteria, fungi and viruses mainly by inactivating microbial proteins. $Zn^{2+}$ ions affect bacteria by damaging cell membrane and interacting with bacterial enzymes. The antimicrobial activity of $Cu^{2+}$ ions is linked to its interaction with bacterial proteins, membranes and nucleic acids. The $SeO_3^{2-}$ ions inhibit bacterial attachment, growth and formation of a biofilm [63].

### 1.1.2. Other calcium phosphates

Other calcium phosphates are also important materials for bone tissue engineering. Different materials should be used for different indications and areas based on their properties. One of the most important properties is the resorption rate which depends on two factors – surface properties and

chemical composition [65]. The surface properties are mainly determined by porosity which was described previously.

Bone fillers made of pure CHAp due to their stability remains in the hard tissue for years, thus more soluble calcium phosphate bioceramics are preffered for medical applications (see Figure 7) [66]. As we can see, calcium deficient hydroxyapatite (CDHA) resorbs within 72 weeks, meanwhile pure CHAp remains as permanent foreign body. Generally speaking CHAp is not resorbable, whereas the other compositions are resorbed too quickly, therefore combinations of CHAp with $\beta$-tricalcium phosphate ($\beta$-TCP) as well as $\alpha$-TCP, octacalcium phosphate, dicalcium phosphate and others are used. CHAp has ability to bond directly to the bone while α-TCP dissolves in the body 10 times faster than CHAp and is source of Ca and P ions for the formation of new bone. Studies showed that biphasic ceramics of CHAp/TCP induce faster bone regeneration than CHAp alone [67]. The reactivity of biphasic formulations of CHAp with any type of TCP increases with increasing TCP/CHAp ratio. Thus, the *in vivo* bioresorbability of such formulations can be adjusted through the phase composition. The same principles apply for triphasic (CHAp, α-TCP and β-TCP) formulations [68].

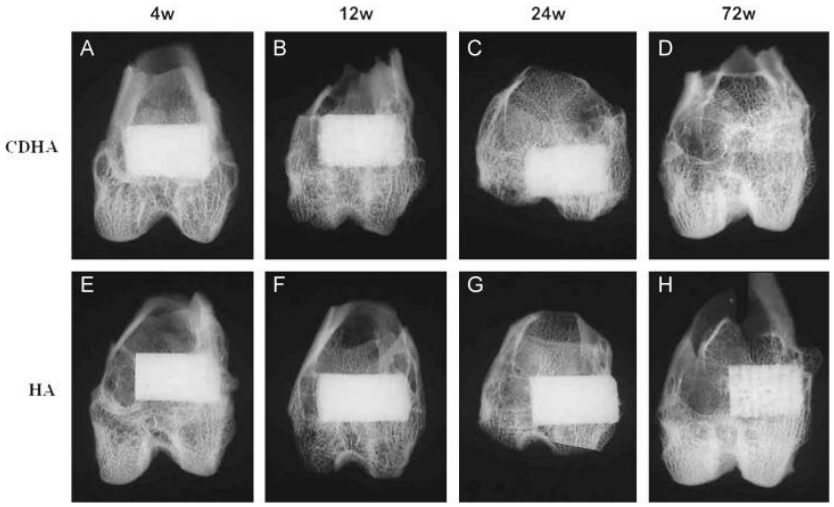


**Figure 7.** X-ray photographs of the operated portion of the rabbit femur. 4 weeks (a), 12 weeks (b), 24 weeks (c) and 72 weeks (d) after implantation of CDHA; 4 weeks (e), 12 weeks (f), 24 weeks (g) and 72 weeks (h) after implantation of sintered CHAp [66].

Special attention should be given to amorphous calcium phosphate (ACP). Beside crystalline forms, amorphous calcium phosphate is very frequent form of phosphates in living organisms. Locations of our body in which ACP (pure or in combination with $Mg^{2+}$) can be found are bone, enamel, small intestine, calciprotein particles in blood and casein micelles in breast milk. ACP is very important for the achievement of a specific physiological functions [69]. Likely, ACP is the precursor to the formation of the crystalline material in many biomineralization processes [70]. In medicine, ACP is used in cements as bone substitution materials, and in other dental applications. In the acidic oral environment ACP release calcium and phosphate ions, which may participate in enamel remineralization. The ACP-containing biocomposites and hybrid biomaterials are used as anticariogenic and/or remineralizing agents in chewing gums, sugar confections, tooth mousses, bleaching gels and mouth rinses [34].

### 1.1.3. Calcium phosphates in human bones and teeth

Bone is a natural organic–inorganic ceramic composite of complex microstructure. Due to hierarchical levels of structural organization bone is very difficult to analyze [71]. Structure of bone is presented in Figure 8 [72].

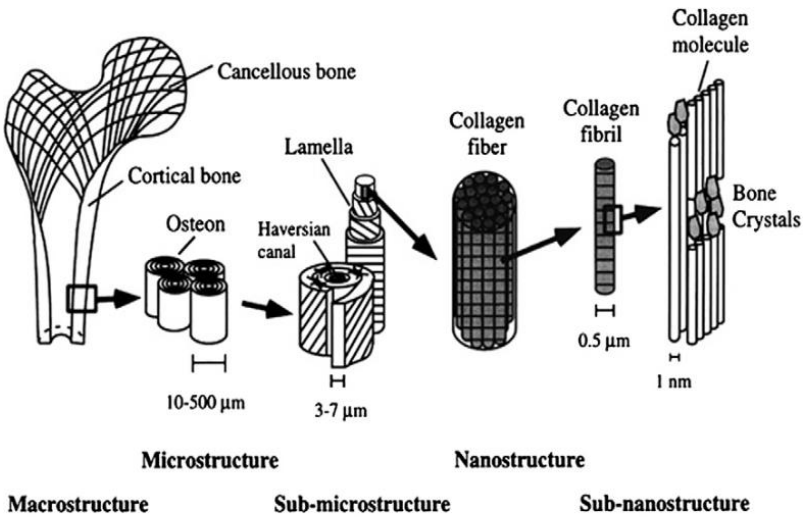


**Figure 8**. Hierarchical structure of bone at various scales.

Major bone constituents are calcium phosphates (69 wt%), collagen (20 wt%) and water (9 wt%). Additionally, other organic materials, such as proteins, polysaccharides and lipids are also present in small quantities. Collagen is bone matrix in the form of small microfibers. The diameter of the collagen microfibers varies from 100 nm to 2 μm. Calcium phosphate in the form of crystallized hydroxyapatite provides stiffness to the bone. CHAp forms well-arrayed, nanocrystalline rods approximately 25-50 nm in lenght embedded within collagen fibrils. [71]. The formation of the apatite in the extracellular space of the collagen is called "biomineralization" [34].

There are three main human hard tissues – bone, dentine and enamel. Differences of elemental composition among these tissues are presented in Table 2 [73].

**Table 2**. Mean values of elemental composition of dried human main hard tissues.

| Element or ion | Bone | Dentine | Dental enamel |
|---|---|---|---|
| Major elements (wt %) | | | |
| **C (total)** | 16.7 | 11.8 | 1.4 |
| **$CO_3^{2-}$** | 5.6 | 4.6 | 3.2 |
| **N** | 4.9 | 4.0 | 0.32 |
| **Ca** | 25.4 | 26.9 | 36.6 |
| **P** | 11.6 | 13.2 | 17.7 |
| Minor elements (wt %) | | | |
| **Cl** | 0.13 | 0.065 | 0.37 |
| **K** | 0.0047 | 0.024 | 0.070 |
| **Mg** | 0.27 | 0.74 | 0.29 |
| **Na** | 0.53 | 0.76 | 0.77 |
| **S** | 0.08 | 0.070 | 0.021 |
| Main trace elements (ppm) | | | |
| **Al** | 29 | 210 | 55 |
| **B** | 22 | - | 11 |
| **F** | 400 | 215 | 50 |
| **Fe** | 76 | 44 | 34 |
| **Pb** | 4.4 | 15 | 17 |
| **Sr** | 70 | 145 | 173 |
| **Zn** | 205 | 148 | 170 |

Different elemental composition and organic-inorganic phase ratio results in different properties of these hard tissues. Tooth enamel (see Figure 9 [74]) which is highly mineralized and containing only 1% of organic matrix is the hardest tissue of all vertebrates. Apatites in enamel are closer to stoichiometry, therefore less soluble and consequently more resistant to acidic attacks from foods or oral bacteria. Dentine is much less mineralised than enamel, but due to collagen matrix has better tensile strength. Bone is even less mineralised than dentine, but possesses a high adaptability to mechanical stress. [73].

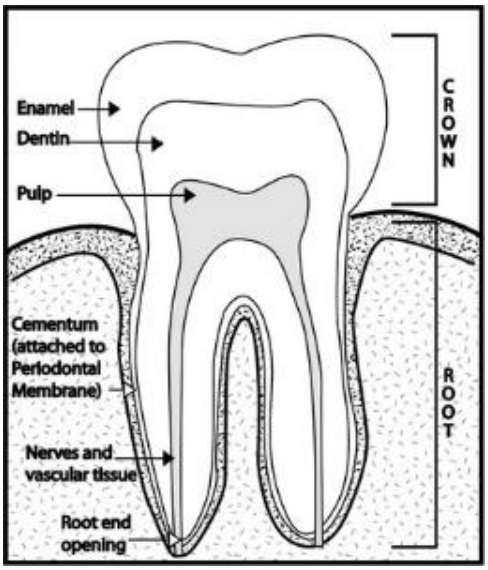


**Figure 9.** Tooth anathomy.

Biological apatites are always carbonate substituted and calcium deficient, therefore nonstoichiometric [75]. Bone apatite contains approximately 7 wt % carbonate and tooth enamel contains about 3.5 wt % carbonate. Basically, two types of carbonate substitutions within apatite are possible, either at $OH^-$ site (type A substitution) or at $PO_4^{3-}$ (type B substitution) site. Synthetically, A-type carbonate apatite can be produced only at very high temperature (solid-state reactions at 1000 ºC), whereas B-type carbonated apatite precipitates from solutions in the temperature range of 50–100 ºC. It is generally accepted that in biological apatites B-type substitution is dominant. The charge imbalance created by the replacement of one $PO_4^{3-}$ tetrahedral group by one $CO_3^{2-}$ group could be counter-balanced by creating a vacancy [76]. Another specificity of biological apatites is substitution of $PO_4^{3-}$ ions with $HPO_4^{2-}$. Two

types of divalent ions substituting for $PO_4^{3-}$ (type B $CO_3^{2-}$ and $HPO_4^{2-}$) have been shown to correspond to the formation of calcium deficient apatites [73]. Studies also revealed, that biological apatites lack $OH^-$ ions in their crystallographic sites [77]. This might be explained with A-type carbonate substitutions and demands of charge balance in B-type substitution [76].

Apatite in human bone, dentine and enamel formulas based on simplified model of calcium deficient apatites are presented below (sodium content, the presence of type A carbonate replacing $OH^-$ ions, hydrated layer impact and all minor and trace elements except Mg are not taken into account):

Human bone apatite: $Ca_{8.1} \cdot Mg_{0.2} \cdot (PO_4)_{4.3} \cdot (HPO_4)_{0.5} \cdot (CO_3)_{1.2} \cdot (OH)_{0.3}$ (1)

Human dentine apatite: $Ca_{8.0} \cdot Mg_{0.4} \cdot (PO_4)_{4.4} \cdot (HPO_4)_{0.7} \cdot (CO_3)_{0.9} \cdot (OH)_{0.4}$ (2)

Human enamel apatite: $Ca_{8.8} \cdot Mg_{0.1} \cdot (PO_4)_{4.9} \cdot (HPO_4)_{0.6} \cdot (CO_3)_{0.5} \cdot (OH)_{0.9}$ (3)

## 1.2. BONE GRAFTING AND IMPLANTS

From medical point of view, the most common form of bone regeneration is fracture healing. Unlike in other tissues, the majority of bone injuries heal without the formation of scar tissue, and bone is regenerated with it‘s original properties restored, and with the newly formed bone being eventually indistinguishable from the adjacent uninjured bone. However, there are conditions in orthopaedic surgery and in oral and maxillofacial surgery in which bone regeneration is required in large quantity (beyond the normal potential for self-healing), such as for skeletal reconstruction of large bone defects created by trauma, infection, tumour resection and skeletal abnormalities, or cases in which the regenerative process is compromised [78]. Bone grafting is one of the most commonly used surgical methods to augment bone regeneration in orthopaedic procedures [79]. Bone grafts are natural or synthetic materials with bone healing properties, implanted into the affected bone areas [80].

### 1.2.1. Natural bone grafts

There are four types of biological grafts for bone parts replacement:

1. Autografts, where bone is taken from the patient‘s own body.

2. Isograft, where bone is taken from the same species and share the same antigenic properties (twins).

3. Allografts, where bone is taken from the same species but different antigenic properties (donor).

4. Xenografts, where material is obtained from different species to humans (bovine, porcine, equine, coralline, algae).

Autografts are considered the ‘gold standard’ among the other available grafting materials due to excellent osteogenic, osteoinductive, osteoconductive properties, no disease transmission and very low risk of of a negative immune reaction. However, rapid resorption of autogenous bone, donor site complications, increased anaesthesia time, increased blood loss and limited amount of graft material especially for large restorations are major drawbacks of autografts. The same advantages and disadvantages applies to isografts [81]. Allografts are osteoinductive, osteoconductive and relatively available, but there is possibility of disease transmission and negative immune response. Allografts properties varies depending on the production method and they are expensive. Xenografts are osteoconductive, available and cheap. Their disadvantage is the fact that bone characteristics differ compared to humans while their processing procedure might affect their physico–chemical properties as well as possibility of disease transmission and stimulation of immunogenicity [82]. In adition, the use of xenograft has raised some ethical and religious concerns, since the use of animal derived products should be considered before use with patients consent for various individuals [81].

### 1.2.2. Synthetic bone grafts

The serious shortage of natural bone grafts and the little chance of supply meeting the demands in an aging population has led research in the field of bone tissue engineering. Growing availability, safety and no donor-site damage are the reasons that synthetic bone substitutes are being used more and more [79]. Various materials, such as calcium phosphate, calcium carbonate, calcium sulfate, bioactive glasses and polymers represents this category [82]. Calcium phosphates were already described in a previous chapter.

*Bioactive glasses.* Bioactive glass is a group of synthetic silicate-based ceramics. Originally constituted by silicon dioxide ($SiO_2$), sodium oxide ($Na_2O$), calcium oxide (CaO), and phosphorus pentoxide ($P_2O_5$), but later modified to a more stable composition by adding potassium oxide ($K_2O$), magnesium oxide (MgO) and boron oxide ($B_2O_3$). The optimized constitutions lead to a strong physical bonding between bioglass and host bone. The resorption of bioactive glasses varies, depending on constituents ratio. Like

the other ceramics, the mechanical properties of bioglass are brittle and weak. Therefore, it has been mainly applied in the reconstruction of facial defects [79, 82].

*Calcium sulphate.* Calcium sulphate is supplied in the form of cement or granules, which possess favourable properties such as biocompatibility, bioactivity, tolerability, osteoconductivity, easy handling and low cost. Calcium sulphate absorbs more quickly than new bone grows, therefore combinations with other materials has to be used. This bone substitute provides minimal structural support and can‘t be used for restoration of load-bearing parts. It is mainly applied in dentistry [83].

*Calcium carbonate*. Calcium carbonate nanoparticles are largely used in bone grafting as well as food packaging, feed additive, pharmaceutics, coating pigment and polymer fillers [84]. Calcium carbonate absorbtion rate is lower than that of calcium phosphates and it has excellent biocompatibility and osteoconductivity. The difficulty of preparing a calcium carbonate ceramic is that it readily decomposes to CaO and $CO_2$ between 600 °C and 700 °C [85].

*Polymers*. Polymer-based biomaterials have major advantages in sourcing, fabrication, controlled structure, and no risk of disease infection. The first polymer-based bone substitute was the hydroxyapatite (HA)/high-density polyethylene (HDPE) composite [86]. The main concept of polymeric composites is combination of elastic protein with stiff mineral to mimic natural bone [87, 88].

Synthetic scaffolds serve as a reservoir for different molecules, such as water and nutrients, and for various mediators such as cytokines and growth factors [89].

### 1.2.3. Metallic implants

Medicine aims to regenerate damaged hard tissues using resorbable scaffolds instead of replacing them [90]. Unfortunatelly, this is not always possible. Implants are used when bone tissue needs to be replaced by medical devices due to various problems such as osteoporosis, cancer, fractures [49]. Most of the implants (about 70-80%) are made of metals, however only limited number of them are suitable for long-term applications [91, 92]. The implant and bone cells are considered well osseointegrated when new bone cells form, proliferate, and differentiate on the implant. To find a strong binding material between the metallic implant and surrounding bone, a bioactive interface must be encouraged to give a better bone regeneration with expedited healing. Many studies are focused on the surface modifications to

gain outstanding bone regeneration ability. Development of porosity on the surface, nanoceramic coating, hydroxyapatite coating and thermal heat treatment are some of the strategies used to improve the bone integration with metallic implants [93].

Metals used in medicine possess good mechanical properties and biocompatibility. There are tree main types of metallic implants based on material they are made of: stainless steel, cobalt-chromium alloy and titanium alloy [94]. Comparison of mechanical properties of metallic biomaterials with bone is presented in Table 3 [95]. Precious metals such as gold, silver and platinum based alloys are mainly used for dental applications.

**Table 3.** Comparison of mechanical properties of metallic biomaterials with bone.

| **Material** | **Young's modulus, (GPa)** | **Yield strength, (MPa)** | **Tensile strength, (MPa)** | **Fatigue limit, (MPa)** |
|---|---|---|---|---|
| Stainless steel | 190 | 221-1213 | 586-1351 | 241-820 |
| Co-Cr alloys | 210-253 | 448-1606 | 655-1896 | 207-950 |
| Titanium (Ti) | 110 | 485 | 760 | 300 |
| Ti-6Al-4V | 116 | 896-1034 | 965-1103 | 620 |
| Cortical bone | 15-30 | 30-40 | 70-150 | - |

One of the most important parameters of metallic implant is its Young's modulus, i.e. stiffness of a material. Young's modulus of the implant must match the one of a bone to avoid stress shielding followed by implant loosening and inflamation [96]. Another important requirement for metallic biomaterial is wear resistance. Wear of artificial joints releases debris particles into the body. Those particles damage corrosion resistant layer on the surface, thus accelerate corrosion and often lead to problematic inflammation and even cancer [97]. Due to many mechanical as well as biological reasons implants can fail during post-surgery period. Various causes for implant failure are presented in Figure 10 [98].

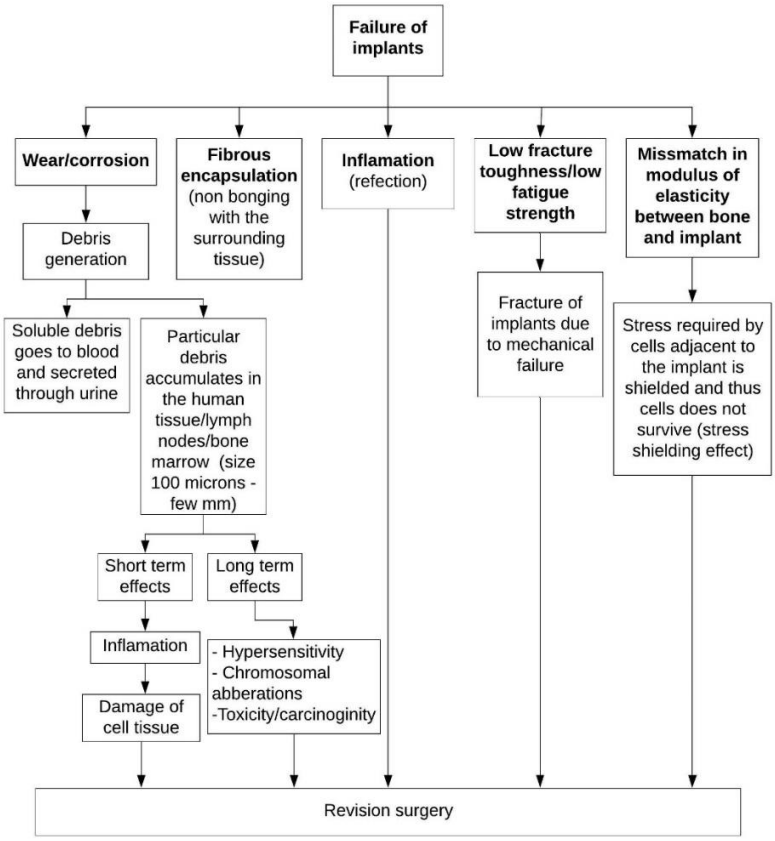


**Figure 10.** Various causes for failure of implants.

### 1.2.3.1. Stainless steel implants

For medical applications non-magnetic austenitic stainless steels, especially 316 L, are being used. Composition of 316 L stainless steels is presented in Table 4 [99]. The letter L means that 316 L contains less carbon than 316 stainless steel.

**Table 4**. Composition ranges for 316L stainless steel.

| **Grade** | | **C** | **Mn** | **Si** | **P** | **S** | **Cr** | **Mo** | **Ni** | **N** |
|---|---|---|---|---|---|---|---|---|---|---|
| 316 L | Min | - | - | - | - | - | 16.0 | 2.00 | 10.0 | - |
| | Max | 0.03 | 2.0 | 0.75 | 0.045 | 0.03 | 18.0 | 3.00 | 14.0 | 0.10 |

Due to addition of molybdenum, 316 L is more resistant to corrosion than conventional steels [100]. Stainless steels are routinely used in orthopaedics due to good mechanical properties, sufficient corrosion resistance, easy processing and low cost [101]. Corrosion resistance of stainless steels is related to the formation of a thin protective chromium oxide layer on its surface. However, environment in the body is harsh and when corrosion finally begins, potentially harmful corrosion products release. This is the main reason why other more corrosion resistant alloys are preferred for permanent prosthetics [94]. Another concern related to the use of stainless steels is nickel allergies. To prevent Ni allergic reactions, an austenitic stainless steel with high nitrogen content has been developed [102]. Due to the low cost and good wear resistance many efforts are made to find modification methods of 316 L stainless steel which would eliminate it‘s disadvantages [27].

#### 1.2.3.2. Other metallic implants

Titanium, the most biocompatible metallic material, is used extensively in orthopaedics. Since pure titanium is relatively soft, it is often combined with other metals to increase its strength and rigidity. The most popular choices include titanium 6-aluminium 4-vanadium (TiAlV) and titanium 6-aluminium 7-niobium (TiAlNb) alloys. Titanium dioxide ($TiO_2$) layer which spontaneously forms on the surface of the metal makes titanium and it‘s alloys highly resistant to corrosion. However due to friction this protective film wears off quickly and expose the underlying metal to the aggressive surrounding within body. CoCr/Ti junctions were shown to release more metallic debris compared to all-titanium connections, with the debris having more potential to cause adverse tissue reactions. This might be due to the fact that CoCr/Ti junctions release mostly cobalt and chromium ions, which are more pro-inflammatory and toxic than titanium ions [103].

The wear resistance of Co alloys is higher than that of both Ti alloys and stainless steel alloys. In artificial hip joints, the head of the joint is subjected to wear. Thus, hip joints have been fabricated from Co alloys, such as Co-Cr-Mo alloys, which exhibit high strength and ductility. However, the Ni content in wrought Co-Cr alloys causes allergic reactions [95]. The comparison of various metallic biomaterials is summarised in Table 5 [95].

**Table 5**. Comparison of metallic biomaterials used in the human body.

| Metals and alloys | Selected examples | Advantages | Disadvantages | Principal applications |
|---|---|---|---|---|
| Titanium-based Alloys | CP-Ti, Ti-Al-V, Ti-Al-Nb, Ti-13Nb-13Zr, Ti-Mo-Zr-Fe | - High biocompatibility<br>- Low Young's modulus<br>- Excellent corrosion resistance<br>- Low density | - Poor tribological properties<br>- Toxic effect of Al and V on long term | - Bone and joint replacement<br>- Fracture fixation<br>- Dental implants<br>- Pacemaker encapsulation |
| Cobalt and Cr alloys | Co-Cr-Mo, Cr-Ni-Cr-Mo | High wear resistance | - Allergy consideration with Ni, Cr and Co<br>- Much higher Young's modulus than bone | - Bone and joint replacement<br>- Dental implants<br>- Dental restorations<br>- Heart valves |
| Stainless steels | 316L stainless steel | High wear resistance | - Allergy consideration with Ni, Cr and Co<br>- Much higher modulus than bone | - Fracture fixation<br>- Stents<br>- Surgical instruments |
| Others | Ni-Ti | Low Young's modulus | Ni cause allergy | - Bone plates<br>- Stents<br>- Orthodontic wires |
| | Platinum and Pt-Ir | High corrosion resistant under extreme voltage potential and charge transfer conditions | | Electrodes |

### 1.2.4. Composites for bone replacement

Since bone is natural composite consisting of organic and inorganic parts, subject of interest is synthetic composites, i.e. polymer matrix filled with ceramics, which would posses the same properties as natural bone tissue. Polymers used in composite scaffolds can be both naturally occuring and synthetic. Benefits and limitations of polymers are presented in Table 6 [104].

**Table 6**. Benefits and limitations of polymers.

| Benefits | Limitations |
|---|---|
| - Natural polymers can be derived from extracellular matrix, ensuring high biocompatibility and low toxicity.<br>- Biodegradable.<br>- Often contains biofunctional molecules on their surface.<br>- Synthetic polymers offer improved control over physical properties.<br>- Mouldable. | - Natural and synthetic polymers generally lack mechanical properties for load bearing.<br>- Pathological impurities such as endotoxin may be presented in natural plymers.<br>- Synthetic polymers are often hydrophobic and lack cell recognition sites. |

Naturally occuring polymers applied in bone tissue engineering are collagen, silk, alginate, chitosan and hyaluronic acid. Synthetic polymers for bone tissue engineering include poly(lactic acid) (PLA), poly(glycolic acid) (PGA), poly(caprolactone) (PCL), poly(ethylene glycol) (PEG), polyamide (PA), polyvilyl alcohol (PVA), teflon and other [105]. Co-polymers including poly(lactic-*co*-glycolic acid) (PLGA) have also been used. Synthetic polymers can be created with tailored pore size, porosity, degradation rate [104, 106, 107].

Recently, more attention is given to natural polymers due to better biocompatibility and biodegradability. Structure of natural polymers consists of ligands that can bind to surrounding cell surface or provide accessible enzymatic degradation sites [108].

## 1.3. CALCIUM HYDROXYAPATITE THIN FILMS DEPOSITION TECHNIQUES

Thin film deposition is a process when material is added to the substrate in the form of thin film layers. Coating is considered as thin film when its thickness is <1μ. There are two main categories of thin film deposition techniques which depend on the nature of the process: chemical and physical deposition [109, 110]. The performance of coated material strongly depends on bonding strenght between coating and substrate. Bonding strength itself is determined by adhesion and cohesion. Adhesion is an attraction between different surfaces, meanwhile cohesion is the internal strenght of a material. Figure 11 shows how the adhesive and cohesive strengths occur between substrate and coating [111].

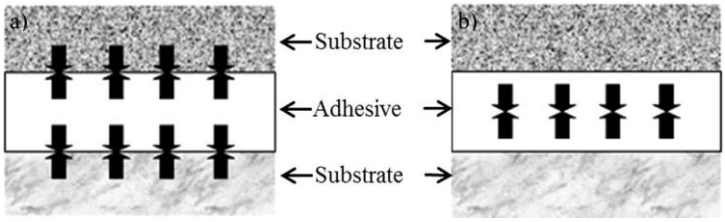


**Figure 11**. Adhesive (a) and cohesive (b) strength between adhesive and substrate.

Failure in bonding leads to the delamination of coating, implant loosening and inflamation, therefore good adhesion is extremely important for medical application [112]. Adhesion, crystallinity, thickness and other properties of coating strongly depend on deposition technique [113]. Variety of thin films deposition techniques is known. There is no unique method to classify these techniques. Depending on the viewpoint, the same process may fall into one or more classes. Each technique has its advantages and disadvantages [114]. Clinical requirements for CHAp coating are presented in Table 7 [111].

**Table 7.** CHAp coatings requirements

| **Essential** | **Requirement** |
|---|---|
| Ca/P ratio | 1.67-1.76 |
| Phase purity | 95% minimum |
| Crystallinity | 62% minimum |
| Tensile strength | >50.8 MPa |
| Shear strenght | >22 MPa |
| Density | 2.98 g/cm3 |

### 1.3.1. Sol – gel technique

Synthesis of CHAp via sol-gel route has been widely studied using variety of precursors [115-117]. Sol-gel technique has strong advantages over other deposition techniques such as low cost, simple set up, ability to coat complex shapes. Coatings achieved via sol-gel route are thin, pure and has good crystallinity [118, 119]. In addition, this technique offers a molecular-level mixing of the calcium and phosphorus precursors therefore better chemical

homogeneity can be achieved [117]. Two methods are used for the deposition of sol-gels: spin-coating and dip-coating.

### 1.3.1.1. Spin-coating method

Spin coating is used to produce thin (<1 μm) and uniform coatings on flat surfaces [120]. The coating fluid is dropped at the center of the target and the stage starts rotating. The applied solution is distributed over the surface via centrifugal force. The thickness of the film mainly depends on the viscosity of coating solution, solvent evaporation rate and rotation speed. Generally, higher rotation speed produces thinner coatings [121]. Illustration of spin-coating method is presented in Figure 12 [122]. The substrate must be kept spinning until the film is fully dry. For most solvents, including water and ethanol, 30 seconds is more than enough to evaporate [123]. One of the disadvantages of spin coating is the loss of material because excessive fluid is dispersed beyond the target by the centrifugal force of the rotation. This is not an issue for research in laboratory, but serious drawback for industrial application.

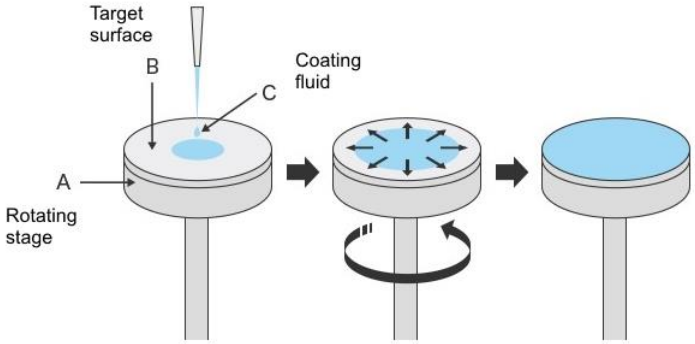


**Figure 12.** Illustration of spin-coating method.

### 1.3.1.2. Dip-coating method

Dip-coating is deposition of liquid film via controlled immersion and withdrawal of a substrate from solution. Dip-coating procedure can be separated into four stages: 1. Immersion (substrate is immersed into sol-gel solution at a constant speed). 2. Dwelling (substrate remains immersed into solution). 3. Withdrawal (substrate withdrawal at constant speed. The faster withdrawal, the thicker layer is obtained). 4. Drying.

All these stages are important but the most critical ones are withdrawal and drying. Visualisation of dip-coating procedure is presented in Figure 13 [124].

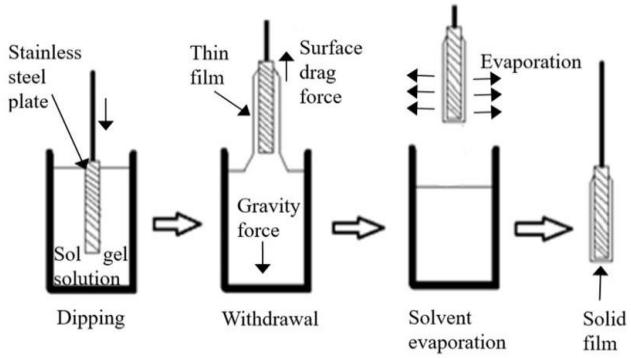


**Figure 13.** Dip-coating process.

Dip-coating process can be automated and equipment adapted to coat large and complex shape substrates. However this method has some disadvantages such as „wedge effect“ when thin film thickness varies from top to bottom and bulky edges developed on the bottom from dripped solution [125].

### 1.3.2. Other chemical techniques

There are several other groups of chemical thin films deposition techniques [61]:

1. Biomimetic.
2. Chemical vapor deposition (CVD).
3. Atomic layer deposition (ALD).

Biomimetic deposition is variation of wet-chemical method and involves soaking metal implants in simulated body fluid at a physiologic temperature and pH. Despite advantages such as low processing temperatures, ability to coat complex shapes and incorporate bone growth factors biomimetic method has serious disadvantages. The process requires replenishment and a constant pH to maintain supersaturation for apatite crystal growth. This operation is very complicated and usually lead to local precipitation and uneven coatings. Such long and difficult process can not be accepted in the coating prostheses industry [126].

CVD is process where coating is deposited from a vapor by a chemical reaction occuring on the substrate surface [127]. There are many processes falling within CVD description such as plasma-enhanced CVD (PECVD), atmospheric pressure CVD (APCVD), low pressure CVD (LPCVD), very low pressure CVD (VLPCVD), etc. [109, 128]. CVD has several advantages such as ability to coat complex shape substrates, high deposition rate and cost-effectiveness in comparison to physical vapor deposition. The disadvantages of CVD are limited selection of precursors (they should be volatile near-room temperatures), hazardous byproducts (for example CO), deposition at eleveated temperatures which limit selection of substrates [129].

ALD also known as atomic layer epitaxy is advanced variation of traditional CVD. ALD allows deposition at the atomic or molecular level and offers better coating uniformity and conformity on complex substrates compared with conventional CVD [130].

### 1.3.3. Physical techniques

#### 1.3.3.1. Physical vapor deposition

Physical vapor deposition (PVD) is the largest family of processes used to deposit thin coatings on various substrates. PVD consists of three essential steps [131]: 1. Changing the phase of material from solid to vapor (sublimation). 2. Transportation of the vapor to the substrate. 3. Condensation of vapor on a substrate surface as a film. Many various PVD approaches are described in the literature. Some of them will be discussed shortly in this part of dissertation.

*Vacuum evaporation* is one of the most simplest among all PVD techniques. Material is heated in vacuum until it evaporates and evaporated atoms hit other gas molecules or solid surface. Vacuum inside is supposed to eliminate other gas molecules and ensure that only substrate is targeted by evaporated atoms. When atoms reach surface of a subtrate, they looses energy thus can not remain in evaporated state. An adhesion of coatings is not as good as other PVD processes [132, 133]. Diagram of evaporation is presented in Figure 14 [134].

*Sputtering* is a process when atoms from source material are ejected by high energy particles (such as ionized gas). Films can be sputtered without chemical composition change. However deposition rates of sputtering are slow and traces of entrapped gas can be found in final product which affect mechanical properties of coating [135].

*Ion plating* is combination of evaporation and sputtering. The bombardment prior to deposition cleans the surface. This method is suitable for complex shapes and has such advantages as high deposition rate, good coverage and adhesion [133, 136].

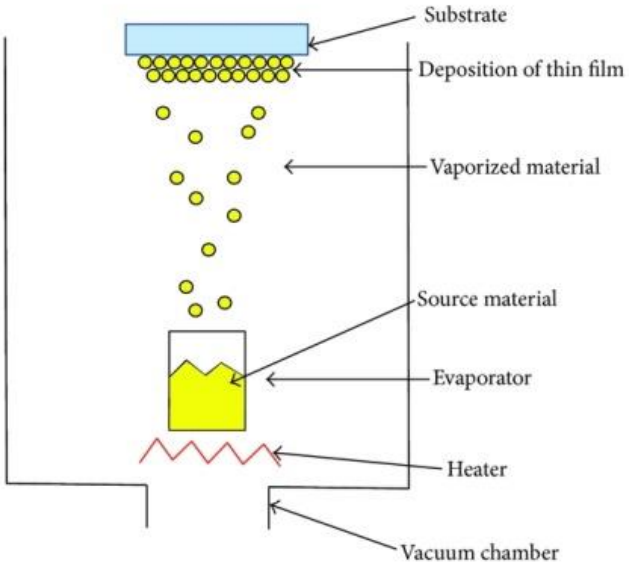


**Figure 14**. Diagram of thermal evaporation.

### 1.3.3.2. Spraying processes

Another group of PVD processes is *spraying*. Spraying is high temperature process when molten or semimolten particles are sprayed at high speed on the substrate surface. According to heating source, spraying is divided into plasma, flame, electrical arc and detonation-gun spraying [137]. Plasma spraying is the most popular and the only clinically accepted implant coating method approved by Food And Drug Administration (FDA) in USA [16].

The atmospheric plasma spraying process (APS) is one of the most accepted methods for the preparation of bioactive coatings [138]. APS technique offers advantages of high deposition rate, low-cost and controllable microstructure of the coatings. The main drawbacks of APS are relatively poor adhesion which leads to coating delamination, structural changes in the microstructure of the coating and the decomposition of the CHAp particles during spraying, which leads to the formation of new phases,

such as α-tri-calcium phosphate (α-TCP), β-tri-calcium phosphate (β-TCP) and tetra-calcium phosphate (TTCP), or even calcium oxide (CaO). Amorphous calcium phosphates (ACP) phases are usually formed within the APS-deposited CHAp coating due to the rapid cooling of the droplets on the substrate material [138, 139]. The indirect method of plasma spray applies melting and spraying onto the surface by an electric arc [111].

## 2. EXPERIMENTAL

### 2.1. REAGENTS AND MATERIALS

Reagents and materials used for the preparation of CHAp coatings were following:

- Calcium acetate monohydrate (99.9%), Fluka (USA);
- Phosphoric acid (concentration 85.0%), Reachem (USA);
- 1,2-ethanediol (99.0%), Alfa Aesar (USA);
- Ethylenediaminetetraacetic acid (EDTA) (99.0%), Alfa Aesar (USA);
- Triethanolamine (TEA) (99.0%), Merck (Germany);
- Poly(vinyl alcohol) (PVA) (99.5%), Aldrich (USA);
- Acetone;
- Distilled water;
- AISI 316 L stainless steel plates (rectangular (20 x 10 x 0.5 mm) and round (20 x 0.5 mm)), Goodfellow (England);
- AISI 316 L stainless steel rounds (10 x 0.5 mm) with TiN (2-3 μm) coating, Goodfellow (England).

### 2.2. PREPARATION AND MODIFICATION OF STAINLESS STEEL SURFACE

Three types of surface preparation of 316 L stainless steel were made:

1. Smooth surface
2. Surface modified by formation of the transverse and longitudinal patterned roughness.
3. Surface modified with titanium nitride (TiN) sublayer.

*Stainless steel with smooth surface*. Surface of 316 L stainless steel plates were cleaned with acetone in ultrasonic cleaner for 15 minutes and then air dried. Rectangular plates of 20 x 10 x 0.5 mm were used for dip-coating and circle plates of 20 x 0.5 mm diameter for spin-coating.

*Surface modified by formation of the transverse and longitudinal patterned roughness*. The surface of square plates of 10 mm × 10 mm × 0.5 mm was modified by formation of transverse and longitudinal patterned roughness prior to the spin-coating of the Ca–P–O sol-gel solution. A sandpaper (2500 grit) was used to obtain the pattern. Two pieces of sandpaper were lightly rubbed against each other to remove any possible large particles to protect the

surface from gouging. Then the metal was roughened with the sandpaper applying medium pressure from an index finger in two directions 90° apart. A schematic diagram of the preparation of the CHAp coatings is presented in Figure 15. After procedure plates were cleaned with acetone in ultrasonic cleaner for 15 minutes and then air dried.

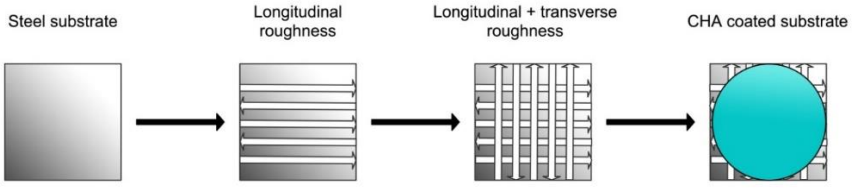


**Figure 15**. A schematic diagram of the preparation of CHAp coatings.

*Surface modified with titanium nitride (TiN) sublayer*. Round 10 x 0.5 mm 316 L stainless steel plates with commercially applied TiN layer (2-3 μm thickness) were used for experiments. Plates were cleaned with acetone in ultrasonic cleaner for 15 minutes and then air dried.

## 2.3. SYNTHESIS OF CALCIUM HYDROXYAPATITE COATINGS

Calcium acetate monohydrate ($Ca(CH_3COO)_2 \cdot H_2O$) and phosphoric acid ($H_3PO_4$) were used as starting materials for the synthesis of CHAp coatings, respectively. 5.2854 g (0.03 mol) of calcium acetate monohydrate were dissolved in 40 ml of distilled water and mixed with 4 ml of complexing agent 1,2-ethanediol. To this solution, 9.6439 g (0.033 mol) of ethylenediaminetetraacetic acid (EDTA) deprotonated with 24 ml of triethanolamine was slowly added. After 10 h of stirring, 1.23 ml of phosphoric acid diluted with 20 ml of distilled water was added to the solution. After stirring for 24 h, 25 ml of the obtained gel were mixed with 15 ml of 3% poly(vinyl alcohol) (PVA). The obtained solution was stirred in a beaker covered with watch glass at room temperature and was used for coating of commercial 316L stainless steel substrates with various surface modifications.

Dip-coating was performed with dip-coater D KSV. Spin-coating was performed with spin-coater P6700.

### 2.3.1. Synthesis of CHAp thin films with low number of layers using spin-coating and dip-coating techniques

Dip-coating and spin-coating techniques were employed to produce sol-gel derived CHAp coatings. Stainless steel rectangles *with smooth surface* were dip-coated in the sol solution, with immersing (85 mm/min) and a withdrawal rates (40 mm/min). For spin-coating, approximately 0.1 ml of coating solution was placed on top of the stainless steel rounds *with smooth surface* using syringe and then spin coated at 2000 RPM for 60 s in air. Both rectangle and circle substrates were annealed 5 times following the same procedures accordingly. 1$^{st}$ and 5$^{th}$ layers were heated in an oven at 1000 °C for 5 h. 2$^{nd}$, 3$^{rd}$ and 4$^{th}$ layer of CHAp were heated on a hot plate for 1 h at 400 °C.

### 2.3.2. Synthesis of CHAp thin films with large number of layers at lower temperature using spin-coating and dip-coating techniques

Dip-coating and spin-coating techniques were employed to produce sol-gel derived CHAp coatings. Stainless steel rectangles *with smooth surface* were dip-coated in the sol solution, with immersing (85 mm/min) and a withdrawal rates (40 mm/min). For spin-coating, approximately 0.1 ml of coating solution was placed on top of the stainless steel rounds *with smooth surface* using syringe and then spin coated at 2000 RPM for 60 s in air. Both rectangle and circle substrates were repeatedly coated 5, 15 and 30 times following the same procedures accordingly and each time annealed at 850 °C for 5 h in an oven.

### 2.3.3. Synthesis of CHAp thin films deposited on roughened stainless steel surface using spin-coating technique

For spin-coating, approximately 0.5 ml of coating solution was placed on top of the stainless steel surface *modified by formation of the transverse and longitudinal patterned roughness* using syringe and then spin coated at 2000 RPM for 60 s in air. Substrates were repeatedly coated 15, 20, 25 and 30 times following the same procedures accordingly and each time annealed at 850 °C for 5 h in an oven.

### 2.3.4. Synthesis of CHAp thin films on stainless steel substrate modified with TiN sublayer using spin-coating technique

For spin-coating, approximately 0.5 ml of coating solution was placed on top of the stainless steel surface *modified with TiN sublayer* using syringe and then spin coated at 2000 RPM for 60 s in air. Substrates were repeatedly coated 1, 3, 5, 7 and 10 times following the same procedures accordingly and each time annealed at 850 °C for 5 h in an oven.

## 2.4. MATERIALS CHARACTERISATION

X-ray diffraction (XRD) analysis was performed with a D8 Focus diffractometer (Bruker AXS Inc., Germany) with a LynxEye detector (Bruker, USA) using Cu Kα radiation. The measurements were recorded at the rate of 0.02 1.5 º/min.

The changes in the layers were evaluated using diffuse reflectance infrared Fourier transform spectroscopy (DRIFTS) with a FTIR Spectrum BX II spectrometer (Perkin–Elmer, USA). Spectra were acquired from 100 scans. For collection of background spectrum bare stainless steel plate annealed at 850 ºC for 5 h was used.

The microstructure and morphology of the obtained samples were investigated using a SU-70 scanning electron microscope (SEM) (Hitachi, Japan) and BioScope Catalyst atomic force microscope (AFM) (Bruker, Germany). Before SEM analysis samples were coated with a thin layer of platinum to avoid charge accumulation on the surface of the specimen and improve image quality.

For the evaluation of the hydrophobicity of the CHAp coatings, the contact angle measurements were performed using contact angle meter (CAM) (CAM 100, KSV, USA). Distilled water was used for CAM measurements.

Raman spectra were measured on Ramboss 500i micro spectrometer (Taiwan) and inVia Raman (Renishaw, United Kingdom) spectrometer. The overall accumulation time was 400 s. Position of the Raman bands on the wavenumber axis was calibrated by the polystyrene film standard spectrum.

XPS measurements of the synthesized samples were carried out employing the JPS-9030 spectrometer (JEOL, Japan).

For tribological measurements, a TriTec SA CSM Tribometer (Anton Paar, Switzerland) was used with a ball-on-plate linearly reciprocal configuration. A corundum ball (RGP International Srl, Italy) of 6 mm (outer diameter) was held stationary, and the load was 1 or 5 N. Stainless steel substrates coated

with calcium hydroxyapatite were used as the moving part, which was mounted on a pre-installed tribometer module. Linear reciprocal motion within the amplitude of 2 mm was maintained resulting in a 4 mm range and 8 mm of the total distance for one reciprocal friction cycle. At a velocity of 2 cm/s, each friction cycle produced approx. 100 data points of the ‘instantaneous’ coefficient of friction (COF).

# 3. RESULTS AND DISCUSSION

## 3.1. SYNTHESIS AND CHARACTERIZATION OF NANOSTRUCTURED CHAp THIN FILMS WITH LOW NUMBER OF LAYERS USING SPIN-COATING AND DIP-COATING TECHNIQUES

### 3.1.1. XRD, FTIR and contact angle measurements

The phase purity of the CHAp films was determined using X-ray diffraction (XRD) analysis. For spin-coated and dip-coated samples after first immersing, withdrawal and annealing procedure the peaks attributable to the Fe, $Fe_2O_3$ and $Fe_3O_4$ crystalline phases were observed in the XRD patterns. The repetition of immersing, withdrawal and annealing procedures for 5 times slightly changed phase composition of the coatings. However, after five dip-coating procedures non-intensive peaks attributable to the $Ca_{10}(PO_4)_6(OH)_2$ phase was already determined. Figure 16 represents XRD patterns of CHAp films fabricated on stainless steel substrate and obtained from CHAp aqueous precursor solution using dip-coating and spin-coating techniques.

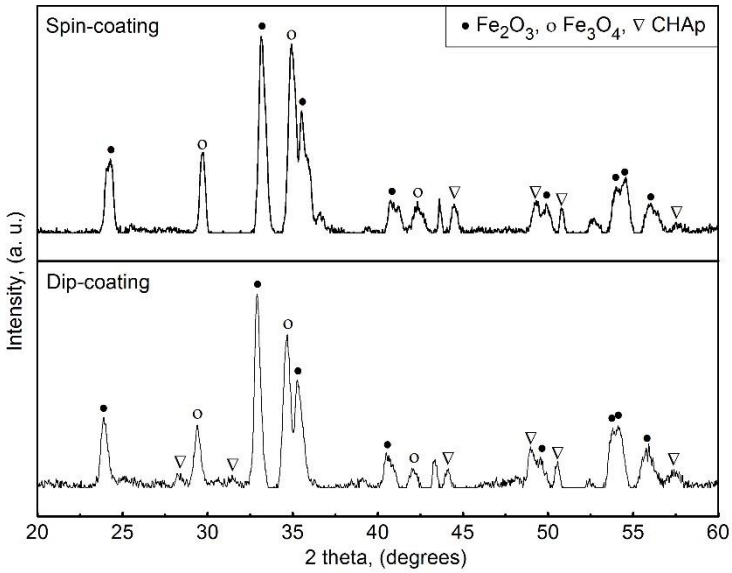


**Figure 16.** The fragments of XRD patterns of CHAp gels annealed on the stainless steel substrate for 5 h in air at 1000 °C after five dipping (at bottom) and spinning (at top) procedures.

Sample obtained using spin-coating technique has less diffraction peaks attributable to CHAp phase. Thus, from the XRD measurements it seems that dip-coating technique was more favourable for the fabrication of CHAp with low number of layers on the surface of stainless steel.

The FTIR spectra of the corresponding films obtained from Ca-P-O gel using spin-coating and dip-coating techniques are presented in Figure 17.

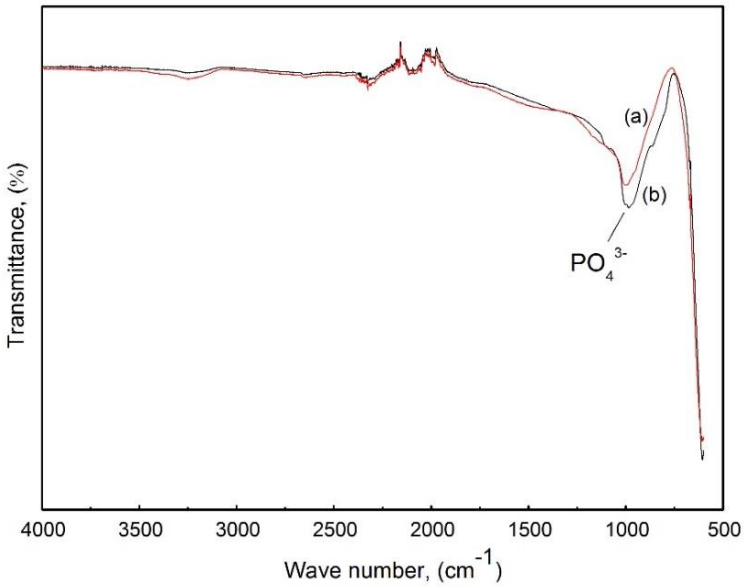


**Figure 17.** FTIR spectra of CHAp gels annealed on the stainless steel substrate for 5 h in air at 1000 °C after five spinning (a) and dipping (b) procedures.

In both FTIR spectra of the samples obtained after five immersing, withdrawal and annealing procedure the absorption peaks in the range of 1100-950 $cm^{-1}$ attributable to the P-O vibrations in $PO_4^{3-}$ ($Ca_{10}(PO_4)_6(OH)_2$) [140] are clearly visible. Intensive absorption lines located at ~600 $cm^{-1}$ unambiguously could be attributed to Ca-O vibrations in apatite structure. Therefore the FTIR spectra indicate the presence of phosphates in the samples. Additionally, the peak attributable to the P-O vibrations is more intensive in the sample obtained by dip-coating technique.

The hydrophobicity of the produced thin films by two techniques using sol-gel chemistry synthesis approach was estimated by the contact angle measurments (CAM). The obtained results are presented in Table 8. As seen the determined contact angle of water drop on the surface of stainless steel is

equal 107.34 °. However, the contact angle decreased dramatically already after first dipping (21.95 °) or spinning (34.73 °) procedures. The values of contact angle were increased after five immersing, withdrawal and annealing procedures, however, the surfaces of both samples remained hydrophilic. The formation of hydrophilic surfaces of coatings are associated with formation of CHAp crystallites which contains the hydrophilic hydroxyl $OH^-$ groups in the chemical composition. Thus, these results are in a good agreement with observed ones by XRD analysis and FTIR spectroscopy.

**Table 8.** Results of CAM obtained on un-coated stainless steel and CHAp films obtained using different techniques and coating times.

| Coating technique | Number of layers | Contact angle, degrees |
|---|---|---|
| - | 0 | 107.34 |
| Dip-coating | 1 | 21.95 |
| Dip-coating | 5 | 50.65 |
| Spin-coating | 1 | 34.73 |
| Spin-coating | 5 | 30.64 |

### 3.1.2. Microscopical characterization

The surface properties of synthesized coatings were investigated using scanning electron microscopy (SEM) and atomic force microscopy (AFM). In Figure 18 the SEM micrographs of stainless steel substrate and the CHAp samples obtained after first coating and heating procedures are presented.

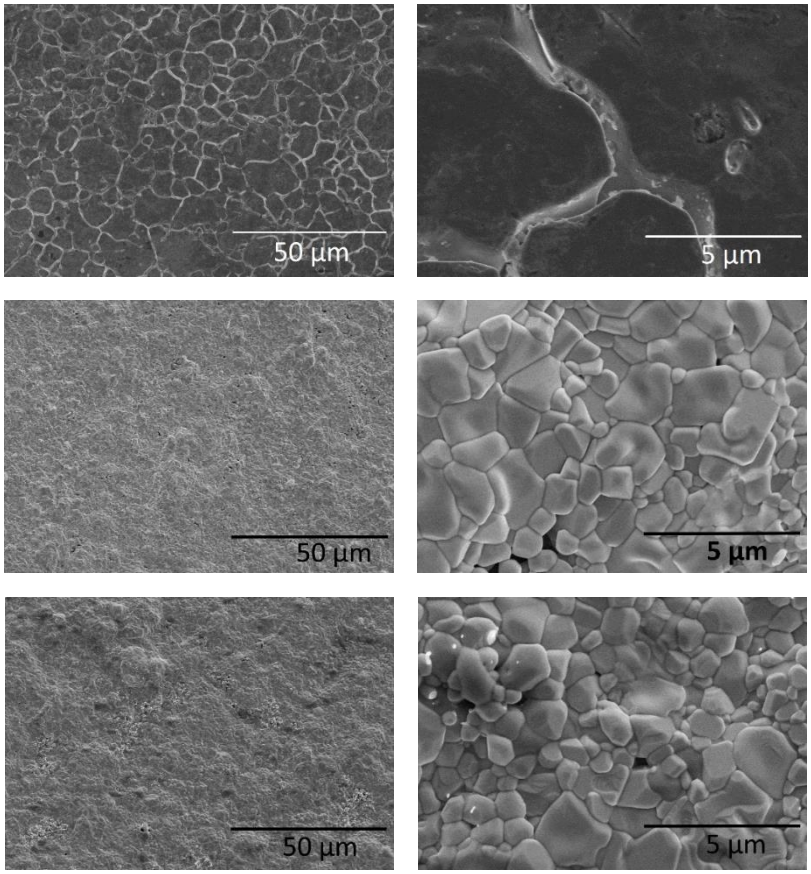


**Figure 18.** SEM micrographs of stainless steel substrate (at top) and samples obtained after one dipping (at middle) and spinning (at bottom) procedures using CHAp gel and obtained at different magnifications.

As seen, the surface of stainless steel substrate clearly expressed with small cracks and differs from the coated samples. However, the main morphological features of CHAp films (1 layer) obtained by dip-coating and spin-coating techniques are very similar. The homogeneous and smooth surfaces were obtained with formation of non-uniform irregular size particles. An average grain size of 0.5-2 µm could be evidently determined in the SEM micrographs obtained at higher magnification.

The SEM micrographs of thin films containing 5 layers of CHAp gel precursor are presented in Figure 19.

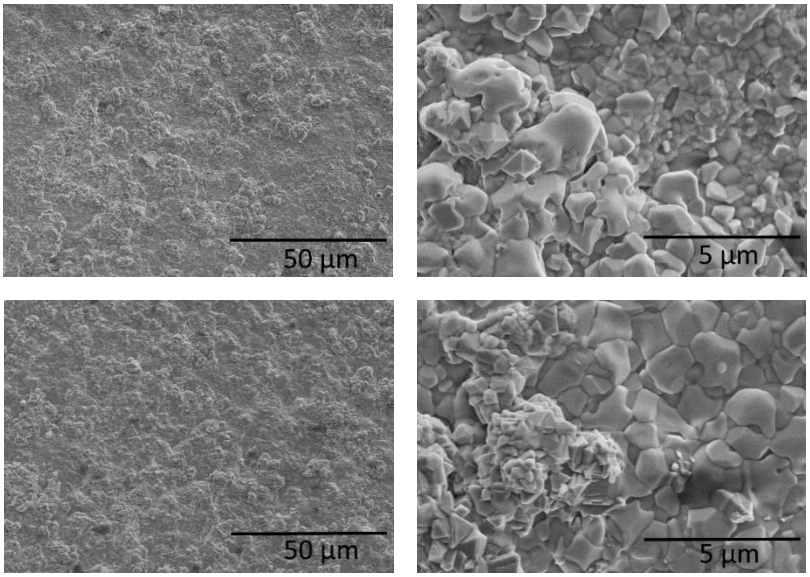


**Figure 19**. SEM micrographs of samples obtained after five dipping (at top) and spinning (at bottom) procedures using CHAp gel and obtained at different magnifications.

Again, the negligible changes in the surface morphology of specimens prepared using two different preparation techniques are evident. The formation of network of irregular size plate-like particles (probably, iron oxides) as was determined in the samples with 1 layer could be detected as well as in the samples obtained after five dipping and spinning procedures. However, the new differently shaped particles could be seen on the surfaces obtained after five dipping and spinning procedures. The "necked" to each other particles of CHAp forming bigger agglomerates (1-2.5 µm) are seen in the sample obtained by dip-coating technique. However, less than 500 nm plate-like crystallites have formed during spin-coating fabrication of thin films.

The same conclusions obviously could be deduced and from the results of AFM measurements (see Figures 20 (samples containing 1 layer of CHAp) and 21 (samples containing 5 layers of CHAp)). As seen, the surface morphology and roughness are changing monotonically with increasing the number of Ca-P-O gel layers on the substrate. However, the surface roughness is very similar for the samples obtained by both synthesis techniques.

In conclusion, the CHAp films with low number of layers could be produced on stainless steel substrate using an aqueous sol-gel method by both

dip- and spin-coating techniques. However, the samples are not monophasic and the homogeneity could be also increased, probably, with increasing number of immersing, withdrawal and annealing procedures.

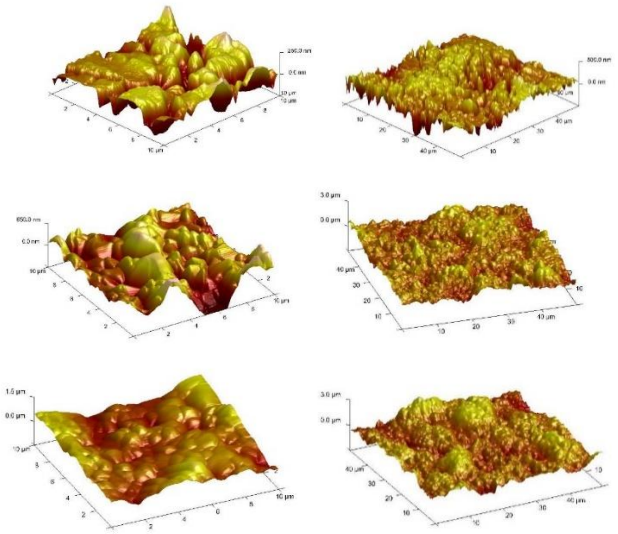

**Figure 20.** AFM images of different areas of stainless steel substrate (at top) and samples containing 1 layer of CHAp gel deposited by dip-coating (at middle) and spin-coating (at bottom) techniques.

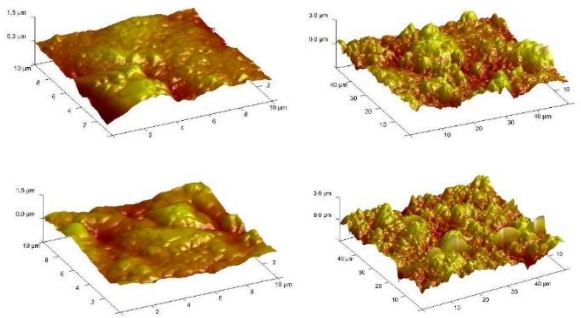

**Figure 21.** AFM images of different areas of samples containing 5 layers of Ca-P-O gel deposited by dip-coating technique (at top) and spin-coating technique (at bottom).

## 3.2. SYNTHESIS AND CHARACTERIZATION OF NANOSTRUCTURED CHAp THIN FILMS WITH LARGE NUMBER OF LAYERS AT LOWER TEMPERATURE USING SPIN-COATING AND DIP-COATING TECHNIQUES

### 3.2.1. XRD, FTIR and contact angle measurements

The phase composition of the fabricated coatings was determined by XRD analysis. Figure 22 shows X-ray diffraction patterns of CHAp films synthesized using spin-coating technique.

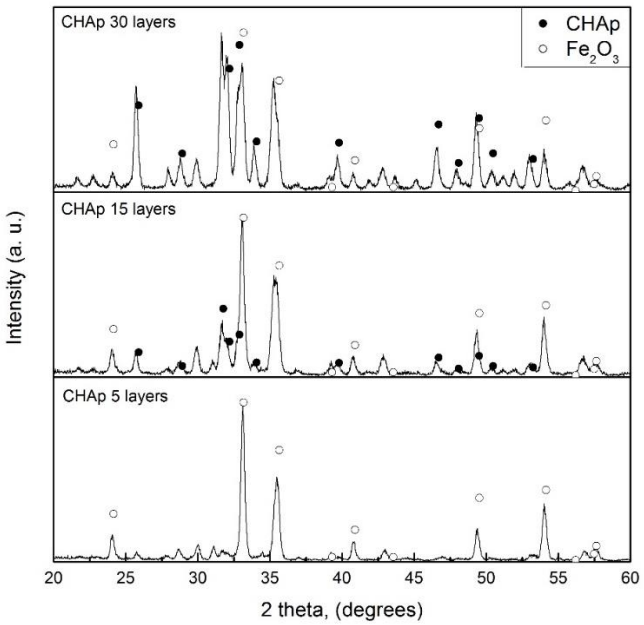


**Figure 22**. XRD patterns of C-P-O gels annealed at 850 °C for 5 h after 5, 15 and 30 spinning procedures. Diffraction peaks are marked: ● is $Ca_{10}(PO_4)_6OH_2$ , ○ is $Fe_2O_3$.

The influence of the spinning and annealing procedures on the formation of CHAp phase is clearly seen. After five spinning and annealing procedures the only phase of $Fe_2O_3$ ($2\theta \approx 24.5^{o}$, $33.5^{o}$, $35.2^{o}$ and $41.5^{o}$; ICSD [033-0664]) could be determined. As seen from Figure 22, the formation of CHAp phase ($2\theta \approx 31.8^{o}$; PDF [9-432]) started after repeating spinning and annealing procedure for 15 times. However, the $Fe_2O_3$ phase remained as dominant

phase in the final product. Diffraction peaks attributable to CHAp are well resolved and intensive sufficiently in the sample obtained after 30 spin-coating procedures. On the other hand, the intensity of reflections attributable to the side iron oxide phase remains on the same level as in the case of CHAp sample prepared using 15 spin-coating procedures.

Very similar results were obtained during the preparation of CHAp thin films using dip-coating synthesis approach. The XRD patterns of CHAp speciments synthesized using dip-coating technique are shown in Figure 23. The intensity of diffraction lines attributable to the $Ca_{10}(PO_4)_6OH_2$ phase increases with increasing number of spinning and annealing procedures. From the XRD measurements we can conclude that both spin-coating and dip-coating techniques are suitable for the fabrication of CHAp on the surface of stainless steel.

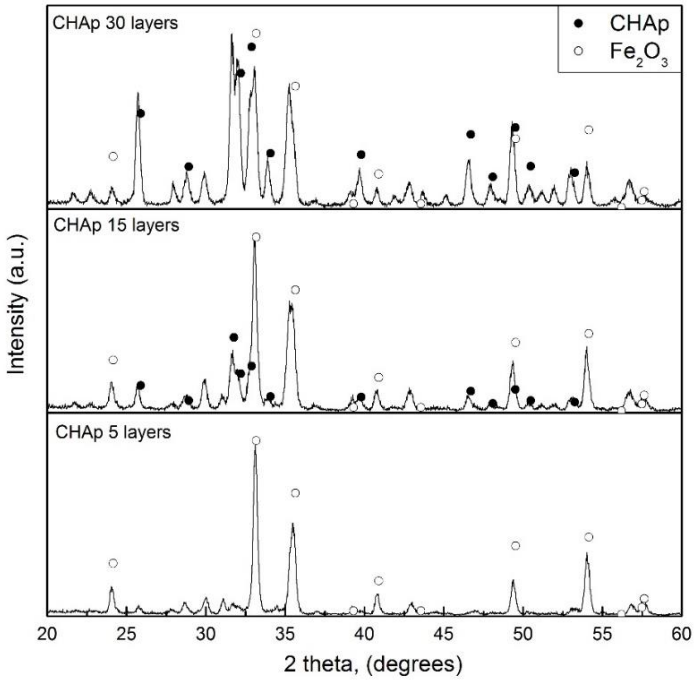


**Figure 23**. XRD patterns of Ca-P-O gels annealed at 850 °C for 5 h after 5, 15 and 30 dipping procedures. Diffraction peaks are marked: ● is $Ca_{10}(PO_4)_6OH_2$ , ○ is $Fe_2O_3$.

The FTIR spectra of the sol-gel derived CHAp coatings and obtained by spin- and dip-coating procedures are shown in Figures 24 and 25, respectively. The characteristic absorption lines of the P-O vibrations in $PO_4^{3-}$ ($Ca_{10}(PO_4)_6(OH)_2$) in the range of 1100-950 $cm^{-1}$ are clearly visible in both spin-coated and dip-coated samples obtained after 15 coating and annealing procedures [141, 142]. The broad band ranging from 3600 to 2800 $cm^{-1}$ with a peak at 2987 $cm^{-1}$ can be attributed to O-H vibration of adsorbed water during the exposure of dried samples to air [143, 144]. Bands within 1490 – 1280 $cm^{-1}$ indicates presence of carbonate from the air [145]. The observed similarity of FTIR spectra of spin-coated and dip-coated samples is in a good agreement with XRD results and confirms that both deposition techniques can be successfully applied to prepare CHAp thin films on stainless steel substrate.

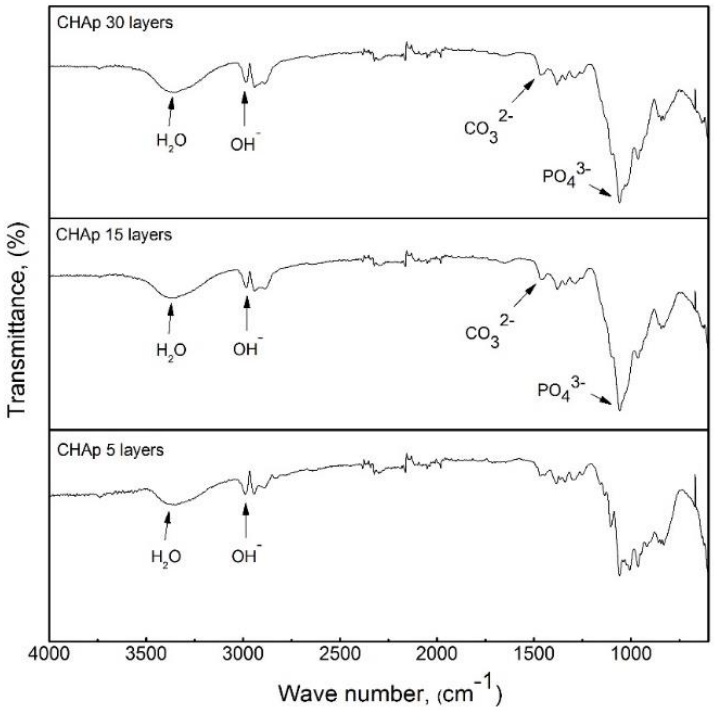


**Figure 24.** FTIR spectra of C-P-O gels annealed at 850 °C for 5 h after 5, 15 and 30 spinning procedures.

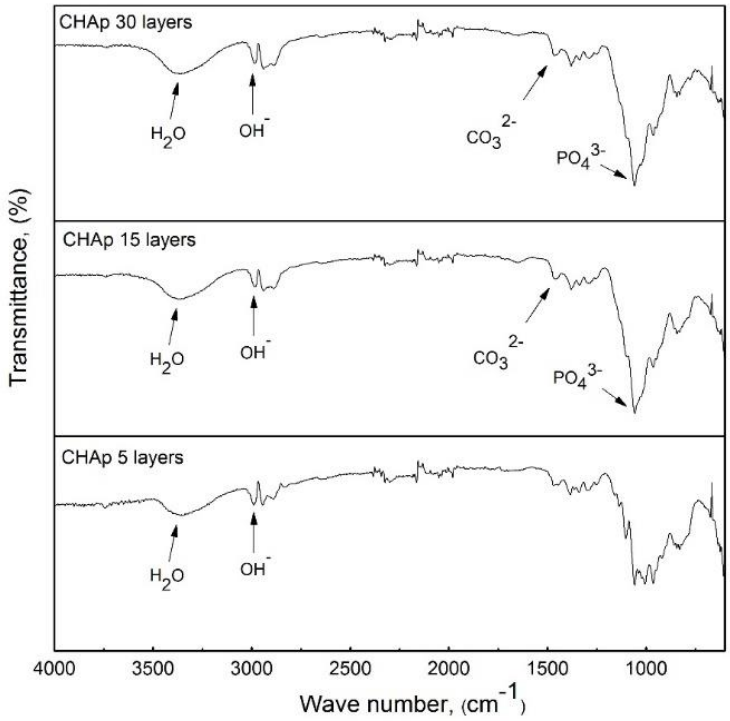


**Figure 25.** FTIR spectra of C-P-O gels annealed at 850 °C for 5 h after 5, 15 and 30 dippping procedures.

Contact angle measurements were performed to estimate hydrophobic and hydrophilic properties of CHAp coatings synthesized with large number of layers. The results of contact angle measurements are presented in Figure 26. The contact angle value determined for stainless steel substrate was 107.3°. Interestingly, the wettability of CHAp coatings depends on a number of layers of samples obtained both dipping and spinning techniques. The contact angle of dip-coated samples decreased from 78.6 ° up to 69.0 ° with increasing the number of layers from 15 to 30. However, spin-coated sample had different tendency in the change of contact angle. This tendency must be related to the difference in surface porosity among samples which are evident in SEM images. The contact angle of spin-coated samples increased from 56.4 ° up to 78.8 ° with increasing the number of layers from 15 to 30.

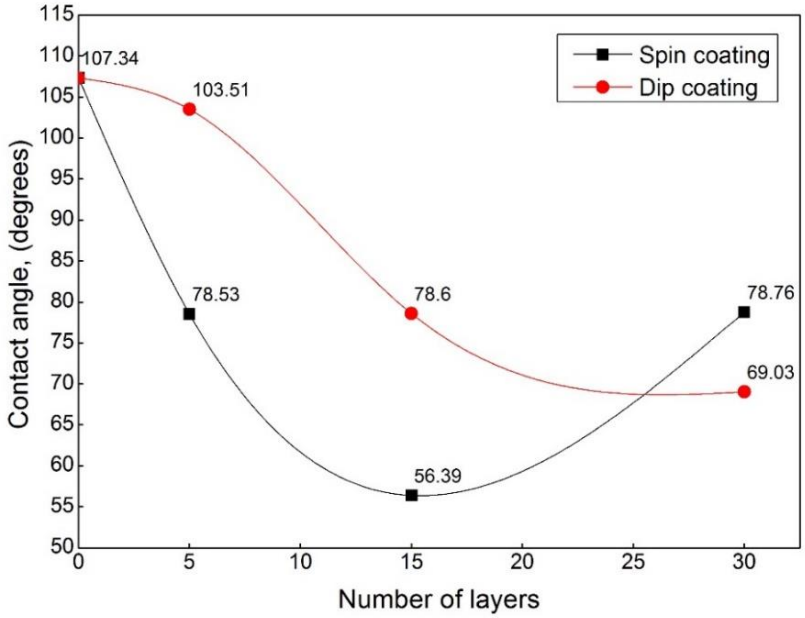


**Figure 26.** Contact angle measurements of spin-coated and dip-coated samples.

The coatings obtained using both spin-coating and dip-coating techniques were hydrophilic which is in a good agreement with previous results. The increased hydrophilicity of CHAp coated stainless steel compared to uncoated stainless steel was determined. Hence, the CHAp coated stainless steel with enhanced wettability can accelerate osseointegration, i. e. structural and functional connection between living bone and the surface of a load-bearing artificial implant [146].

### 3.2.2. Microscopical characterization

The surface morphological properties of synthesized CHAp coatings were investigated using scanning electron microscopy and atomic force microscopy. The SEM micrographs of the 316L stainless steel plate obtained at different magnification are shown in Figure 27.

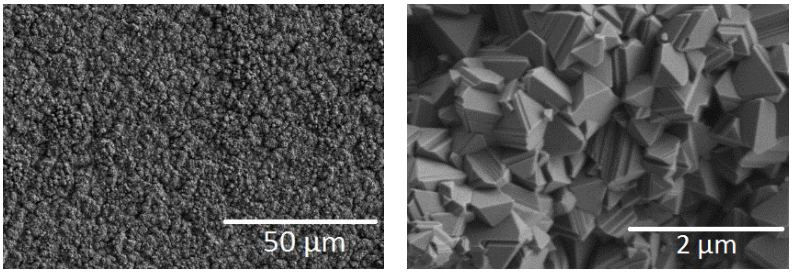


**Figure 27.** SEM micrographs of the 316L stainless steel substrate annealed at 850 ºC.

Surprisingly, the surface of the substrate is rough and composed of pyramidal crystallites. Figure 28 represents the SEM micrographs of both samples containing 5 layers of precursor gel and heated at 850 ºC.

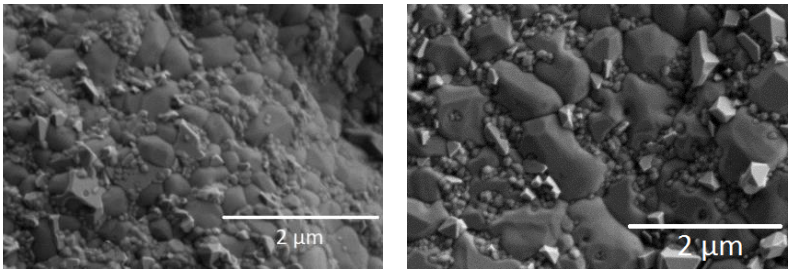


**Figure 28.** SEM micrographs of CHAp samples containing 5 layers and obtained by spin-coating (at left) and dip-coating (at right) techniques.

The SEM images clearly differ from the SEM micrographs of substrate. It is evident that the stainless steel substrate is more evenly coated with synthesis product using spin-coating procedure. In comparison, the network of irregularly shaped particles (probably, iron oxide) could be observed in the SEM micrograph of the dip-coated sample.

The SEM micrographs of the samples containing 15 layers of CHAp and obtained at different magnification are presented in Figure 29.

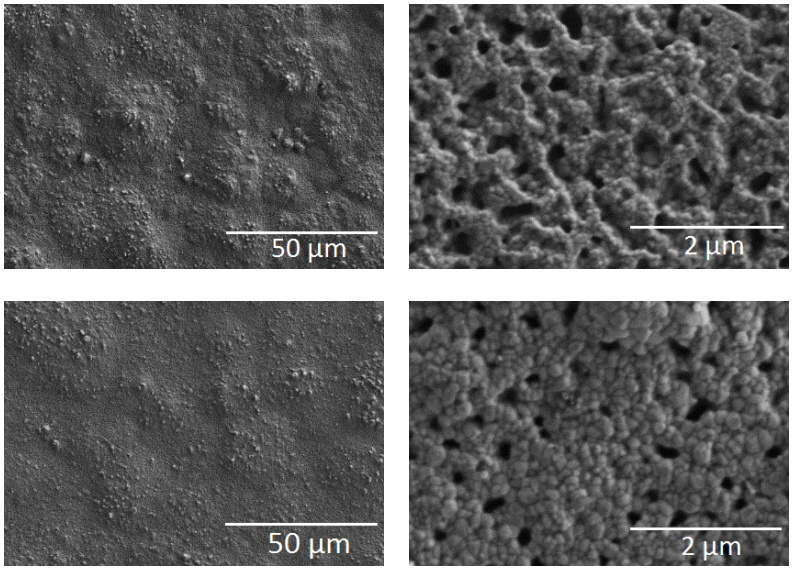


**Figure 29.** SEM micrographs of CHAp samples containing 15 layers and obtained by spin-coating (at top) and dip-coating (at bottom) techniques.

The both stainless steel surfaces are homogenously coated by calcium hydroxyapatite showing the formation of porous microstructure. However, the changes in surface morphology of CHAp samples prepared using spin-coating and dip-coating techniques are visible. The surface quality after 15 procedures is slightly better for the CHAp sample obtained via dip-coating procedure. As seen, the synthesized thin film using dip-coating technique is composed of evenly distributed well interconnected spherical particles less than 200 nm in size.

Figure 30 shows SEM micrographs of CHAp thin films obtained after 30 coating and annealing procedures.

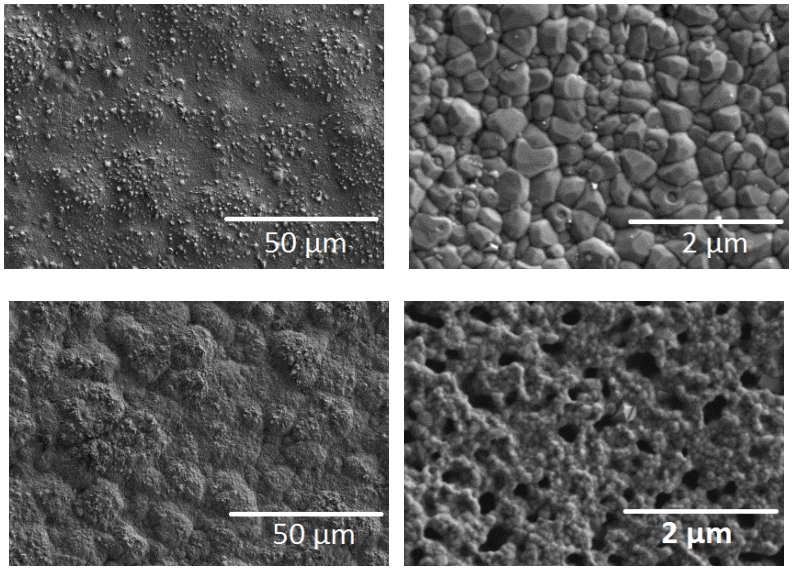


**Figure 30.** SEM micrographs of CHAp samples containing 30 layers and obtained by spin-coating (at top) and dip-coating (at bottom) techniques.

The coatings appear uniform, crack free and completely covering the substrates. The SEM images obtained at higher magnification indicated different surface morphology of spin-coated and dip-coated samples. The SEM image of spin-coated sample is homogeneous and composed of nano-scaled particles. The individual particles are about 100-300 nm in size. These particles appear to have fused together to form stone-like deposits [147]. Interestingly, the dip-coated sample is not fully dense and remains porous with coral microstructure. The pores appear to be of a nano-scale size range. SEM results showed that despite the structural similarities of coatings, some morphological features are different and these changes were affected by coating technique.

With both preparation techniques the stainless steel substrates were fully covered by CHAp, despite different texture of thin films was obtained. CHAp with coral structure has considerable success considering its porous structure. It is similar to the human cancellous bone and the material could form chemical bonds with bone and soft tissue *in vivo* [148]. Such type of implants show enhanced biological interactions and hence accelerate fixation to bone [149]. *In vitro* tests of CHAp coatings with homogeneous particle distribution also revealed chemical reaction of the particles with the surrounding body fluid, considered as a signal of bioactivity [150]. Additionally, dense CHAp ceramic exhibits a higher fracture toughness having improved mechanical

properties [151, 152]. Moreover, both samples appear to be good candidates for biocompatible drug carriers, since they can be resorbed by cells and promote new bone formation [153-155].

Atomic force microscopy was also used as additional tool to investigate the surface morphology of the CHAp coatings. The AFM images of the uncoated stainless steel substrate and different CHAp coatings are presented in Figures 31-34. The AFM 3D images of different areas of as-prepared stainless steel substrate are depicted in Figure 31.

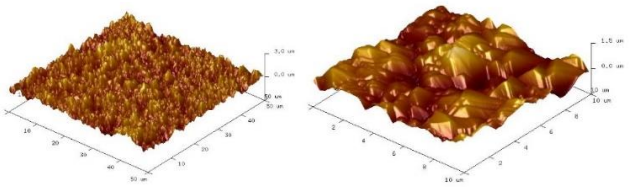

**Figure 31.** AFM images of different areas of the as-prepared stainless steel substrate.

As shown, stainless steel substrate used in our experiments revealed micro-scale topography. As was mentioned earlier, the surface of the substrate is not atomically smooth.

In Figure 32 AFM 3D images of CHAp films containing 5 layers of Ca-P-O gel deposited by spin- and dip-coating techniques are presented.

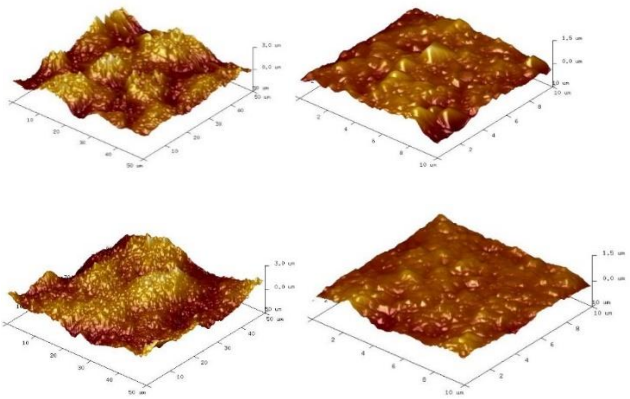

**Figure 32.** AFM images of different areas of the samples containing 5 layers of Ca-P-O gel deposited by spin-coating (at top) and dip-coating (at bottom) techniques.

Again, the AFM images of CHAp samples clearly differ from the substrate images. AFM topographs show a network of crystallites with intercrystalline

vacant spaces [156]. However, AFM images do not show differences in the topography between synthesized samples using different techniques. The surfaces are rough and contain similar bumps. The AFM images of the specimens containing 15 and 30 layers, however, are slightly different. The AFM 3D surface topology of the samples containing 15 layers of CHAp and obtained by different techniques are presented in Figure 33.

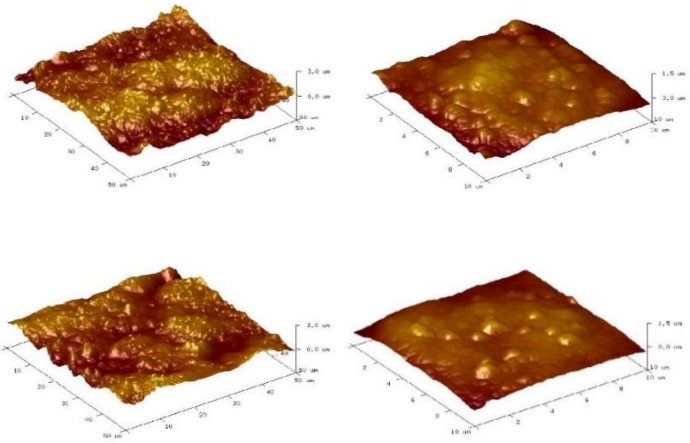

**Figure 33.** AFM images of different areas of samples containing 15 layers of C-P-O gel deposited by spin-coating (at top) and dip-coating (at bottom) techniques.

These AFM images exhibit a homogeneous coverage of the surface of substrate by CHAp coating [157]. Apparently, the coating increased and saturated the surface texture of the samples which is in a good agreement with SEM results. The surface of the CHAp films containing 30 layers is smooth with larger crystals and more homogeneous crystal size distribution (see Figure 34).

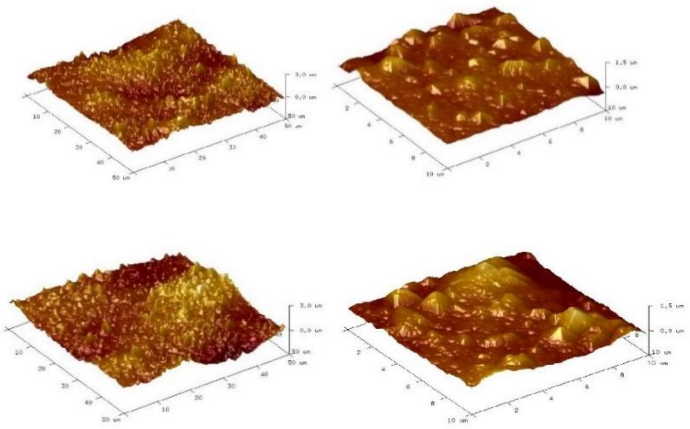

**Figure 34.** AFM images of different areas of samples containing 30 layers of C-P-O gel deposited by spin-coating (at top) and dip-coating (at bottom) techniques.

The AFM results of surface roughness measurements for sol-gel derived CHAp films on stainless steel substrates are presented in Table 9.

**Table 9.** The AFM results of surface roughness measurements for CHAp films obtained using different synthetic techniques.

| **Number of layers** | **RMS (Rq, nm)** | | | |
|---|---|---|---|---|
| | Surface area 10/10μm | | Surface area 50/50μm | |
| | Spin-coating | Dip-coating | Spin-coating | Dip-coating |
| 0 | 37.9 | | 40.2 | |
| 5 | 37.8 | 34.9 | 56.3 | 44.4 |
| 15 | 29.7 | 30.1 | 38.8 | 39.8 |
| 30 | 28.0 | 27.3 | 36.9 | 37.1 |

As seen from Table 9, the roughness of stainless steel substrate after five spinning and annealing procedures has changed negligibly. The roughness of CHAp films remains almost the same with increasing number of layers from 15 to 30 by both spin- and dip-coating techniques. The AFM results suggested that the surface roughness and morphology of the CHAp films changed remarkably in comparison with un-coated substrate. Moreover, the presence of smaller grains along the step-edges (see Figure 34) proves the presence of considerable grain mobility during the deposition process [158].

It is possible to conclude that the CHAp films with large number of layers could also be produced on stainless steel substrate using an aqueous sol-gel method by both dip- and spin-coating techniques. The phase purity and homogeneity of these CHAp samples was increased considerably. Moreover, the morphological properties of CHAp coatings could be controlled by selection of the preparation technique. However, the synthesis for the preparation of CHAp coatings with large number of layers is time consuming process.

## 3.3. SYNTHESIS AND CHARACTERIZATION OF CHAp THIN FILMS DEPOSITED ON ROUGHENED STAINLESS STEEL SURFACE VIA SPIN-COATING TECHNIQUE

### 3.3.1. Characterization of as-prepared CHAp coatings

#### 3.3.1.1. XRD analysis

As was mentioned in the experimental part, the surface of stainless steel substrate was additionally modified by formation of the transverse and longitudinal patterned roughness prior to the spin-coating of the Ca–P–O sol-gel solution. The aim of this procedure was to improve adhesion between coating and substrate. Phase composition of the obtained coatings was determined by XRD analysis. Figure 35 shows the XRD patterns of CHAp films synthesized using spin-coating technique on the steel surface with patterned roughness. The multilayer coatings were obtained by increasing the number of spinning procedures from 15 to 30. The dependence of CHAp formation on the times of spinning and annealing is evident. As seen, after 15 spinning and annealing procedures iron oxides ($Fe_2O_3$ and $Fe_3O_4$) are the dominant crystalline phases. This is not surprising, since the iron oxide phase is clearly formed by heating at the same temperature only rough stainless steel substrate (see Figure 36).

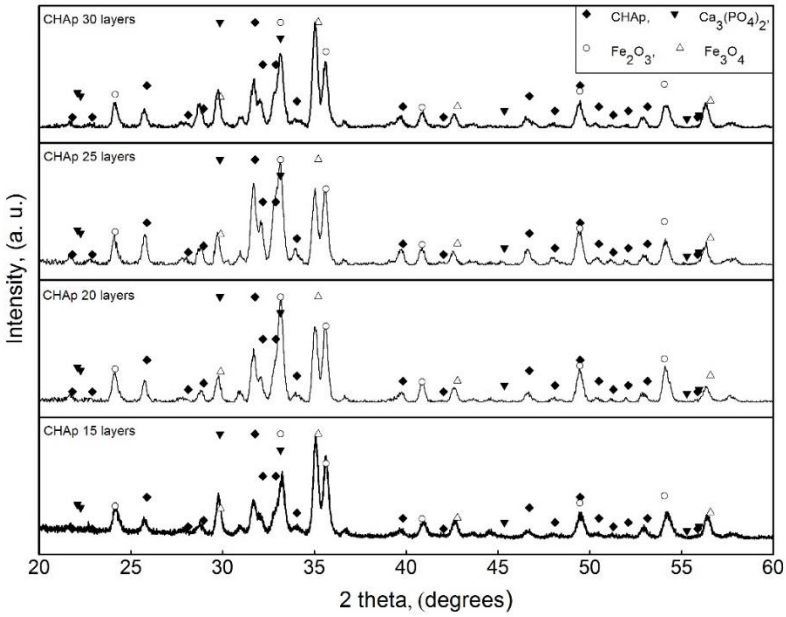


**Figure 35.** XRD patterns of calcium hydroxyapatite (CHAp) coatings fabricated using different numbers of spinning and annealing procedures. Diffraction peaks are marked: ♦ is CHAp, ▼ is $Ca_3PO_4$, ○ is $Fe_2O_3$, Δ is $Fe_3O_4$.

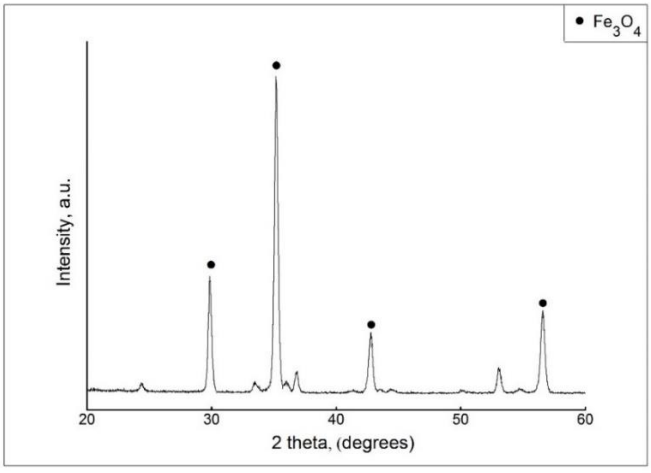


**Figure 36.** XRD pattern of uncoated rough 316 L stainless steel substrate annealed at 850 °C. $Fe_3O_4$ is the only dominant phase.

However, even after 15 coating cycles, the calcium phosphate phases such as CHAp and $Ca_3(PO_4)_2$ have also formed. The intensity of diffraction lines attributable to the CHAp phase monotonically increased with increasing the number of layers to 20 and 25. Well resolved CHAp diffraction peaks were seen and in the XRD pattern of the sample with 30 layers. However, after 30 spin-coating procedures the intensity of peaks attributable to calcium phosphate phases surprisingly decreased. These XRD results allow us to draw the initial conclusion that the most crystalline CHAp sample was obtained with 25 Ca-P-O layers.

### 3.3.1.2. FTIR analysis

The DRIFT spectra of sol-gel derived CHAp films with 15, 20, 25, 30 layers obtained with the DRIFTS attachment are presented in Figure 37.

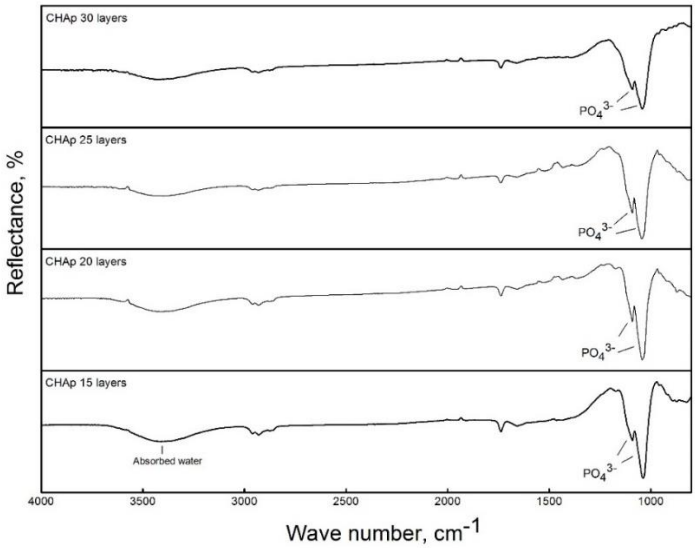


**Figure 37.** DRIFT spectra of sol-gel derived films with 15, 20, 25, 30 layers of Ca-P-O precursor gel.

The DRIFT spectra are almost identical among all the samples with various number of layers. The characteristic calcium hydroxyapatite absorption bands in the range of 1100–950 $cm^{-1}$ were clearly visible [142]. Strong bands located at 1035 and 1090 $cm^{-1}$ resulted from the $\nu_1$ symmetric P–O stretching vibrations in $PO_4^{3-}$ [142, 145]. The broad band visible in the range of 3600–

3300 $cm^{-1}$ is associated with O–H stretch vibrations and attributed to adsorbed water [159, 160]. In all spectra, weak and broad bands in the range of 1550–1370 $cm^{-1}$ were also seen. The origin of these bands is related to the stretching and bending modes of $CO_3^{2-}$ in CHAp (C–O bond), despite the last band being slightly shifted to the region of lower wavenumbers. The existence of low-intensity bands at about 870 $cm^{-1}$ may be ascribed to the $\nu_2$ bending mode of $CO_3^{2-}$ (C–O bond) in CHAp and confirmed the presence of carbonated apatite in the samples [160]. No specific bands attributable to oxyhydroxyapatite $Ca_{10}(PO_4)_6(OH)_{2-2x}O_x$ were detected in our spectra, however, such bands were present for the CHAp thin films deposited on Si substrate [161].

### 3.3.1.3. Raman analysis

Figure 38 shows Raman spectra in the 200–1400 $cm^{-1}$ spectral region of the CHAp samples deposited on rough stainless steel substrate.

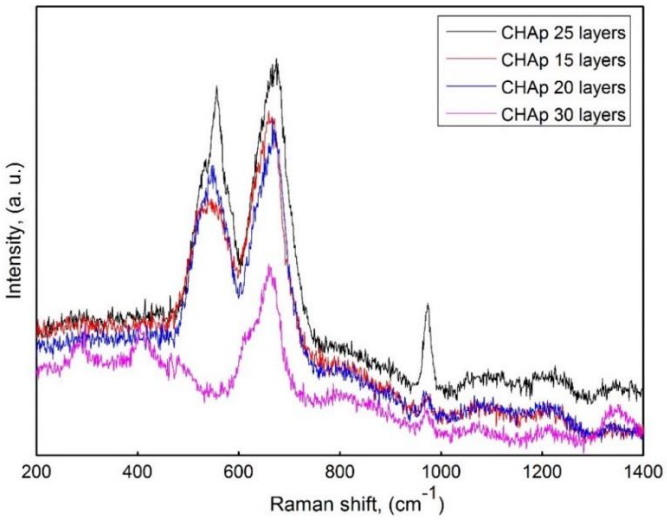


**Figure 38.** Raman spectra of the CHAp samples containing 15, 20, 25, and 30 layers of Ca–P–O gel deposited on rough stainless-steel substrate in 200–1400 $cm^{-1}$ spectral region.

The most intensive Raman bands were observed for the CHAp sample having 25 layers. The intensity of the bands monotonically increased with the number of layers but decreased for the specimen having 30 layers. The most intense bands were observed at 580 and 640 $cm^{-1}$. These bands could be

assigned to the triple degenerate ($F_2$ symmetry) asymmetric bending modes $\nu_4$ of phosphate group in calcium hydroxyapatite [162]. Interestingly, the band at 580 $cm^{-1}$ was not observed in Raman spectrum of the CHAp sample synthesized with 30 layers. The band at about 960 $cm^{-1}$ is due to $\nu_1$ ($A_1$) symmetric stretching vibration of the tetrahedral $PO_4^{3-}$ group. This band was the most intense in the Raman spectrum of the CHAp sample synthesized on a silicon nitride substrate [161]. For the specimens in this study, the intensity of this band was substantially less. The peak position of this band confirms the exact stoichiometry (molar ratio Ca:P = 1.67) for calcium hydroxyapatite [163, 164]. The Raman spectroscopy results are in good agreement with the XRD analysis data, because in both spectra the most intense peaks attributable to CHAp were visible for the sample with 25 layers.

#### 3.3.1.4. XPS analysis

The XPS of samples was measured by calibrating the binding energy scale with C 1*s* peak as reference. All XPS survey spectra (Figure 39a) exhibited signals characteristic of calcium, oxygen, phosphorous, and carbon. The high-resolution O 1*s* XPS convoluted spectra (Figure 39b) showed a signal centered at 535.1 eV corresponding to O–P–O and O–H bonding in hydroxyapatite [165]. Figure 39c shows P 2*p* XPS spectra, which consist of $2p^{3/2}$ and $2p^{1/2}$ components, corresponding to O–P–O bonding in the ($PO_4$) network of calcium hydroxyapatite and tricalcium phosphate [166]. The high resolution Ca 2*p* spectra are shown in Figure 39d. That spectra consists of two peaks at 351.1 and 354.7 eV. These peaks are attributed to the spin-orbit splitting components of $2p^{3/2}$ and $2p^{1/2}$ with energy difference of 3.4 eV [167]. The elemental analysis, represented as Ca to P ratio, showed that the Ca to P ratio was lower than in stoichiometric calcium hydroxyapatite (1.67). This is not surprising, since the samples also contain TCP. The Ca:P varied between 1.40 and 1.51. Only sample with 15 precursor gel layers had Ca:P ratio 1.51 which is common to TCP. Ca:P ratio was 1.4 in samples with 20, 25 and 30 layers. Lack of $OH^-$ groups in the sample with 15 layers results in peak shift toward lower binding energies.

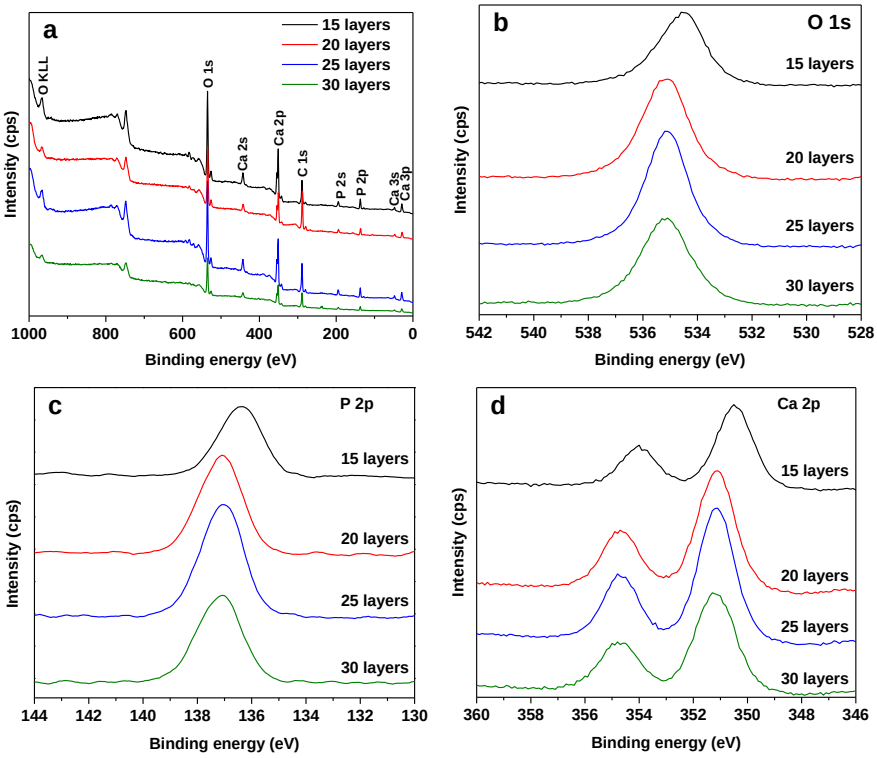


**Figure 39.** XPS survey spectra (**a**) and high-resolution O 1*s* (**b**), P 2*p* (**c**) and Ca 2*p* (**d**) XPS spectra taken from the surface of deposited and annealed CHAp films with different numbers of layers.

### 3.3.1.5. SEM analysis

The SEM micrographs of the surfaces of obtained CHAp samples are shown in Figure 40. As seen, the surface of the CHAp specimen obtained after 15 spin-coating procedures is uneven with clearly pronounced asperities and pores. The better surface smoothness was achieved when the number of layers was increased to 20. The CHAp coating on roughened stainless steel substrate obtained after 25 spin-coating procedures was even more uniform. The surface of CHAp coating with 25 layers was composed of homogeneously distributed well interconnected spherical grains about 250 nm in size. The formed layer of hydroxyapatite was continuous and pore-free. Surprisingly, the morphological features of the CHAp sample synthesized with 30 layers were slightly changed, and the formation of nanospheres on the surface cannot be seen anymore. But nano-sized pores were visible in the CHAp sample

containing 30 layers of precursor. Regularly shaped particles about 1-2 μm in size are TCP crystals. TCP phase presence was confirmed by XRD data.

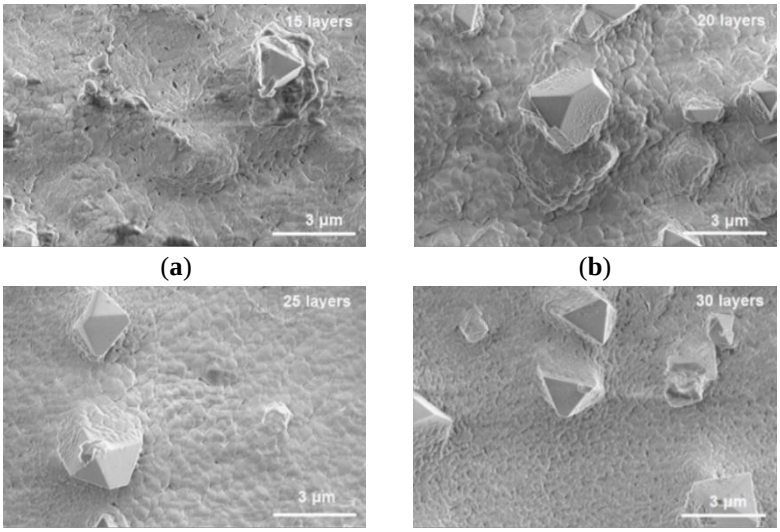


**Figure 40.** SEM micrographs of the CHAp samples containing (**a**) 15, (**b**) 20, (**c**) 25, and (**d**) 30 Ca-P-O precursor layers.

### 3.3.1.6. Tribological measurements

The results of the tribological measurements are presented in Figure 41. Coefficient of friction (COF) changes were observed after more loading cycles were performed for either a 1 or 5 N load. In most samples, the instantaneous COF values remained similar throughout the selected range of the reciprocal motion, i.e., the middle 80% of a segment. Tribological effectiveness (lowest COF) of sol-gel derived CHAp layers coated on the rough stainless steel substrates was evaluated under 1 and 5 N loads. The layer thickness of CHAp influenced friction from 15 to 30. Layers of 15 and 30 had the lowest friction by showing a gradual increase of COF after a few friction cycles under 1 N load. Samples with 30 coating cycles had the highest friction. This effect may be explained by rapid CHAp layer deformation and degradation, producing wear debris particles that damaged the substrate. The CHAp coating with 30 layers was thick enough to break off or delaminate into debris particles. Another possible mechanism to explain such an increase in friction could be related to changes in the surface morphology of these CHAp specimens. The best tribological effectiveness (lowest COF) was COF reduction below 0.2 for

100 friction cycles under 1 N load. Friction for the sample with 30 layers evaluated under 5 N load was even higher; the COF value was 0.6 after just a few friction cycles. The samples with 15 and 25 layers had much lower COF, below 0.2 for 30 friction cycles. Despite lower durability (30 vs. 100 friction cycles) the CHAp layers on the patterned surface resist abrasion under considerable loads. Thin layers, produced after 15 coating cycles, were tribologically effective under 5 N load, while under 1 N load this effect was not observed. Overall, CHAp layers showed the best protective and anti-frictional properties when produced after 25 coating cycles under 1 and 5 N loads. SEM micrographs showed that the steel substrate with 25 layers was evenly coated with homogeneously distributed spherical grains of about 250 nm in size.

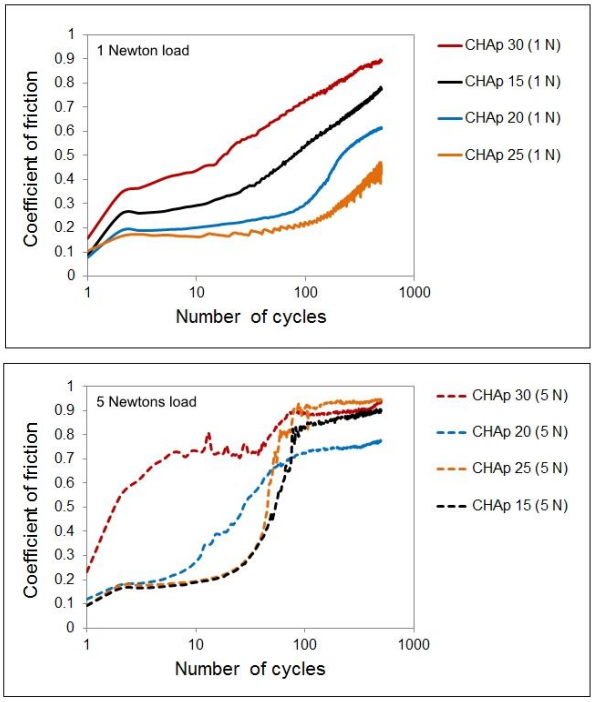


**Figure 41.** Friction dependence on the coating cycles of Ca-P-O gel layers deposited on the patterned rough surface of stainless steel substrate under 1 and 5 N loads. Number of layers: 15 layers – CHAp 15, 20 layers – CHAp 20, 25 layers – CHAp 25, and 30 layers – CHAp 30.

### 3.3.1.7. Contact angle measurement

The contact angle measured for the uncoated patterned stainless steel substrate was 81.3°, as shown in Figure 42. The contact angle values of all CHAp coatings fell within a small range (113°–116°). The images of water drops on CHAp surfaces coated with 15, 20, 25, or 30 sol-gel layers show the CHAp coatings were slightly hydrophobic. These results, however, were unexpected initially since they differ significantly from the previous ones. The determined contact angle of water drop on the surface of stainless steel without additional surface modification by formation of the transverse and longitudinal patterned roughness was equal 107.3°. The coatings synthesized on traditional substrates with different number of layers and obtained using both spin-coating and dip-coating techniques were hydrophilic. It was also demonstrated that the wettability of CHAp coatings depended on number of layers. The contact angle of CHAp coatings varied between 69.0° and 78.8° depending on the number of layers and used fabrication technique.

Contact angle differences between smooth and roughened stainless steels could be explained by the physical aspect. Surface wettability of mechanically roughened 316 L stainless steel is about 79° [168] which is close to our experimental result – 81.3°. The reason our experimental contact angle of smooth stainless steel is so high could be due to presence of the cracks on the surface (Figure 18). When cracks are deep enough, water droplet can not fully contact with the surface thus surface appears hydrophobic despite the fact it is hydrophylic by nature. This phenomenon is explained by Cassie – Baxter theory [169]. Next, the formation of significant amount of tricalcium phosphate phase $Ca_3(PO_4)_2$ on the patterned stainless steel substrate was clearly observed. The TCP phase does not contain $OH^-$ groups which are very hydrophylic. Thus, synergy of physical and chemical effects, possibly, is responsible for the observed hydrophobicity of synthesized calcium phosphatic layers on modified surface of stainless steel. Such type of biphasic hydrophobic phosphate bioceramic could be used for improving corrosion resistance of implants and, consequently, to increase its antibacterial properties. However, the osteointegration of obtained coatings could be insuficient therefore more suitable for replacement of non-load bearing parts.

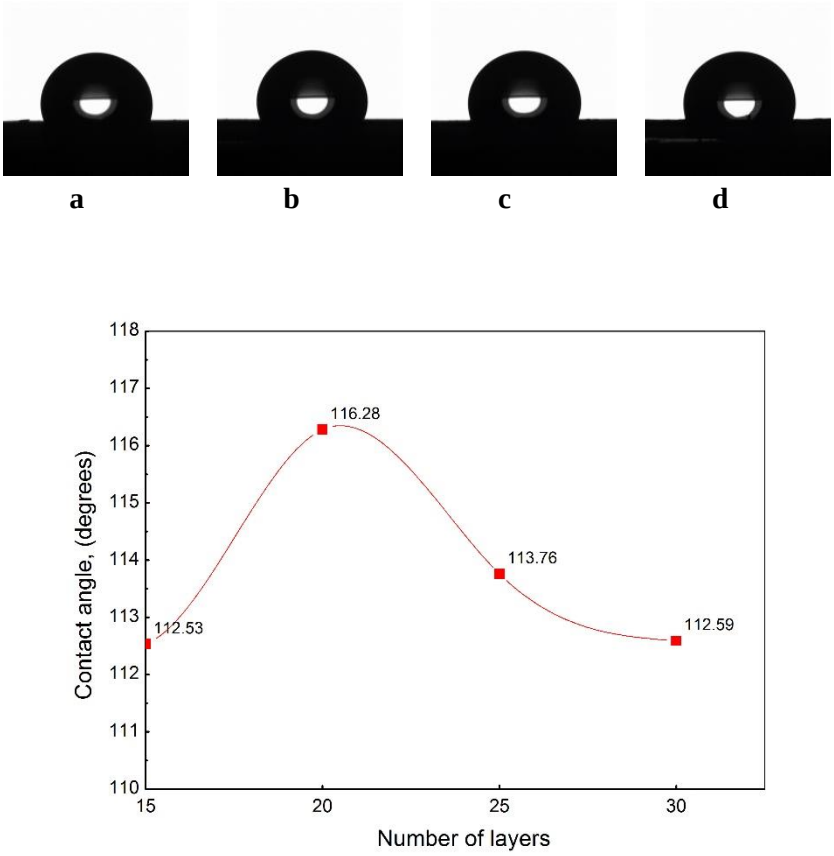


**Figure 42.** Variation of contact angle of CHAp coatings with increasing number of precursor gel layers (bottom) and the images of water drops on CHAp surfaces coated with (**a**) 15, (**b**) 20, (**c**) 25, and (**d**) 30 sol-gel layers.

### 3.3.2. Characterization of coatings after immersion into simulated body fluid (SBF)

#### 3.3.2.1. XRD analysis

All CHAp samples synthesized on the surface of stainless steel with additional surface modification by formation of the transverse and longitudinal patterned roughness were immersed into simulated body fluid (SBF) for one month. The phase transformations and morphological changes of the samples were examined after 2, 3, and 4 weeks. The SBF was prepared

using the method proposed by Kokuba and Takadama [170]. The concentrations of ions in the prepared SBF solution are presented in Table 10.

**Table 10.** Nominal ion concentrations of simulated body fluid (SBF) in comparison with those in human blood plasma.

| Ion | Ion Concentration (mM) | |
|---|---|---|
| | **Blood Plasma** | **SBF** |
| $Na^+$ | 142.0 | 142.0 |
| $K^+$ | 5.0 | 5.0 |
| $Mg^{2+}$ | 1.5 | 1.5 |
| $Ca^{2+}$ | 2.5 | 2.5 |
| $Cl^-$ | 103.0 | 147.8 |
| $HCO_3^-$ | 27.0 | 4.2 |
| $HPO_4^{2-}$ | 1.0 | 1.0 |
| $SO_4^{2-}$ | 0.5 | 0.5 |
| pH | 7.2–7.4 | 7.40 |

The XRD patterns of the CHAp samples with 15, 20, 25 and 30 precursor layers after immersion into SBF for 2, 3 and 4 weeks are presented in Figures 43-46. Once placed into SBF, the TCP started to dissolve and induce formation of amorphous calcium phosphate (ACP) and precipitation of CHAp. However, the amount of precipitated ACP and CHAp is probably too small to be detected using the XRD [171]. ACP is the precursor phase of bone-like hydroxyapatite [172]. Loss of crystallinity due to lower peak intensity is visible in Figures 43 and 44 for the samples with 15 and 20 layers respectively. The changes in phase composition during one month of soaking in SBF were not monotonic.

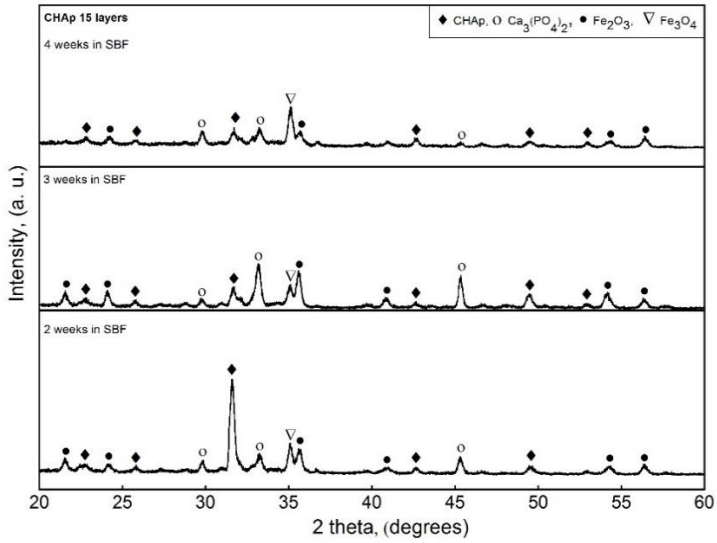


**Figure 43.** XRD patterns of CHAp samples coated with 15 layers after immersion in SBF for 2, 3, and 4 weeks. Diffraction peaks are marked: ♦ is CHAp, ○ is $Ca_3PO_4$.

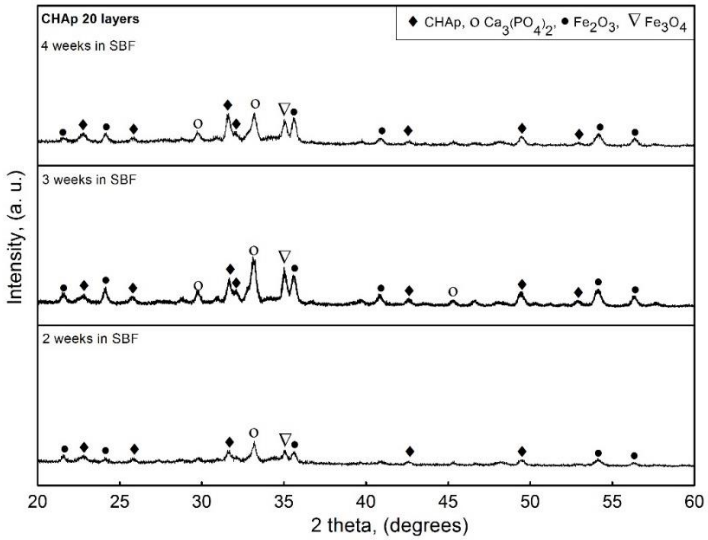


**Figure 44.** XRD patterns of CHAp samples coated with 20 layers after immersion in SBF for 2, 3, and 4 weeks. Diffraction peaks are marked: ♦ is CHAp, ○ is $Ca_3PO_4$.

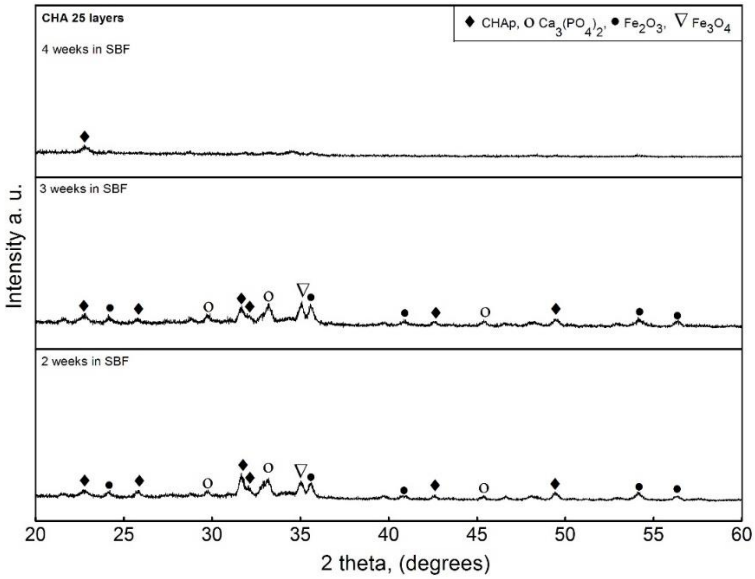


**Figure 45.** XRD patterns of CHAp samples coated with 25 layers after immersion in SBF for 2, 3, and 4 weeks. Diffraction peaks are marked: ♦ is CHAp, ○ is $Ca_3PO_4$.

The situation has changed for the CHAp sample obtained with 25 layers (Figure 45). After 1 month of soaking in SBF, a decrease in the intensity of the peaks attributable to both CHAp and TCP phases can be seen in the XRD patterns. Amorphous precipitate of CHAp and ACP dominated the surface of stainless steel. However, the presence of amorphous calcium phosphate has a very positive impact for bone repair [173]. With further increases in the number of CHAp layers, the dissolution and precipitation process remains very similar (Figure 46).

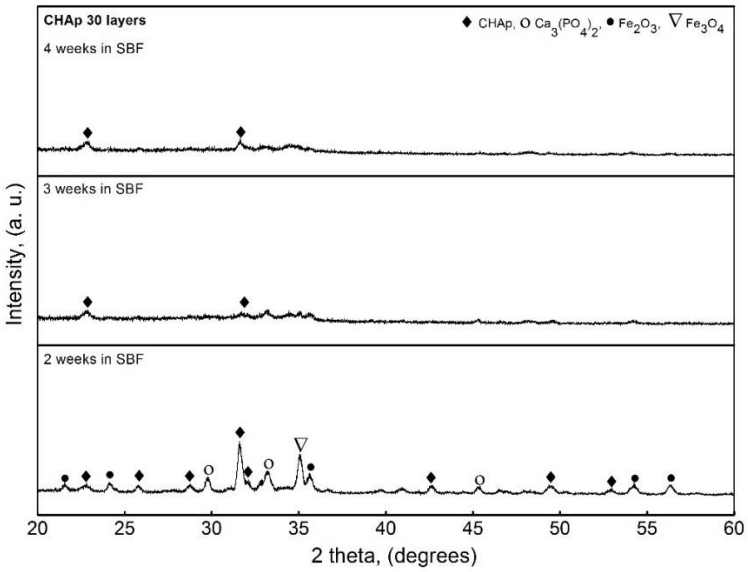


**Figure 46.** XRD patterns of CHAp samples coated with 30 layers after immersion in SBF for 2, 3, and 4 weeks. Diffraction peaks are marked: ♦ is CHAp, ○ is $Ca_3PO_4$.

### 3.3.2.2. SEM analysis

The SEM micrographs of the CHAp samples with 15, 20, 25, and 30 layers obtained after immersion into SBF for 2, 3, and 4 weeks are presented in Figure 47. Interestingly, almost no changes in the surface morphology of CHAp coatings were observed after soaking in SBF. The microstructure was not influenced by immersion time or by the number of layers on the substrate, despite the slight changes in phase composition and crystallinity during SBF immersion were determined. Neither etching behavior, nor additional precipitates were observed. Probably, the dissolution and the precipitation processes proceeded simultaneously, without any domination [174]. However, the SEM images obtained using secondary electron or backscattered electron modes gave poorly distinguishable results among different calcium phosphate phases [175-178]. Loss of crystallinity and formation of various defects including twining, dislocations, stacking faults, and grain boundaries should be investigated using transmission electron microscopy [179].

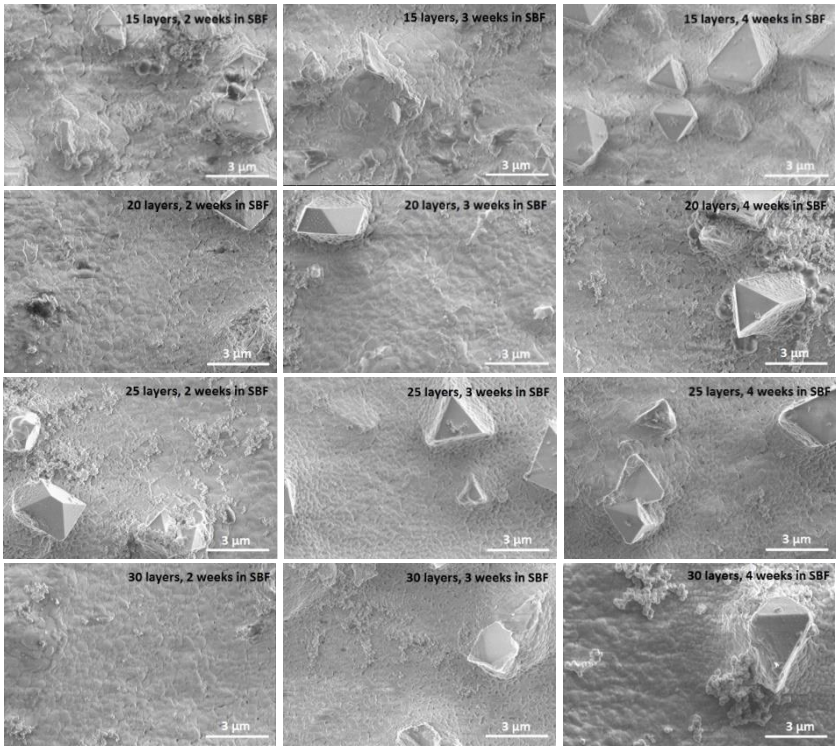


**Figure 47.** SEM micrographs of CHAp samples coated with 15, 20, 25, and 30 layers after immersion in SBF for 2, 3, and 4 weeks.

### 3.3.2.3. Contact angle measurements

The SEM results were partially confirmed by the contact angle measurements. All CHAp coatings after soaking in SBF were much more hydrophilic compared to the initial samples. The values of the contact angle determined for all studied specimens after 3 weeks of soaking in SBF (Figure 48) were about 40° – 60°. Only negligible changes of contact angle were observed with increasing soaking time to 4 weeks.

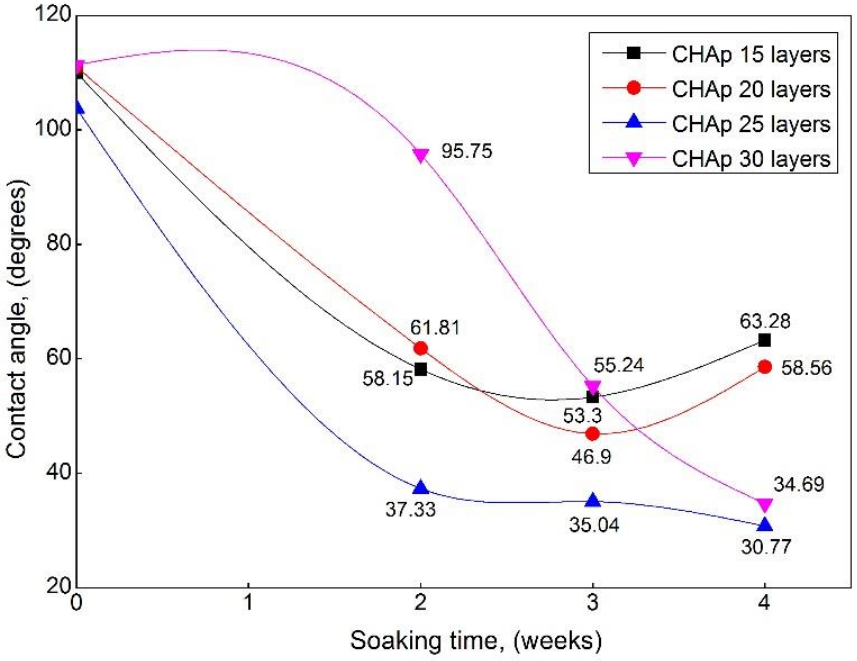


**Figure 48.** Contact angle values for CHAp samples with 15, 20, 25 and 30 layers of Ca-P-O precursor gel layers after soaking in SBF.

## 3.4. SYNTHESIS AND CHARACTERISATION OF CHAp THIN FILMS ON STAINLESS STEEL SUBSTRATE MODIFIED WITH TiN SUBLAYER

### 3.4.1. XRD analysis

Figure 49 shows the XRD patterns of CHAp films synthesized using spin-coating technique on the 316 L stainless steel surface modified with titanium nitride (TiN) sublayer. The phase composition of the coatings was determined depending on the times of spinning and annealing procedures.

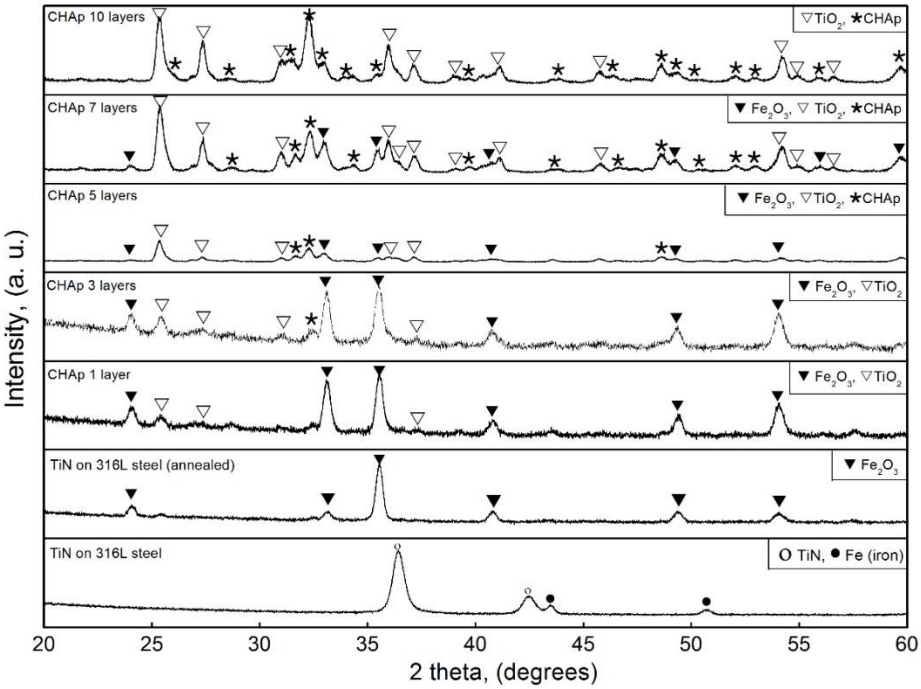


**Figure 49.** XRD patterns of CHAp films with various number of Ca-P-O gel layers synthetized on the 316 L stainless steel surface modified with TiN sublayer coating. The reflections of crystalline phase are marked: ● Fe, ○ TiN, ▼ $Fe_2O_3$, ▽ $TiO_2$, ✶ CHAp.

By heating the stainless steel substrate coated with TiN sublayer at 850 °C in air the iron was oxidized to the mixture of iron oxides. This is evident from the XRD pattern of annealed Fe/TiN substrate. Moreover, the reflections attributable to the TiN phase could not be detected after a heat treatment of substrate. The XRD pattern of the sample obtained after one spinning procedure already contains the reflections of oxides of iron and titanium. It means, that the sol-gel processing promotes an oxidation of TiN. In the XRD pattern of sample synthesized using three spinning and annealing steps, the negligible reflection attributable to the CHAp phase already is seen. With further increasing the spinning and annealing times the monotonic increase of intensities of reflections of CHAp crystalline phase is evidently seen in the XRD patterns of CHAp films fabricated on Fe/TiN substrate. Besides, the formation of CHAp evidently inhibits formation of $Fe_2O_3$ and promotes

formation of $TiO_2$. Interestingly, after ten coating procedures the reflections attributable to the iron oxides are no longer visible in the XRD patterns and are fully replaced by diffraction peaks of titanium oxide. Thus, the TiN sublayer acts as the buffer layer inhibiting possible formation of iron oxides during the sol-gel synthesis of calcium hydroxyapatite on the surface of stainless steel.

### 3.4.2. Raman analysis

Figure 50 shows Raman spectra of studied samples containing different layers of composition for synthesis of CHAp prepared by spin-coating technique and subsequently annealed at 850 ºC and TiN/steel substrate before the formation of calcium hydroxyapatite coating. The dominant band of TiN/steel substrate at 671 cm−1 (Fig. 50d) evidence presence of magnetite (Fe3O4) [180-183]. The broad low intensity band near 1346 cm−1 and narrow low intensity feature at 298 cm−1 belongs to haematite (α-Fe2O3) [181-183]. Formation of calcium hydroxyapatite after annealing of spin-coated precursors on all of the studied samples (Fig. 50a, b, c) is visible from the narrow and well-defined band at 961−962 cm−1 [163, 184-186]. This band belongs to symmetric stretching vibration ν1 (A1) of tetrahedral phosphate group [187]. Peak position of this band is characteristic marker for presence of stoichiometric calcium hydroxyapatite with molar Ca/P ratio of 1.667 [163, 184, 188]. Two intense bands visible near 614−615 and 448−450 cm−1 belong to TiO2 rutile phase A1g and Eg modes, respectively [162, 189]. Presence of these bands clearly reveals conversion of TiN layer into the TiO2 rutile structure during the preparation of calcium hydroxyapatite. The broad features near 670−780 cm−1 and 338−348 cm−1 might be associated with presence of maghemite (γ-Fe2O3) [180-183].

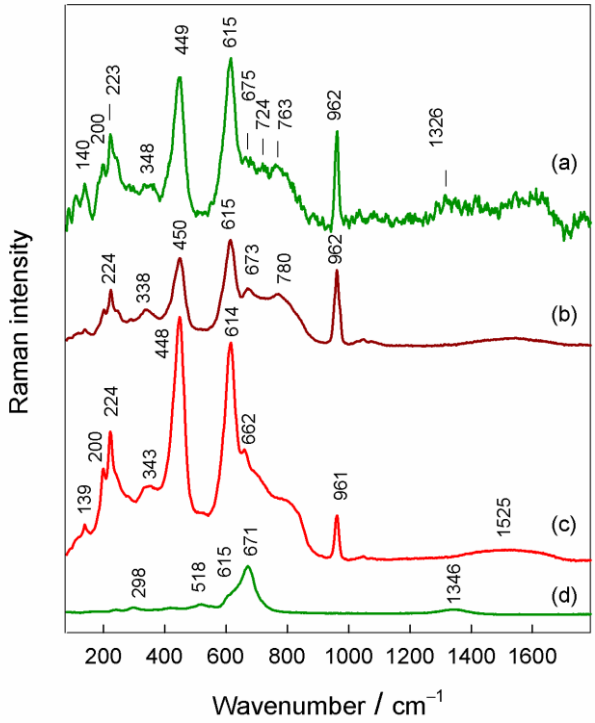


**Figure 50.** Raman spectra of samples containing (a) 10 layers, (b) 7 layers, and (c) 5 layers of composition for synthesis of calcium hydroxyapatite deposited by spin-coating technique and annealed at 850 oc, and (d) initial TiN/steel substrate before the deposition of calcium hydroxyapatite forming layer.

### 3.4.3. Microscopical characterization

The SEM micrographs of 316 L steel substrate with TiN sublayer before and after annealing at 850 °C are presented in Figure 51.

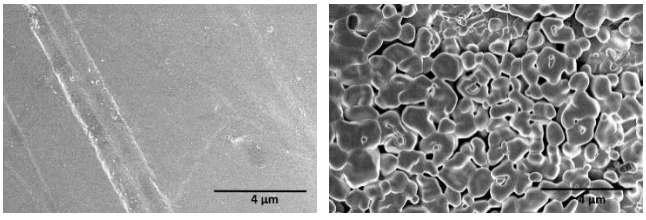


**Figure 51.** SEM micrographs of 316 L steel substrate with TiN sublayer before (left) and after annealing at 850 °C (right).

As we can see, the surface of the substrate before heat treatment is smooth, flat, crack and pores free. A situation is totally different after annealing the 316 L steel substrate at 850 °C. The surface during the heat-treatment was homogenously coated by differently shaped microparticles of iron oxide ($Fe_2O_3$). The particles are non-uniform, partially merged with average grain size of 1-2 μm. Also, the porous microstructure of the 316 L steel substrate after annealing at 850 °C could be determined from the SEM micrograph.

After application of the first CHAp layer (see Figure 52a), the microparticles of iron oxide are not merged anymore, the pores appear less pronounced, and they are filled with titania particles. Obviously, the latter situation was slightly further developed after the spinning of three layers of CHAp (Figure 52b). Significant changes in surface microstructure are visible after repeating the synthesis of CHAp for five times (Figure 52c). The dense surface having small irregular pores (about 200 nm) has formed. Moreover, the surface is covered with plate-like crystallites which size is about 1-2 μm. Even more compact coating was obtained after seven sol-gel layers (Figure 52d). The transformation of plate like particles to spherical nanoparticles also takes place in this stage of sol-gel processing. This is related to the transformations of crystalline phases which is visible in the XRD patterns of these specimens. In the SEM image of CHAp sample obtained with ten layers (Figure 52e) the formation of uniform surface with exposed irregular crystallites is observed. Thus, with increasing the spinning and annealing times from seven to ten the previously observed nanoparticles showed a tendency to growth to the bigger derivatives.

AFM images of 316 L steel substrate with TiN sublayer before and after annealing at 850 °C are presented in Figure 53. As seen, the AFM results correlate well with SEM data and show an increased roughness of the surface of the annealed sample.

AFM images of CHAp coated samples are shown in Figure 54. The AFM results of surface roughness measurements for CHAp films on stainless steel with TiN sublayer substrates for different areas are summarized in Table 11. As we can see, the roughness of the CHAp coatings decreases almost monotonically with increasing the amount of CHAp layers. Only almost no changes in the rougness was observed for the CHAp coatings fabricated after three and five spinning and annealing times. This stage was only one exception in all series of compounds. The AFM results are in a good correlation with ones obtained by SEM measurements.

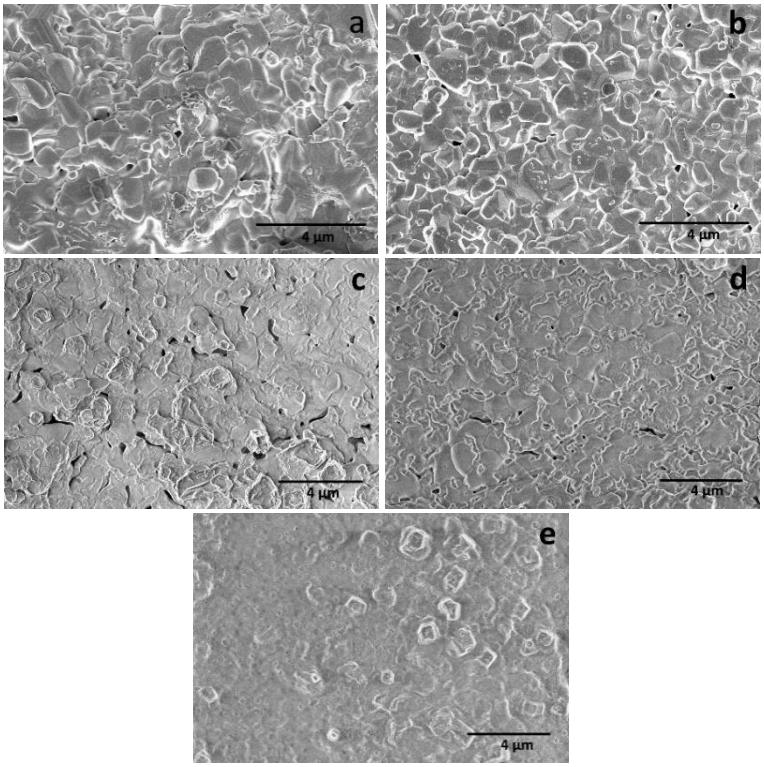


**Figure 52.** SEM micrographs of the sol-gel derived CHAp coatings on the 316 L steel substrate with TiN sublayer obtained after 1 (a), 3 (b), 5 (c), 7 (d) and 10 (e) the spinning and annealing procedures.

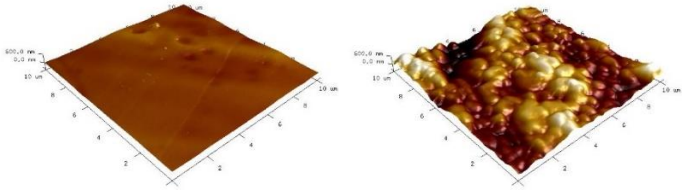

**Figure 53.** AFM images of 316 L steel substrate with TiN sublayer before (left) and after annealing at 850 °C (right).

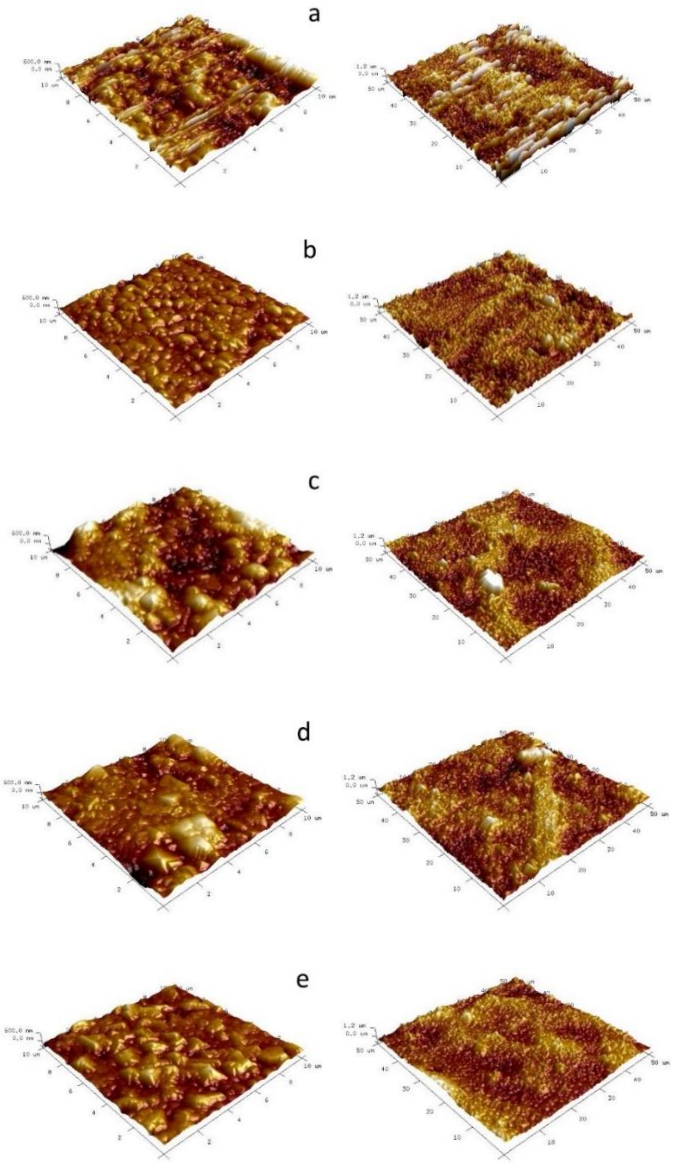


**Figure 54.** AFM images of different areas of CHAp samples obtained on the steel substrate with TiN sublayer using 1 (a), 3 (b), 5 (c), 7 (d) and 10 (e) spinning and annealing procedures.

**Table 11.** The AFM results of surface roughness measurements for CHAp films on stainless steel with TiN sublayer obtained after annealing at 850 °C.

| **Number of layers** | **RMS (Rq, nm)*** | |
|---|---|---|
| | Surface area 10/10 μm | Surface area 50/50 μm |
| 0 | 321 | 410 |
| 1 | 233 | 447 |
| 3 | 195 | 362 |
| 5 | 196 | 359 |
| 7 | 147 | 318 |
| 10 | 117 | 260 |

*Rq values for raw substrate is 37.4 nm (surface area 10/10 μm) and 81.9 (surface area 50/50 μm).

## 4. CONCLUSIONS

1. An aqueous sol-gel method was developed for the synthesis of calcium hydroxyapatite ($Ca_{10}(PO_4)_6OH_2$, CHAp) thin films on stainless steel substrate at 1000 ºC temperature with low number of layers. For the fabrication of coatings, two different dip-coating and spin-coating techniques were applied and compared. The XRD and FTIR results revealed that dip-coating technique was more favourable for the faster fabrication of CHAp on the surface of stainless steel.

2. The "necked" to each other particles of CHAp forming bigger agglomerates (1-2.5 μm) were formed in the sample obtained by dip-coating technique. However, less than 500 nm plate-like crystallites have formed during spin-coating fabrication of thin films. The values of contact angle on the surface of films decreased dramatically in comparison with pure substrate. Thus, the high hydrophilicity CHAp coatings were obtained after five immersing, withdrawal and annealing procedures in the sol-gel processing.

3. The CHAp coatings on stainless steel substrate with considerably increased phase purity and the homogeneity have been synthesized with increasing number of immersing, withdrawal and annealing procedures. The final synthesis temperature of CHAp samples fabricated using two different deposition dip-coating and spin-coating techniques was reduced to 850 ºC. The intensity of diffraction lines attributable to the $Ca_{10}(PO_4)_6OH_2$ phase in the XRD patterns increased with increasing number of spinning or dipping and annealing procedures confirming that both spin-coating and dip-coating techniques are suitable for the fabrication of CHAp on the surface of stainless steel with large number of layers.

4. The SEM results indicated different surface morphology of spin-coated and dip-coated samples when large number of layers of CHAp was designed. The spin-coated samples were homogeneous and composed of nano-scaled particles. The individual particles were about 100-300 nm in size. The dip-coated samples were not fully dense and remained porous with coral microstructure. Thus, the morphological properties of CHAp coatings could be controlled by selection of the preparation technique. The hydrophilic CHAp coatings with contact angle values of $69.0^{o}$-$78.8^{o}$ were

obtained after 30 immersing, withdrawal and annealing procedures in the sol-gel processing.

5. To increase the surface quality of CHAp coatings the specific modification of the surface of stainless steel substrate before the coating procedures was performed. An aqueous sol-gel method was applied for the synthesis of CHAp thin films on medical grade stainless steel substrates with transverse and longitudinal patterned roughness. The results obtained by XRD, DRIFT, Raman, XPS and tribological measurements were in a good correlation and confirmed that the best quality CHAp coatings were obtained after 25 spin-coating and annealing at 850 °C in air procedures.

6. The surface of CHAp coatings on roughened stainless steel substrate obtained after 25 spin-coating procedures was composed of homogeneously distributed well interconnected spherical grains about 250 nm in size. The formed layer of calcium hydroxyapatite was continuous and pore-free. The increased hydrophobicity of CHAp coatings on rough substrate, however, was determined. The increased hydrophobicity of CHAp coatings on rough substrate was achieved due to the synergy of energetic and chemical effects. Such type of biphasic hydrophobic phosphate bioceramics could be used for improving corrosion resistance of implants with increased antibacterial properties.

7. Fabricated CHAp coatings were evaluated after immersing in simulated body fluid (SBF) for 2, 3 and 4 weeks. After 1 month of soaking in SBF, a decrease in the intensity of the peaks attributable to both CHAp and TCP phases was observed. The XRD results clearly indicated that amorphous calcium phosphate had formed on the immersed samples. The microstructure of SBF treated CHAp samples was not influenced neither by immersing time nor by the amount of layers on the substrate despite the phase composition and crystallinity was different.

8. An aqueous sol-gel method was applied for the synthesis of CHAp thin films on medical grade stainless steel substrates with TiN sublayer. Each layer in the preparation of CHAp multilayers (1, 3, 5, 7 and 10) was separately annealed at 850 °C in air. It was determined that the sample obtained after one spinning procedure contained only the oxides of iron and titanium. The XRD analysis revealed that CHAp phase is visible after 5 spin-coating and annealing procedures. With further increasing the

number of spinning and annealing procedures the monotonic increase of intensities of reflections of CHAp crystalline phase was observed in the XRD patterns of CHAp films fabricated on Fe/TiN substrate.

9. It was demonstrated for the first time that the formation of CHAp inhibited the formation of $Fe_2O_3$ and promoted formation of $TiO_2$ on the surface. Interestingly, after ten coating procedures the reflections attributable to the iron oxides were no longer visible in the XRD patterns and were fully replaced by diffraction peaks of titanium oxide. Thus, the TiN sublayer acted as the buffer layer inhibiting possible formation of iron oxides during the sol-gel synthesis of calcium hydroxyapatite on the surface of stainless steel. Raman results were in good agreement with XRD data and confirmed conversion of TiN layer into the $TiO_2$ during the preparation of calcium hydroxyapatite coatings.

10. The SEM micrographs of CHAp samples obtained with ten layers revealed the formation of uniform surface with exposed irregular crystallites. With increasing the number of spinning and annealing procedures the previously observed nanoparticles showed a tendency to form bigger derivatives. The AFM results for different areas showed that the roughness of the CHAp coatings on stainless steel with TiN sublayer substrates decreased almost monotonically with increasing the amount of CHAp layers.

# 5. LIST OF PUBLICATIONS AND CONFERENCES PARTICIPATION

## 5.1. PUBLICATIONS INCLUDED IN THE THESIS

### 5.1.1. Articles

1. V. Jonauske, S. Stanionyte, S.-W. Chen, A. Zarkov, R. Juskenas, A. Selskis, T. Matijosius, Thomas C. K. Yang, K. Ishikawa, R. Ramanauskas and A. Kareiva. Fabrication of sol-gel derived calcium hydroxyapatite coatings on patterned rough surface, characterization and assessment of its behaviour in simulated body fluid. *Coatings*, 9, 334 (2019) 1-14.

2. V. Jonauske, A. Prichodko, R. Skaudzius and A. Kareiva. Sol-gel derived calcium hydroxyapatite thin films on 316L stainless steel substrate: comparison of spin-coating and dip-coating techniques. *Chemija,* 27 (2016) 192-201.

3. A. Prichodko, V. Jonauske, M. Cepenko, A. Beganskiene and A. Kareiva. Sol-gel derived two-dimensional nanostructures of calcium phosphates. *Adv. Sci. Technol.,* 91 (2014) 13-18.

### 5.1.2. Attended conferences

1. V. Jonauske, Y. Tanaka, Y. Nishimoto and A. Kareiva. Characterization of sol-gel dirived and spin-coated on stainless stell calcium hydroxyapatite thin films. *Materials science and engineering: European congress and exhibition on advanced materials and processes, September 26-28, Darmstadt, Germany, 2018, P06-59.*

2. V. Jonauskė, Thomas C.K. Yang and A. Kareiva. The formation of calcium hydroxyapatite thin films on stainless steel substrate. *The International Conference „EcoBalt 2018“, October 25-27, Vilnius, Lithuania, 2018,* 60.

3. V. Jonauskė, A. Prichodko, A. Kareiva and M. Malakauskaitė-Petrulevičienė. Spin-coated calcium hydroxyapatite thin films prepared using an aqueous sol-gel chemistry approach. *Fourth International Conference on Multifunctional, Hybrid and Nanomaterials (Hybrid Materials 2015), Sitges, Spain, 9-13 March, 2015, P1. 285.*

4. A. Prichodko, V. Jonauske and A. Kareiva. Characterization of sol-gel derived CHAp thin films on stainless steel substrate prepared using dip-coating procedure. *4th International Conference on Multifunctional, Hybrid and Nanomaterials (Hybrid Materials 2015) Sitges, Spain, March 9-13, 2015, P1.301.*

5. V. Jonauskė, A. Prichodko, Ž. Stankevičiūtė, R. Raudonis, A. Beganskienė and A. Kareiva. Sol-gel derived thin films of calcium hydroxyapatite: Comparison of two coating techniques. *Chemistry and Chemical Technology 2015: International Conference of Lithuanian Chemical Society, Dedicated to Professor Vitas Daukšas on His 80th Birth Anniversary, January 23, 2015, Vilnius, Lithuania, 92-93.*

6. A. Prichodko, V. Jonauske, A. Beganskiene and A. Kareiva. Comparison of sol-gel derived thin films of calcium hydroxyapatite: dip-coating and spin-coating procedures. *8th Scandinavian Society for Biomaterials Conference "Design of Biomaterials". Sigulda, Latvia, May 6-8, 2015, 79.*

7. A. Prichodko, V. Jonauske, M. Cepenko, A. Beganskiene and A. Kareiva. Sol-gel derived two-dimensional nanostructures of calcium phosphate composites. *13th International Ceramics Congress "CIMTEC 2014". Montecatini Terme, Italy, June 8-13, 2014, CE:P04.*

## 5.2. PUBLICATIONS NOT INCLUDED IN THE THESIS

### 5.2.1. Articles

1. V. Čiuvašovaitė, E. Adomavičiūtė and V. Vičkačkaitė. Solid-phase microextraction of parabens by polyaniline-polypyrrole coating. Chemija, 18 (2007) 11-15.

2. V. Vičkačkaitė and V. Čiuvašovaitė. Polyaniline-polypyrrole coating for solid phase microextraction. Centr. Eur. J. Chem., 5 (2007) 727-738.

### 5.2.2. Attended conferences

1. M. Malakauskaite, V. Jonauskė, Ž. Stankevičiūtė, R. Raudonis, A. Beganskienė, A. Kareiva and A. Prichodko. Spin-coated and dip-coated hydroxyapatite thin films on silica substrate: preparation and

characterization. *Int. Conf. "Bio-inspired materials". Potsdam, Germany, March 18-21, (2014) 111.*

ACKNOWLEDGEMENT

I am deeply grateful to my supervisors Prof. Dr. Aivaras Kareiva and Prof. Dr. Jurgis Barkauskas for their guidance, encouragement and being amazing mentors. I will always be grateful for their understanding, trust and support.

I am really grateful to all my colleagues from Sol-Gel Chemistry group and the Department of Inorganic Chemistry for scientific discussions and fun during spare time. I am especially grateful to Dr. Živilė Stankevičiūtė, Dr. Milda Malakauskaitė–Petrulevičienė, Dr. Jurgis Pilipavičius, Dr. Ramūnas Skaudžius, Dr. Martynas Misevičius, Dr. Inga Grigoravičiūtė–Puronienė, Dr. Lina Mikoliūnaitė and Dr. Monika Skruodienė for giving me their helping hand.

I am saying big thanks to the ladies from Administration of the Faculty of Chemistry and Geosciences I had a pleasure to work with and who were the best colleagues ever.

I would like to acknowledge Faculty of Chemistry and Geosciences for the financial support and opportunities to attend conferences and work with foreign colleagues in Taiwan at National Taipei University of Technology.

I am grateful to my amazing husband Mantas for his love, encouragement and care. Without you I wouldn‘t be where I am today. Huge thanks to my family and friends who surrounded me with love and supported emotionally during the final steps of my doctoral studies. Without support from all these amazing people my studies would have been much harder.

I dedicate this work to my daughters Ula and Vainė who are my inspiration and pride.

REFERENCES


1. Nutt, J.L. and M.C. Solan, *Ageing and orthopaedics.* Orthopaedics and Trauma, 2017. **31**(5): p. 321-325.
2. Stadhouders, N., et al., *Effective healthcare cost-containment policies: A systematic review.* Health Policy, 2019. **123**(1): p. 71-79.
3. Ayoub, M., et al., *Perception Versus Reality in the Cost of Orthopedic Trauma Implants.* Journal of Surgical Education, 2018. **75**(5): p. 1333-1341.
4. Stadhouders, N., et al., *Policy options to contain healthcare costs: a review and classification.* Health Policy, 2016. **120**(5): p. 486-494.
5. Ferguson, R.J., et al., *Hip replacement.* The Lancet, 2018. **392**(10158): p. 1662-1671.
6. Talha, M., et al., *Role of protein adsorption in the bio corrosion of metallic implants – A review.* Colloids and Surfaces B: Biointerfaces, 2019. **176**: p. 494-506.
7. Negrea, R., et al., *Akermanite-based coatings grown by pulsed laser deposition for metallic implants employed in orthopaedics.* Surface and Coatings Technology, 2019. **357**: p. 1015-1026.
8. Manam, N.S., et al., *Study of corrosion in biocompatible metals for implants: A review.* Journal of Alloys and Compounds, 2017. **701**: p. 698-715.
9. Najeeb, S., et al., *21 - Dental implants materials and surface treatments*, in *Advanced Dental Biomaterials*, Z. Khurshid, et al., Editors. 2019, Woodhead Publishing. p. 581-598.
10. Khandelwal, H., et al., *Characterization of hydroxyapatite coating by pulse laser deposition technique on stainless steel 316 L by varying laser energy.* Applied Surface Science, 2013. **265**: p. 30-35.
11. Thanh, D.T.M., et al., *Controlling the electrodeposition, morphology and structure of hydroxyapatite coating on 316L stainless steel.* Materials Science and Engineering: C, 2013. **33**(4): p. 2037-2045.
12. Gurappa, I., *Development of appropriate thickness ceramic coatings on 316 L stainless steel for biomedical applications.* Surface and Coatings Technology, 2002. **161**(1): p. 70-78.
13. Takechi, M., et al., *Tissue responses to anti-washout apatite cement using chitosan when implanted in the rat tibia.* Journal of Materials Science-Materials in Medicine, 2001. **12**(7): p. 597-602.
14. Shah, F.A., P. Thomsen, and A. Palmquist, *Osseointegration and current interpretations of the bone-implant interface.* Acta Biomaterialia, 2019. **84**: p. 1-15.
15. Sadtler, K., et al., *Divergent immune responses to synthetic and biological scaffolds.* Biomaterials, 2019. **192**: p. 405-415.
16. Mohseni, E., E. Zalnezhad, and A.R. Bushroa, *Comparative investigation on the adhesion of hydroxyapatite coating on Ti–6Al–*

*4V implant: A review paper.* International Journal of Adhesion and Adhesives, 2014. **48**: p. 238-257.
17. Hahn, B.D., et al., *Enhanced bioactivity and biocompatibility of nanostructured hydroxyapatite coating by hydrothermal annealing.* Thin Solid Films, 2011. **519**(22): p. 8085-8090.
18. Wang, H., et al., *Biocompatibility and osteogenesis of biomimetic nano-hydroxyapatite/polyamide composite scaffolds for bone tissue engineering.* Biomaterials, 2007. **28**(22): p. 3338-3348.
19. Faig-Martí, J. and F.J. Gil-Mur, *Hydroxyapatite coatings in prosthetic joints.* Revista Española de Cirugía Ortopédica y Traumatología (English Edition), 2008. **52**(2): p. 113-120.
20. Fielding, G.A., et al., *Antibacterial and biological characteristics of silver containing and strontium doped plasma sprayed hydroxyapatite coatings.* Acta Biomaterialia, 2012. **8**(8): p. 3144-3152.
21. Barry, J.N., et al., *Evaluation and comparison of hydroxyapatite coatings deposited using both thermal and non-thermal techniques.* Surface & Coatings Technology, 2013. **226**: p. 82-91.
22. Gopi, D., J. Indira, and L. Kavitha, *A comparative study on the direct and pulsed current electrodeposition of hydroxyapatite coatings on surgical grade stainless steel.* Surface and Coatings Technology, 2012. **206**(11): p. 2859-2869.
23. Ossa, C.P.O., S.O. Rogero, and A.P. Tschiptschin, *Cytotoxicity study of plasma-sprayed hydroxyapatite coating on high nitrogen austenitic stainless steels.* Journal of Materials Science-Materials in Medicine, 2006. **17**(11): p. 1095-1100.
24. Wang, H.N., et al., *Biocompatibility and osteogenesis of biomimetic nano-hydroxyapatite/polyamide composite scaffolds for bone tissue engineering.* Biomaterials, 2007. **28**(22): p. 3338-3348.
25. Olding, T., M. Sayer, and D. Barrow, *Ceramic sol-gel composite coatings for electrical insulation.* Thin Solid Films, 2001. **398**: p. 581-586.
26. Tredwin, C.J., et al., *Hydroxyapatite, fluor-hydroxyapatite and fluorapatite produced via the sol–gel method. Optimisation, characterisation and rheology.* Dental Materials, 2013. **29**(2): p. 166-173.
27. Baharuddin, M.Y., et al., *Fabrication of Low-Cost, Cementless Femoral Stem 316L Stainless Steel Using Investment Casting Technique.* Artificial Organs, 2014. **38**(7): p. 603-608.
28. Britannica, E.; Available from: https://www.britannica.com/science/calcium/Compounds.
29. I. M. Mehdawi, A.Y., *Antibacterial composite restorative materials for dental applications*, in *Non-Metallic Biomaterials for Tooth Repair and Replacement*. 2013, Woodhead Publishing Limited. p. 270-293.

30. Acevedo, J., et al., *Chemical synthesis of bone-like carbonate hydroxyapatite from hen eggshells and its characterization.* Boletín de la Sociedad Española de Cerámica y Vidrio, ISSN 0366-3175, Vol. 46, Nº. 5, 2007, pags. 225-231, 2007. **46**.
31. Tung, M.S., *Calcium Phosphates: Structure, Composition, Solubility, and Stability*, in *Calcium Phosphates in Biological and Industrial Systems*, Z. Amjad, Editor. 1998, Kluwer Academic Publishers. p. 1-20.
32. Canillas, M., et al., *Calcium phosphates for biomedical applications.* Boletín de la Sociedad Española de Cerámica y Vidrio, 2017. **56**(3): p. 91-112.
33. Kalita, S.J., A. Bhardwaj, and H.A. Bhatt, *Nanocrystalline calcium phosphate ceramics in biomedical engineering.* Materials Science and Engineering: C, 2007. **27**(3): p. 441-449.
34. Eliaz, N. and N. Metoki, *Calcium Phosphate Bioceramics: A Review of Their History, Structure, Properties, Coating Technologies and Biomedical Applications.* Materials (Basel, Switzerland), 2017. **10**(4): p. 334.
35. Naik, K.S., *Chapter 25 - Advanced bioceramics*, in *Advances in Biological Science Research*, S.N. Meena and M.M. Naik, Editors. 2019, Academic Press. p. 411-417.
36. Rey, C., et al., *1.11 Bioactive Calcium Phosphate Compounds: Physical Chemistry☆*, in *Comprehensive Biomaterials II*, P. Ducheyne, Editor. 2017, Elsevier: Oxford. p. 244-290.
37. Khalyfa, A., et al., *Development of a new calcium phosphate powder-binder system for the 3D printing of patient specific implants.* Journal of Materials Science: Materials in Medicine, 2007. **18**(5): p. 909-916.
38. Manchón, A., et al., *Antibiotic Release from Calcium Phosphate Materials in Oral and Maxillofacial Surgery. Molecular, Cellular and Pharmaceutical Aspects.* Current pharmaceutical biotechnology, 2016. **18**.
39. Vidal, E., et al., *Single-step pulsed electrodeposition of calcium phosphate coatings on titanium for drug delivery.* Surface and Coatings Technology, 2019. **358**: p. 266-275.
40. Bisso, S., et al., *Dual delivery of nucleic acids and PEGylated-bisphosphonates via calcium phosphate nanoparticles.* European Journal of Pharmaceutics and Biopharmaceutics, 2019. **142**: p. 142-152.
41. Sugawara, A., K. Asaoka, and S.-J. Ding, *Calcium Phosphate-Based Cements: Clinical Needs and Recent Progress.* J. Mater. Chem. B, 2013. **1**: p. 1081-1089.
42. *Scaffold*. Available from: https://www.innovationtoronto.com/2015/09/silk-and-ceramics-offer-hope-for-long-term-repair-of-joint-injuries/.

43. *Coated dental implant*. Available from: https://nanoscience.ch/en/2018/04/24/ceramic-coating-of-bone-implants-a-cost-effective-process-is-being-developed-in-the-nanocoatnano-argovia-project/.
44. Vallet-Regí, M. and E. Ruiz-Hernández, *Bioceramics: From Bone Regeneration to Cancer Nanomedicine.* Advanced Materials, 2011. **23**(44): p. 5177-5218.
45. Li, X., et al., *The effect of calcium phosphate microstructure on bone-related cells in vitro.* Biomaterials, 2008. **29**(23): p. 3306-3316.
46. Hayashi, K., M.L. Munar, and K. Ishikawa, *Carbonate apatite granules with uniformly sized pores that arrange regularly and penetrate straight through granules in one direction for bone regeneration.* Ceramics International, 2019. **45**(12): p. 15429-15434.
47. Rouahi, M., et al., *Physico-chemical characteristics and protein adsorption potential of hydroxyapatite particles: Influence on in vitro biocompatibility of ceramics after sintering.* Colloids and Surfaces B: Biointerfaces, 2006. **47**(1): p. 10-19.
48. Zhu, X.D., et al., *Effect of phase composition and microstructure of calcium phosphate ceramic particles on protein adsorption.* Acta Biomaterialia, 2010. **6**(4): p. 1536-1541.
49. Barba, D., E. Alabort, and R.C. Reed, *Synthetic bone: Design by additive manufacturing.* Acta Biomaterialia, 2019.
50. Ambard, A.J. and L. Mueninghoff, *Calcium Phosphate Cement: Review of Mechanical and Biological Properties.* Journal of Prosthodontics, 2006. **15**(5): p. 321-328.
51. Aronov, D., et al., *Tunable hydroxyapatite wettability: Effect on adhesion of biological molecules.* Process Biochemistry, 2006. **41**(12): p. 2367-2372.
52. Jeong, J., et al., *Bioactive calcium phosphate materials and applications in bone regeneration.* Biomaterials Research, 2019. **23**(1): p. 4.
53. Shadanbaz, S. and G.J. Dias, *Calcium phosphate coatings on magnesium alloys for biomedical applications: A review.* Acta Biomaterialia, 2012. **8**(1): p. 20-30.
54. Dorozhkin, S.V., *A detailed history of calcium orthophosphates from 1770s till 1950.* Materials Science and Engineering: C, 2013. **33**(6): p. 3085-3110.
55. Yacoubi, A.E., et al., *Rietveld Refinement of the Crystal Structure of Hydroxyapatite Using X-ray Powder Diffraction.* American Journal of Materials Science and Engineering, 2017. **5**(1): p. 1-5.
56. Fihri, A., et al., *Hydroxyapatite: A review of syntheses, structure and applications in heterogeneous catalysis.* Coordination Chemistry Reviews, 2017. **347**: p. 48-76.

57. Ma, G. and X.Y. Liu, *Hydroxyapatite: Hexagonal or Monoclinic?* Crystal Growth & Design, 2009. **9**(7): p. 2991-2994.
58. Kattimani, V.S., S. Kondaka, and K.P. Lingamaneni, *Hydroxyapatite–-Past, Present, and Future in Bone Regeneration.* Bone and Tissue Regeneration Insights, 2016. **7**: p. BTRI.S36138.
59. Wang, G., Z. Lu, and H. Zreiqat, *Bioceramics for skeletal bone regeneration*. 2014.
60. Blokhuis, T.J., *4 - Bioresorbable bone graft substitutes*, in *Bone Substitute Biomaterials*, K. Mallick, Editor. 2014, Woodhead Publishing. p. 80-92.
61. Narayanan, R., et al., *Calcium phosphate-based coatings on titanium and its alloys.* Journal of Biomedical Materials Research Part B: Applied Biomaterials, 2008. **85B**(1): p. 279-299.
62. Pasquale, S.M., et al., *Bone CO2-titration curves in acute hypercapnia obtained with a modified titration technique.* Journal of Applied Physiology, 1980. **48**(1): p. 197-201.
63. Szurkowska, K., A. Laskus, and J. Kolmas, *Hydroxyapatite-Based Materials for Potential Use in Bone Tissue Infections*. 2018.
64. Szcześ, A., L. Hołysz, and E. Chibowski, *Synthesis of hydroxyapatite for biomedical applications.* Advances in Colloid and Interface Science, 2017. **249**: p. 321-330.
65. Blokhuis, T., *Bioresorbable bone graft substitutes*. 2014. p. 80-93.
66. Dorozhkin, S.V., *Calcium orthophosphate bioceramics.* Ceramics International, 2015. **41**(10, Part B): p. 13913-13966.
67. Yasuda, H.Y., et al., *Preparation of hydroxyapatite/α-tricalcium phosphate composites by colloidal process.* Science and Technology of Advanced Materials, 2002. **3**(1): p. 29-33.
68. Dorozhkin, S.V., *Biphasic, triphasic and multiphasic calcium orthophosphates.* Acta Biomaterialia, 2012. **8**(3): p. 963-977.
69. Gelli, R., F. Ridi, and P. Baglioni, *The importance of being amorphous: calcium and magnesium phosphates in the human body*. Advances in Colloid and Interface Science, 2019. **269**: p. 219-235.
70. Gower, L.B., *Biomimetic Model Systems for Investigating the Amorphous Precursor Pathway and Its Role in Biomineralization.* Chemical Reviews, 2008. **108**(11): p. 4551-4627.
71. Suchanek, W. and M. Yoshimura, *Processing and properties of hydroxyapatite-based biomaterials for use as hard tissue replacement implants.* Journal of Materials Research, 2011. **13**(1): p. 94-117.
72. Zhou, H. and J. Lee, *Nanoscale hydroxyapatite particles for bone tissue engineering.* Acta Biomaterialia, 2011. **7**(7): p. 2769-2781.
73. Combes, C., S. Cazalbou, and C. Rey, *Apatite Biominerals.* Minerals, 2016. **6**: p. 34.

74. Yeroshalmi, F., *Dental Emergencies*, in *Clinical Manual of Emergency Pediatrics*, E.F. Crain and J.C. Gershel, Editors. 2018, Cambridge University Press: Cambridge. p. 83-97.
75. Nga, N.K., N.T. Thuy Chau, and P.H. Viet, *Facile synthesis of hydroxyapatite nanoparticles mimicking biological apatite from eggshells for bone-tissue engineering.* Colloids and Surfaces B: Biointerfaces, 2018. **172**: p. 769-778.
76. Wopenka, B. and J.D. Pasteris, *A mineralogical perspective on the apatite in bone.* Materials Science and Engineering: C, 2005. **25**(2): p. 131-143.
77. Loong, C.K., et al., *Evidence of hydroxyl-ion deficiency in bone apatites: an inelastic neutron-scattering study.* Bone, 2000. **26**(6): p. 599-602.
78. Dimitriou, R., et al., *Bone regeneration: current concepts and future directions.* BMC Medicine, 2011. **9**(1): p. 66.
79. Wang, W. and K.W.K. Yeung, *Bone grafts and biomaterials substitutes for bone defect repair: A review.* Bioactive Materials, 2017. **2**(4): p. 224-247.
80. Klifto, C., S. D. Gandi, and A. Sapienza, *Bone Graft Options in Upper-Extremity Surgery.* The Journal of Hand Surgery, 2018. **43**.
81. Khanijou, M., et al., *Bone graft material derived from extracted tooth: A review literature.* Journal of Oral and Maxillofacial Surgery, Medicine, and Pathology, 2019. **31**(1): p. 1-7.
82. Titsinides, S., G. Agrogiannis, and T. Karatzas, *Bone grafting materials in dentoalveolar reconstruction: A comprehensive review.* Japanese Dental Science Review, 2019. **55**(1): p. 26-32.
83. Yang, G., et al., *Bioactive calcium sulfate/magnesium phosphate cement for bone substitute applications.* Materials Science and Engineering: C, 2014. **35**: p. 70-76.
84. Khan, S.R., et al., *Agar and egg shell derived calcium carbonate and calcium hydroxide nanoparticles: Synthesis, characterization and applications.* Chemical Physics Letters, 2019. **732**: p. 136662.
85. He, F., et al., *Comparative study on in vivo response of porous calcium carbonate composite ceramic and biphasic calcium phosphate ceramic.* Materials Science and Engineering: C, 2016. **64**: p. 117-123.
86. Zhao, B., et al., *Promoting osteoblast proliferation on polymer bone substitutes with bone-like structure by combining hydroxyapatite and bioactive glass.* Materials Science and Engineering: C, 2019. **96**: p. 1-9.
87. Kłosowski, M.M., et al., *Probing carbonate in bone forming minerals on the nanometre scale.* Acta Biomaterialia, 2015. **20**: p. 129-139.

88. Diaz-Rodriguez, P., et al., *Mineralized alginate hydrogels using marine carbonates for bone tissue engineering applications.* Carbohydrate Polymers, 2018. **195**: p. 235-242.
89. Adil, A., M. Rouabhia, and Z. Zhang, *Potential use of bone tissue engineering to treat human bone defects*. 2013.
90. Sonekar, M.M. and W.S. Rathod, *An experimental investigation on tribologial behavior of bio-implant material (SS-316 l & Ti6Al4V) for orthopaedic applications.* Materials Today: Proceedings, 2019.
91. Andersen, P.J., *1.1 Metals for Use in Medicine*, in *Comprehensive Biomaterials II*, P. Ducheyne, Editor. 2017, Elsevier: Oxford. p. 1-18.
92. Oskouei, R.H., K. Fallahnezhad, and S. Kuppusami, *An Investigation on the Wear Resistance and Fatigue Behaviour of Ti-6Al-4V Notched Members Coated with Hydroxyapatite Coatings.* Materials (Basel, Switzerland), 2016. **9**(2): p. 111.
93. Wilson, J., *1 - Metallic biomaterials: State of the art and new challenges*, in *Fundamental Biomaterials: Metals*, P. Balakrishnan, S. M S, and S. Thomas, Editors. 2018, Woodhead Publishing. p. 1-33.
94. Balamurugan, A., et al., *Corrosion aspects of metallic implants — An overview.* Materials and Corrosion, 2008. **59**: p. 855-869.
95. Hussein, M., M. Samad, and N. Al-Aqeeli, *Wear Characteristics of Metallic Biomaterials: A Review.* Materials, 2015. **8**: p. 2749-2768.
96. Tan, M.H.C., et al., *Effect of niobium content on the microstructure and Young's modulus of Ti-xNb-7Zr alloys for medical implants.* Journal of the Mechanical Behavior of Biomedical Materials, 2019. **99**: p. 78-85.
97. Ramsden, J.J., et al., *The Design and Manufacture of Biomedical Surfaces.* CIRP Annals, 2007. **56**(2): p. 687-711.
98. Geetha, M., et al., *Ti based biomaterials, the ultimate choice for orthopaedic implants – A review.* Progress in Materials Science, 2009. **54**(3): p. 397-425.
99. *Stainless steel*. Available from: https://www.azom.com/article.aspx?ArticleID=2382.
100. Li, D.G., et al., *Molybdenum addition enhancing the corrosion behaviors of 316 L stainless steel in the simulated cathodic environment of proton exchange membrane fuel cell.* International Journal of Hydrogen Energy, 2015. **40**(17): p. 5947-5957.
101. Javanbakht, M., M.J. Hadianfard, and E. Salahinejad, *Microstructure and mechanical properties of a new group of nanocrystalline medical-grade stainless steels prepared by powder metallurgy.* Journal of Alloys and Compounds, 2015. **624**: p. 17-21.
102. Li, M., et al., *Study of biocompatibility of medical grade high nitrogen nickel-free austenitic stainless steel in vitro.* Materials Science and Engineering: C, 2014. **43**: p. 641-648.

103. Swiatkowska, I., N. Martin, and A.J. Hart, *Blood titanium level as a biomarker of orthopaedic implant wear.* Journal of Trace Elements in Medicine and Biology, 2019. **53**: p. 120-128.
104. Turnbull, G., et al., *3D bioactive composite scaffolds for bone tissue engineering.* Bioactive Materials, 2018. **3**(3): p. 278-314.
105. Das, A. and D. Pamu, *A comprehensive review on electrical properties of hydroxyapatite based ceramic composites.* Materials Science and Engineering: C, 2019. **101**: p. 539-563.
106. Abdullah, A.M., et al., *Enhancement of thermal, mechanical and physical properties of polyamide 12 composites via hybridization of ceramics for bone replacement.* Materials Science and Engineering: C, 2019. **99**: p. 719-725.
107. Du, X., et al., *3D printing of mesoporous bioactive glass/silk fibroin composite scaffolds for bone tissue engineering.* Materials Science and Engineering: C, 2019. **103**: p. 109731.
108. Farokhi, M., et al., *Silk fibroin/hydroxyapatite composites for bone tissue engineering.* Biotechnology Advances, 2018. **36**(1): p. 68-91.
109. Singh, T.R.R., et al., *6 - Microneedles for drug delivery and monitoring*, in *Microfluidic Devices for Biomedical Applications*, X. Li and Y. Zhou, Editors. 2013, Woodhead Publishing. p. 185-230.
110. Teixeira, V., et al., *11 - High barrier plastics using nanoscale inorganic films*, in *Multifunctional and Nanoreinforced Polymers for Food Packaging*, J.-M. Lagarón, Editor. 2011, Woodhead Publishing. p. 285-315.
111. Harun, W.S.W., et al., *A comprehensive review of hydroxyapatite-based coatings adhesion on metallic biomaterials.* Ceramics International, 2018. **44**(2): p. 1250-1268.
112. Otsuka, Y., H. Kawaguchi, and Y. Mutoh, *Cyclic delamination behavior of plasma-sprayed hydroxyapatite coating on Ti–6Al–4V substrates in simulated body fluid.* Materials Science and Engineering: C, 2016. **67**: p. 533-541.
113. Froes, F.H., *1.1 - Titanium for medical and dental applications—An introduction*, in *Titanium in Medical and Dental Applications*, F.H. Froes and M. Qian, Editors. 2018, Woodhead Publishing. p. 3-21.
114. *Chapter 1 - Deposition Technologies: An Overview*, in *Handbook of Deposition Technologies for Films and Coatings (Third Edition)*, P.M. Martin, Editor. 2010, William Andrew Publishing: Boston. p. 1-31.
115. Robertson, S.F., A. Bandyopadhyay, and S. Bose, *Titania nanotube interface to increase adhesion strength of hydroxyapatite sol-gel coatings on Ti-6Al-4V for orthopedic applications.* Surface and Coatings Technology, 2019. **372**: p. 140-147.

116. Garcia-Casas, A., et al., *Functionalization of sol-gel coatings with organophosphorus compounds for prosthetic devices.* Colloids and Surfaces B: Biointerfaces, 2019. **181**: p. 973-980.
117. Owens, G.J., et al., *Sol–gel based materials for biomedical applications.* Progress in Materials Science, 2016. **77**: p. 1-79.
118. Dorozhkin, S.V., *Calcium orthophosphate coatings on magnesium and its biodegradable alloys.* Acta Biomaterialia, 2014. **10**(7): p. 2919-2934.
119. Asri, R.I.M., et al., *A review of hydroxyapatite-based coating techniques: Sol–gel and electrochemical depositions on biocompatible metals.* Journal of the Mechanical Behavior of Biomedical Materials, 2016. **57**: p. 95-108.
120. Zhang, J.X.J. and K. Hoshino, *Chapter 2 - Fundamentals of nano/microfabrication and scale effect*, in *Molecular Sensors and Nanodevices (Second Edition)*, J.X.J. Zhang and K. Hoshino, Editors. 2019, Academic Press. p. 43-111.
121. Yilbas, B.S., A. Al-Sharafi, and H. Ali, *Chapter 3 - Surfaces for Self-Cleaning*, in *Self-Cleaning of Surfaces and Water Droplet Mobility*, B.S. Yilbas, A. Al-Sharafi, and H. Ali, Editors. 2019, Elsevier. p. 45-98.
122. *Spin-coating* Available from: https://www.keyence.com/ss/products/measure/sealing/coater-type/spin.jsp.
123. *Spin-coating*. Available from: https://www.ossila.com/pages/spin-coating#spin-coating-general-theory.
124. Madon, R., et al., *Effect of Reaction Temperature on Steam Methane Reforming's yield over Coated Nickel Aluminide (Ni 3 Al) Catalyst in Micro Reactor.* Journal of Advanced Research in Fluid Mechanics and Thermal Sciences, 2018. **50**.
125. *Dip-coating*. Available from: http://www.apexicindia.com/technologies/dip-coating-technology.
126. Habibovic, P., et al., *Biomimetic Apatite Coating on Metal Implants.* Journal of The American Ceramic Society - J AMER CERAM SOC, 2002. **85**: p. 517-522.
127. Makhlouf, A.S.H., *1 - Current and advanced coating technologies for industrial applications*, in *Nanocoatings and Ultra-Thin Films*, A.S.H. Makhlouf and I. Tiginyanu, Editors. 2011, Woodhead Publishing. p. 3-23.
128. Carlsson, J.-O. and P.M. Martin, *Chapter 7 - Chemical Vapor Deposition*, in *Handbook of Deposition Technologies for Films and Coatings (Third Edition)*, P.M. Martin, Editor. 2010, William Andrew Publishing: Boston. p. 314-363.
129. Park, J.-H. and T.S. Sudarshan, *Chemical vapor deposition.* 2001.

130. Putkonen, M., et al., *Atomic layer deposition and characterization of biocompatible hydroxyapatite thin films.* Thin Solid Films, 2009. **517**(20): p. 5819-5824.
131. Jilani, A., M. Abdel-wahab, and A. Hammad, *Advance Deposition Techniques for Thin Film and Coating*. 2017.
132. Wei, Q., Y. Xu, and Y. Wang, *3 - Textile surface functionalization by physical vapor deposition (PVD)*, in *Surface Modification of Textiles*, Q. Wei, Editor. 2009, Woodhead Publishing. p. 58-90.
133. *Mechanical engineering*. Available from: https://me-mechanicalengineering.com/physical-vapor-deposition/.
134. *Thermal evaporation*. Available from: https://www.albmaterials.com/what-is-thermal-evaporation.html.
135. Sigmund, P., *Recollections of fifty years with sputtering.* Thin Solid Films, 2012. **520**(19): p. 6031-6049.
136. *Chapter 6 - Ion Plating*, in *Handbook of Deposition Technologies for Films and Coatings (Third Edition)*, P.M. Martin, Editor. 2010, William Andrew Publishing: Boston. p. 297-313.
137. Li, P.H. and P.K. Chu, *1 - Thin film deposition technologies and processing of biomaterials*, in *Thin Film Coatings for Biomaterials and Biomedical Applications*, H.J. Griesser, Editor. 2016, Woodhead Publishing. p. 3-28.
138. Henao, J., et al., *Bio-active glass coatings manufactured by thermal spray: a status report.* Journal of Materials Research and Technology, 2019.
139. Liu, X., et al., *Effect of post-heat treatment on the microstructure of micro-plasma sprayed hydroxyapatite coatings.* Surface and Coatings Technology, 2019. **367**: p. 225-230.
140. Bogdanoviciene, I., et al., *Infuence of heating conditions on the formation of sol- gel derived calcium hydroxyapatite.* Chemija, 2010. **21**: p. 98-105.
141. Epiphanova, A., O. Magaev, and O. Vodyankina, *Formation and characterization of phosphate-modified silicate materials derived from sol–gel process.* Journal of Sol-Gel Science and Technology, 2012. **61**(3): p. 509-517.
142. Garskaite, E., et al., *Effect of processing conditions on the crystallinity and structure of carbonated calcium hydroxyapatite (CHAp).* CrystEngComm, 2014. **16**: p. 3950-3959.
143. Bogdanoviciene, I., et al., *Influence of heating conditions on the formation of sol-gel derived calcium hydroxyapatite.* Chemija, 2010. **21**(2-4): p. 98-105.
144. Gheisari, H., E. Karamian, and M. Abdellahi, *A novel hydroxyapatite –Hardystonite nanocomposite ceramic.* Ceramics International, 2015. **41**: p. 5967-5975.

145. Mujahid, M., S. Sarfraz, and S. Amin, *On the Formation of Hydroxyapatite Nano Crystals Prepared Using Cationic Surfactant.* Materials Research, 2015. **18**: p. 468-472.
146. Pauline, S.A. and N. Rajendran, *Biomimetic novel nanoporous niobium oxide coating for orthopaedic applications.* Applied Surface Science, 2014. **290**: p. 448-457.
147. Gan, L. and R. Pilliar, *Calcium phosphate sol–gel-derived thin films on porous-surfaced implants for enhanced osteoconductivity. Part I: Synthesis and characterization.* Biomaterials, 2004. **25**(22): p. 5303-5312.
148. Choi, A. and B. Ben-Nissan, *Sol-Gel Production of Bioactive Nanocoatings for Medical Applications. Part II: Current Research and Development.* Nanomedicine (London, England), 2007. **2**: p. 51-61.
149. Goudouri, O.M., et al., *Modifying a dental ceramic by bioactive glass via the sol–gel route: Characterization and bioactivity investigation.* Materials Chemistry and Physics, 2011. **125**(1): p. 309-313.
150. García, C., S. Ceré, and A. Durán, *Bioactive coatings prepared by sol–gel on stainless steel 316L.* Journal of Non-Crystalline Solids, 2004. **348**: p. 218-224.
151. Tas, A., *Molten Salt Synthesis of Calcium Hydroxyapatite Whiskers.* Journal of the American Ceramic Society, v.84, 295-300 (2001), 2001. **84**.
152. Yasuda, H., et al., *Preparation of Hydroxyapatite/Tricalcium Phosphate Composites by Colloidal Process.* Science and Technology of Advanced Materials - SCI TECHNOL ADV MATER, 2002. **3**: p. 29-33.
153. Josse, S., et al., *Chemically Modified Calcium Phosphates as Novel Materials for Bisphosphonate Delivery*. Vol. 16. 2004. 1423-1427.
154. Zhang, W., et al., *Rod-shaped hydroxyapatite with mesoporous structure as drug carriers for proteins.* Applied Surface Science, 2014. **322**: p. 71-77.
155. Son, J., T.-Y. Kwon, and K.-H. Kim, *Osteogenic Evaluation of Porous Calcium Phosphate Granules with Drug Delivery System Using Nanoparticle Carriers.* Journal of Nanoscience and Nanotechnology, 2015. **15**.
156. Gopi, D., et al., *Development of strontium and magnesium substituted porous hydroxyapatite/poly(3,4-ethylenedioxythiophene) coating on surgical grade stainless steel and its bioactivity on osteoblast cells.* Colloids and surfaces. B, Biointerfaces, 2013. **114C**: p. 234-240.
157. Hosseini, S., et al., *Improved surface bioactivity of stainless steel substrates using osteocalcin mimetic peptide.* Materials Chemistry and Physics, 2014. **143**(3): p. 1364-1371.

158. Surmeneva, M.A., et al., *Comparative study of the radio-frequency magnetron sputter deposited CaP films fabricated onto acid-etched or pulsed electron beam-treated titanium.* Thin Solid Films, 2014. **571**: p. 218-224.
159. Nawawi, N., I. Sopyan, and Z. Ahmad, *Fourier Transform Infrared Study on Sol-Gel Derived Manganese-Doped Hydroxyapatite*. Advanced Materials Research, 2008. **47-50**: p. 1185-1188.
160. Garskaite, E., et al., *Effect of processing conditions on the crystallinity and structure of carbonated calcium hydroxyapatite (CHAp).* Crystengcomm, 2014. **16**(19): p. 3950-3959.
161. Malakauskaite-Petruleviciene, M., et al., *Characterization of sol-gel processing of calcium phosphate thin films on silicon substrate by FTIR spectroscopy.* Vibrational Spectroscopy, 2016. **85**: p. 16-21.
162. Usinskas, P., et al., *Sol–gel processing of calcium hydroxyapatite thin films on silicon nitride (Si3N4) substrate.* Journal of Sol-Gel Science and Technology, 2017. **83**: p. 1-7.
163. Karampas, I.A. and C.G. Kontoyannis, *Characterization of calcium phosphates mixtures.* Vibrational Spectroscopy, 2013. **64**: p. 126-133.
164. Sofronia, A.M., et al., *Thermal and structural characterization of synthetic and natural nanocrystalline hydroxyapatite.* Materials Science and Engineering: C, 2014. **43**: p. 153-163.
165. Chernozem, R.V., et al., *Hybrid biocomposites based on titania nanotubes and a hydroxyapatite coating deposited by RF-magnetron sputtering: Surface topography, structure, and mechanical properties.* Applied Surface Science, 2017. **426**: p. 229-237.
166. Ramesh, B., et al., *Structural studies of a green-emitting terbium doped calcium zinc phosphate phosphor.* Journal of Molecular Structure, 2018. **1155**: p. 568-572.
167. Huang, J., et al., *Characterization and one-step synthesis of Hydroxyapatite-Ti(C,N)-TiO2 composite coating by cathodic plasma electrolytic saturation and accompanying electrochemical deposition on titanium alloy.* Surface and Coatings Technology, 2017. **324**: p. 463-470.
168. Razi, s., m. mollabashi, and k. madanipour, *Nanosecond Laser Surface Patterning of Bio Grade 316L Stainless Steel for Controlling its Wettability Characteristics.* ijop, 2015. **9**(1): p. 43-52.
169. Cai, Y., et al., *Superhydrophobic structures on 316L stainless steel surfaces machined by nanosecond pulsed laser*. Precision Engineering, 2018. **52**: p. 266-275.
170. Kokubo, T. and H. Takadama, *How useful is SBF in predicting in vivo bone bioactivity?* Biomaterials, 2006. **27**(15): p. 2907-2915.
171. Brázda, L., D. Rohanova, and A. Helebrant, *Kinetics of dissolution of calcium phosphate (Ca-P) bioceramics.* Processing and Application of Ceramics, 2008. **2**.

172. Wu, M., et al., *Preparation of bio-inspired polydopamine coating on hydrated tricalcium silicate substrate to accelerate hydroxyapatite mineralization.* Materials Letters, 2019. **236**: p. 120-123.
173. Xie, L., et al., *Fe/Zn-modified tricalcium phosphate (TCP) biomaterials: Preparation and biological properties.* RSC Advances, 2019. **9**: p. 781-789.
174. Chen, Z., et al., *Bioactivity of hydroxyapatite/wollastonite composite films deposited by pulsed laser.* Ceramics International, 2018. **44**(9): p. 10204-10209.
175. Shahrezaei, M., et al., *Synthesis of Magnesium Doped Amorphous Calcium Phosphate as a Bioceramic for Biomedical Application: In Vitro Study.* Silicon, 2017.
176. Heimann, R.B., *Plasma-Sprayed Hydroxylapatite Coatings as Biocompatible Intermediaries Between Inorganic Implant Surfaces and Living Tissue.* Journal of Thermal Spray Technology, 2018. **27**(8): p. 1212-1237.
177. Roy, M., A. Bandyopadhyay, and S. Bose, *Induction plasma sprayed nano hydroxyapatite coatings on titanium for orthopaedic and dental implants.* Surface and Coatings Technology, 2011. **205**(8): p. 2785-2792.
178. Xiao, G.-y., et al., *Fabrication of hydroxyapatite microspheres with poor crystallinity using a novel flame-drying method.* Transactions of Nonferrous Metals Society of China, 2012. **22**: p. s169-s174.
179. Zhu, H., et al., *Nanostructural insights into the dissolution behavior of Sr-doped hydroxyapatite.* Journal of the European Ceramic Society, 2018. **38**(16): p. 5554-5562.
180. Bellot-Gurlet, L., et al., *Raman Studies of Corrosion Layers Formed on Archaeological Irons in Various Media.* Journal of Nano Research, 2009. **8**: p. 147-156.
181. Colomban, P., S. Cherifi, and G. Despert, *Raman identification of corrosion products on automotive galvanized steel sheets.* Journal of Raman Spectroscopy, 2008. **39**: p. 881-886.
182. de Faria, D.L.A., S. Venâncio Silva, and M.T. de Oliveira, *Raman microspectroscopy of some iron oxides and oxyhydroxides.* Journal of Raman Spectroscopy, 1997. **28**(11): p. 873-878.
183. Froment, F., A. Tournié, and P. Colomban, *Raman Identification of Natural red to Yellow Pigments: Ochre and Iron-Containing Ores.* Journal of Raman Spectroscopy, 2008. **39**: p. 560-568.
184. Kernazhitsky, L., et al., *Laser-excited excitonic luminescence of nanocrystalline TiO2 powder.* Ukrainian Journal of Physics, 2014. **59**: p. 246-253.
185. Khan, A.F., et al., *Raman Spectroscopy of Natural Bone and Synthetic Apatites.* Applied Spectroscopy Reviews, 2013. **48**(4): p. 329-355.

186. Malakauskaite-Petruleviciene, M., et al., *Synthesis and characterization of sol–gel derived calcium hydroxyapatite thin films spin-coated on silicon substrate.* Ceramics International, 2015. **41**.
187. Niaura, G., A.K. Gaigalas, and V.L. Vilker, *Surface-Enhanced Raman Spectroscopy of Phosphate Anions: Adsorption on Silver, Gold, and Copper Electrodes.* The Journal of Physical Chemistry B, 1997. **101**(45): p. 9250-9262.
188. Sofronia, A., et al., *Thermal and structural characterization of synthetic and natural nanocrystalline hydroxyapatite.* Materials Science and Engineering: C, 2014. **43**: p. 153–163.
189. Zhang, Y., et al., *Asymmetric Lattice Vibrational Characteristics of Rutile TiO2 as Revealed by Laser Power Dependent Raman Spectroscopy.* The Journal of Physical Chemistry C, 2013. **117**: p. 24015–24022.

NOTES

NOTES

Vilniaus universiteto leidykla
Saulėtekio al. 9, LT-10222 Vilnius
El. p. info@leidykla.vu.lt,
www.leidykla.vu.lt
Tiražas 10 egz.